UNIVERSIDADE ESTADUAL DE CAMPINAS
INSTITUTO DE QUÍMICA

RAFAEL LAVAGNOLLI GERMSCHEIDT

WATER OXIDATION PERFORMANCE ENHANCED BY ELECTROCHEMICALLY DESIGNED VACANCIES ON PRUSSIAN BLUE ANALOGUES BASED CATALYSTS

MELHORA DA PERFORMANCE DA REAÇÃO DE OXIDAÇÃO DA ÁGUA PELO DESIGN DE VACANCIAS FORMADAS ELETROQUIMICAMENTE EM CATALISADORES A BASE DE ANÁLOGOS DO AZUL DA PRÚSSIA

CAMPINAS
2023

RAFAEL LAVAGNOLLI GERMSCHEIDT

WATER OXIDATION PERFORMANCE ENHANCED BY ELECTROCHEMICALLY DESIGNED VACANCIES ON PRUSSIAN BLUE ANALOGUES BASED CATALYSTS

MELHORA DA PERFORMANCE DA REAÇÃO DE OXIDAÇÃO DA ÁGUA PELO DESIGN DE VACANCIAS FORMADAS ELETROQUIMICAMENTE EM CATALISADORES A BASE DE ANÁLOGOS DO AZUL DA PRÚSSIA

Tese de Doutorado apresentada ao Instituto de Química da Universidade Estadual de Campinas como parte dos requisitos exigidos para a obtenção do título de Doutor em Ciências.

Doctor's Thesis presented to the Institute of Chemistry of the University of Campinas as part of the requirements to obtain the title of Doctor in Sciences.

Supervisor: Dr. Juliano Alves Bonacin
Co-supervisor: Dr. Tulio Costa Rizuti da Rocha

O arquivo digital corresponde à versão final da Tese defendida pelo aluno Rafael Lavagnolli Germscheidt e orientada pelo Prof. Dr. Juliano Alves Bonacin.

CAMPINAS
2023

Ficha catalográfica
Universidade Estadual de Campinas
Biblioteca do Instituto de Química
Simone Luiz Alves - CRB 8/9094

G318w Germscheidt, Rafael Lavagnolli, 1997-
Water oxidation performance enhanced by electrochemically designed vacancies on Prussian blue analogues-based catalysts / Rafael Lavagnolli Germscheidt. – Campinas, SP : [s.n.], 2023.

Orientador: Juliano Alves Bonacin.
Coorientador: Tulio Costa Rizuti da Rocha.
Tese (doutorado) – Universidade Estadual de Campinas, Instituto de Química.

1. Eletroquímica. 2. Catálise. 3. Azul da Prússia. 4. Defeitos estruturais. 5. Espectroscopia de raio X. I. Bonacin, Juliano Alves, 1980-. II. Rocha, Tulio Costa Rizuti da, 1979-. III. Universidade Estadual de Campinas. Instituto de Química. IV. Título.

Informações Complementares

Título em outro idioma: Melhora da performance da reação de oxidação da água pelo design de vacancias formadas eletroquimicamente em catalisadores a base de análogos do azul da Prússia
Palavras-chave em inglês:
Electrochemistry
Catalysis
Prussian blue
Structural defects
X-ray spectroscopy
Área de concentração: Química Inorgânica
Titulação: Doutor em Ciências
Banca examinadora:
Juliano Alves Bonacin [Orientador]
Kalil Cristhian Figueiredo Toledo
Raphael Nagao de Sousa
Paulo Cesar de Sousa Filho
Caterina Gruenwaldt Cunha Marques Netto
Data de defesa: 11-09-2023
Programa de Pós-Graduação: Química

Identificação e informações acadêmicas do(a) aluno(a)
- ORCID do autor: https://orcid.org/0000-0001-6328-8249
- Currículo Lattes do autor: http://lattes.cnpq.br/3262605160950586

BANCA EXAMINADORA

Prof. Dr. Juliano Alves Bonacin (Orientador)

Dr. Kalil Cristhian Figueiredo Toledo (Universidade de São Paulo)

Prof. Dr. Raphael Nagao de Sousa (IQ/UNICAMP)

Prof. Dr. Paulo Cesar de Sousa Filho (IQ/UNICAMP)

Dra. Caterina Gruenwaldt Cunha Marques Netto (Universidade Federal de São Carlos)

A Ata da defesa assinada pelos membros da Comissão Examinadora, consta no SIGA/Sistema de Fluxo de Dissertação/Tese e na Secretaria do Programa da Unidade.

Este exemplar corresponde à redação final da Tese de Doutorado defendida pelo aluno **Rafael Lavagnolli Germscheidt**, aprovada pela Comissão Julgadora em 11 de setembro de 2023.

“We’re all stories in the end.
Just make it a good one, eh?”

Doctor Who – S05E13 (2010)

Agradecimentos

Ao meu orientador, professor Juliano por todo apoio e ajuda desde o começo do meu doutorado. Muito obrigado por todas as conversas, discussões científicas, ensinamento, encorajamento e motivação em vários momentos. Você tem sido minha inspiração como pesquisador e orientador, e contribuiu muito com a minha formação pessoal e profissional. Muito obrigado, você foi essencial.

Ao meu marido Lucas, agradeço imensamente por todo apoio durante toda essa jornada. Nos conhecemos um pouco depois que eu já havia começado, e desde então, você tem me apoiado e estado comigo em cada momento. Passei por um momento pessoal bem difícil durante esse processo, não relacionado ao doutorado, e você esteve sempre ao meu lado, me incentivando e motivando a continuar, só tenho a agradecer. E agora, vamos juntos para uma nova aventura em Barcelona e não poderia estar mais feliz. Amo compartilhar a vida e estar junto com você.

As minhas grandes amigas que ganhei durante o doutorado e levarei para a vida, Theo e Gabi, muito obrigado por tudo, vocês se tornaram minha família. Theo, nos conhecemos nas primeiras semanas do doutorado, quando estávamos os dois ainda bem perdidos, e desde então, temos nos ajudado e apoiado em tudo. Obrigado por sempre comemorar comigo todas as conquistas, desde um experimento simples dando certo, a um artigo aceito, a aniversário e vitorias da vida. E obrigado por me apoiar nos momentos difíceis e tristes, você deixou os dias no laboratório mais leves e nossos roles sempre tão incríveis. E Gabi, serei sempre grato pelos cafés, pelas fofocas, pelos dias fazendo home office juntos porque eu não estava bem para ficar sozinho, por sempre me emprestar um quarto na sua casa quando eu precisava ficar em Campinas. Sem falar de todo apoio e por sempre comemorar comigo todos os momentos bons e estarmos juntos nos ruins também. Muito obrigado, eu amo vocês.

À minha amiga Laura, que mesmo estando longe, sempre esteve presente durante esse tempo, ansioso para nossos roles na Europa, já estou chegando.

À Ju, minha psicóloga, por toda ajuda e apoio nesse tempo. O período difícil que enfrentei não estava relacionado com o doutorado, mas você me ajudou muito a ficar bem, para que eu pudesse concluir o doutorado da melhor forma possível. Muito obrigado por contribuir com meu crescimento pessoal.

À Ana, que de IC se tornou uma amiga. Muito obrigado por toda a ajuda no laboratório com o projeto e os experimentos, além de todas as conversas, fofocas e apoio sempre. Saudades e desejo um enorme sucesso para você.

Ao Daniel, meu amigo do laboratório, muito obrigado pelas conversas, roles assistindo ICarly, pedidos de churros todos os dias depois do almoço e toda a ajuda e discussões no laboratório também. Te desejo muito sucesso!

À Cris por toda ajuda, conversas e companheirismo. Muito obrigado pela ajuda com todos os processos FAPESP, com partes analíticas do projeto e todas as dúvidas que sempre esteve disposta a tirar e a ajuda da melhor maneira. Sem contar todas as dicas sobre Barcelona, com certeza farão a diferença.

À Acacia, técnica do laboratório, por toda ajuda e amizade nesses anos. Lembro de te conhecer logo no começo, quando me ajudou a enviar os documentos para a bolsa. E depois, em todos esses anos, sempre esteve presente para ajudar em todo necessário e ouvir todas nossas histórias, você realmente faz a diferença no laboratório.

A todos que passaram pelo laboratório durante esses anos enquanto estive lá, Pãmyla, Priscilla, Rafael Yoshimura, Thiago, Gabriel, Mateus, Gabriel, Evandro, Nycolas, Luis, Fiorella, Mari, João, Marcos, Marcelo e Gabi. Muito obrigado por todas as discussões científicasE com certeza, obrigado pelos bolos e comemorações que sempre arrumávamos alguma desculpa para fazer.

Ao prof. Airton por todo apoio, companheirismo e conversas durante o doutorado. E obrigado por sempre me aceitar ser intruso no seu laboratório para ficar trabalhando com a Theo.

As alunas do prof. Zezzi, Dani e Eduarda, muito obrigado por toda a ajuda com as análises do laser e do ICP. Além de me ajudarem nas loucuras e correrias para fazer as amostras darem certo e obtermos os melhores resultados. Com certeza fizeram toda a diferença durante esse tempo e eu amei muito poder conhecer vocês.

Ao meu coorientador, Dr. Tulio Costa por toda ajuda e discussões durante o projeto. Muito obrigado por todo apoio com as análises no Sirius e toda a explicação sobre os experimentos e técnica a cada discussão.

Ao staff da linha IPE do Sirius, Luiz, Felipe e Thiago por toda ajuda e apoio durante o tempo de linha.

Aos professores Airton, Fernando Sigoli, Italo e Julio Pastes por todo apoio e ensino durante a realização do PED.

Aos professores André Formiga, William e Lauro Kubota por todas as considerações durante o exame de qualificação geral.

Ao professor Rafael Nagao e professora Ana Flávia por todas as contribuições durante o exame de qualificação de área.

Aos professores membros da banca de doutorado: Kalil Cristhian, Fabio Henrique Barros de Lima, Raphael Nagao e Paulo Cesar de Sousa Filho por aceitarem o convite e pela contribuição com a finalização deste trabalho.

Aos técnicos Milene, Cláudia, Sônia, Ricardo e Hugo por toda ajuda e paciência durante os treinamentos, além de sempre estarem dispostos a ajudar durante qualquer dúvida durante as análises e na busca da solução de problemas.

This thesis was financed by the São Paulo Research Foundation (FAPESP) under grant #2018/25092-9.

This study was financed in part by the Coordenação de Aperfeiçoamento de Pessoal de Nível Superior – Brasil (CAPES) – Finance Code 001.

Resumo

A busca por fontes limpas, renováveis e ecológicas de hidrogênio fizeram com que a água fosse uma excelente candidata para ser utilizada como matéria prima na produção de hidrogênio. A produção de hidrogênio verde a partir da água é feita através de um sistema conhecido como *Water Splitting* (WS) e é limitado pelo processo anódico, denominado reação de evolução de oxigênio, sendo necessário a utilização de um catalisador para que a reação seja eficiente. O Azul da Prússia é um material inorgânico de valência mista em uma estrutura cúbica tridimensional formado por Fe(II) ligado a Fe(III) através de pontes de cianeto. Além disso, o ferro pode ser substituído por outros metais de transição e uma estrutura análoga é obtida, conhecida como Análogos ao Azul da Prússia. Esses análogos são representados por $M_{1(x)}[M_2(CN)_6]_{(y)}$, onde M_2 é um hexacianometalato desempenhando uma função estrutural e pode modular efeitos de doador-receptor do outro metal. Enquanto isso, M_1 é um metal da primeira série de transição e está coordenado ao N, dando origem a essa estrutura cúbica 3D. Devido as suas ótimas propriedade eletroquímicas, eles representam uma ótima alternativa como catalisadores baseados em metais abundantes para reação de evolução de oxigênio, tendo uma ótima performance, atividade e estabilidade operando em condições brandas de pH. Entretanto, apesar de terem alta estabilidade e atividade, o principal desafio é a baixa concentração de sítios ativos, dessa maneira, uma engenharia da estrutura e defeitos é essencial para se obter uma alta concentração de sítios ativos nesse material.

Nessa tese, o mecanismo da oxidação eletroquímica da água utilizando catalisadores a base de análogos de azul da Prússia é investigado, além disso, são propostas algumas estratégias para melhorar sua atividade. Portanto, eu reporto o pré-tratamento fotoquímico para a quantificação de ferro total em filmes heterogêneos de materiais baseados em ferro. A abordagem fotoquímica foi usada para garantir uma dissociação completa dos íons de ferro antes da quantificação. Além disso, uma metodologia alternativa para a síntese do azul da Prússia foi proposta, consistindo na aplicação de um alto potencial ao eletrodo em uma solução contendo $[Fe(CN)_6]^{4-}$, que foi então oxidado junto com alguns grupos cianeto, obtendo um catalisador com vacâncias geradas eletroquimicamente e então, teve sua atividade durante a reação de evolução de oxigênio estudada, apresentando uma ótima performance. Ademais, essa metodologia foi utilizada para criar defeitos de cianeto em um análogo do azul da Prússia formado por CoFe, nos permitindo entender o papel desses defeitos na

melhora da atividade desses catalisadores durante a reação de oxidação da água. Por fim, uso de espectroscopia de raio-X mole realizada em uma fonte de luz sincrotron foi utilizada para identificar a composição e a natureza desses defeitos.

Abstract

The search for clean, renewable, and environmentally friendly hydrogen sources has made water an excellent feedstock candidate to produce hydrogen. The production of green H_2 from water occurs by a system known as Water Splitting (WS), which is limited by the anodic process, called Oxygen Evolution Reaction (OER), thus, it requires a catalyst to be effective. Prussian Blue (PB) is an inorganic material of mixed valence in a tridimensional framework formed by Fe(II) bound to Fe(III) through a cyanide bridge. Moreover, the iron can be substituted by some other transition metals and an analogue structure known as Prussian blue analogues (PBA) can be obtained. PBAs are represented by $M_{1(x)}[M_2(CN)_6]_{(y)}$, where M_2 is an hexacyanometalate that plays a structural role and it can modulate the donor-acceptor effect to the other metal and M_1 a first-row transition metal and it is coordinated to the N atoms forming a 3D network. Due to their outstanding electrochemical properties, it represents a great alternative as an Earth-abundant catalyst for OER, presenting great performance, activity, and stability under mild conditions. Nonetheless, despite their high stability and activity, the main shortcoming is their low concentration of active sites, thus, engineering the structure and defects is essential to lead to a high concentration of active sites.

In this thesis, the electrochemical mechanisms of water oxidation using catalysts based on Prussian Blue analogues is investigated, moreover, strategies to enhance their activity are proposed**.** Thus, I report a photochemical pre-treatment for the quantification of the total iron from heterogeneous thin films composed of iron-based materials. The photochemical approach is used to ensure a full dissociation of iron ions before the quantification. Furthermore, an alternative methodology to synthesize the Prussian blue was proposed, by applying a high and constant potential to the electrode in a solution containing $[Fe(CN)_6]^{4-}$ that is oxidized along with some cyanide groups, obtaining a catalyst with electrochemically formed vacancies and have its performance towards WOR studied, presenting an outstanding activity. Furthermore, the same methodology was applied to create these cyanide vacancies on a CoFe Prussian blue analogue catalyst, allowing the understanding of the role of these vacancies on the enhancement of these catalysts' performance towards OER. Finally, synchrotron-based soft X-ray spectroscopy was used to probe the composition and the nature of these defects.

Abbreviations and Symbols

[Co]surf.	superficial concentration of electroactive Co^{2+} sites
AAS	atomic absorption spectroscopy
ABS	acrylonitrile, butadiene, and styrene filament
ACoFePBA	activated Cobalt-Iron Prussian blue analogue
AEC	alkaline electrolysis cells
AFM	Atomic force microscopy
Ag/AgCl 3.5 M	silver/silver chloride 3.5 mol L^{-1} reference electrode
APB	activated Prussian blue
CE	counter electrode
CoFePBA	Cobalt-Iron Prussian blue analogue
CPE	constant phase element
CV	cyclic voltammetry
DMF	dimethylformamide
DO	dissolved oxygen
ECSA	electrochemical active surface area
EDS	energy-dispersive X-ray spectroscopy
EIS	electrochemical impedance spectroscopy
FCs	fuel cells
FTIR	Fourier transform infrared spectroscopy
FTO	fluorine doped tin oxide electrode
GCE	glassy carbon electrode

HER	hydrogen evolution reaction
HOMO	highest occupied molecular orbital
HPP	hydrogen production pathway
ICP-MS	inductively coupled plasma mass spectrometry
ICP-OES	inductively coupled plasma optical emission spectrometry
j	Current density
k^0_{obs}	heterogeneous electron transfer rate constant
KPFM	Kelvin probe force microscopy
LA-ICP-MS	laser ablation inductively coupled plasma mass spectrometry
LNLS	Brazilian Synchrotron Light Laboratory
LOD	detection limit
LOQ	quantification limit
LSV	linear sweep voltammetry
LUMO	lowest unoccupied molecular orbital
MLCT	metal-to-ligand charge transfer
MS	mass spectroscopy
NHE	normal hydrogen electrode
OER	oxygen evolution reaction
PB	Prussian blue
PBA	Prussian blue analogue
PEMEC	proton exchange membrane electrolysis cells
R_{ct}	charge transfer resistance
RE	reference electrode

R_u	uncompensated resistance
SCE	saturated calomel electrode
SECM	Scanning Electrochemical Microscopy
SEM	scanning electron microscopy
SG/TC	substrate generation / tip collection
SOEC	solid oxide electrolysis cells
SQ	single quadrupole
SQ-KED	kinetic energy discrimination
STL	standard tessellation language
TOF	turnover frequency
TON	turnover number
TPB	traditional Prussian blue
UME	ultramicro-electrode
UV	ultraviolet
UV-Vis	electronic absorption spectroscopy in the ultraviolet-visible region
WE	working electrode
WOR	water oxidation reaction
WS	water splitting
XAS	X-Ray absorption spectroscopy
XPS	X-ray photoelectron spectroscopy
XRD	X-ray diffractometry
η	overpotential
λ	wavelength

Contents

Overview 18

Chapter I. Introduction and Objectives 20

1.1. Hydrogen environmental benefits depend on the way of production 21

1.2. Green Hydrogen 26

1.3. Prussian Blue 31

1.4. Objectives 33

Chapter II. Photochemical Pre-Treatment to Quantify Iron in Thin Films 34

2.1 Introduction 35

2.2 Experimental Section 36

2.2.1 Catalyst preparation and GCE modification 36

2.2.1.1 Hematite (Fe_2O_3) 36

2.2.1.2 Bimetallic hydroxide (NiFe(oxy)OH) 36

2.2.1.3 Prussian Blue (PB) 37

2.2.1.4 CoFe Prussian Blue analogues (CoFePBA) 37

2.2.1.5 CoFe oxide ($CoFeO_x$) 37

2.2.2 Preparation for iron quantification 37

2.2.3 Electronic Spectroscopy 38

2.2.4 Calibration Curve Validation 38

2.2.5 Accuracy check for Fe quantification by Inductively Coupled Plasma Mass Spectrometry (ICP-MS) 39

2.2.5.1 Sample Preparation 39

2.2.5.2 ICP-MS Instrumental Parameters 39

2.2.5.3 ICP-MS Results 39

2.3 Results and Discussion 40

2.3.1 Fe concentration calibration 40

2.3.2 Iron quantification in different catalysts 46

2.4 Conclusion 53

2.5 Acknowledgments 53

Chapter III. Water oxidation performance enhanced by electrochemically designed vacancies on Prussian blue catalyst. 54

3.1 Introduction 55

3.2 Experimental Section 56
3.2.1 Catalyst preparation and GCE modification 56
3.2.1.1 Traditional Prussian Blue 56
3.2.1.2 Activated Prussian Blue 57
3.2.2 Electrochemical characterization 57
3.2.3 3D Printed SECM assembling and calibration 57
3.2.3.1 3D printed SECM design 57
3.2.3.2 Oxygen Evolution Studies 58
3.2.3.3 Oxygen Evolution Studies 59
3.2.3.4 TOF Calculation 60
3.2.4 Electrochemical Active Surface Area (ECSA) and Heterogeneous electron transfer rate constant (K^{o}_{obs}) 62
3.2.5 FTIR Spectroscopy 63
3.2.6 RAMAN Spectroscopy 63
3.2.7 UV-Vis Spectroscopy 64
3.2.8 SEM 64
3.2.9 AFM 64
3.2.10 XPS and XAS 64
3.2.11 Laser Ablation Inductively Coupled Plasma Mass Spectrometry (LA-ICP-MS) 65
3.2.11.1 Instrumentation and Measurements of LA-ICP-MS 65
3.3 Results and Discussion 67
3.3.1 Synthesis and Characterization **67**
3.3.1.1 X-ray Diffraction (XRD) 69
3.3.1.2 Vibrational Spectroscopy 70
3.3.2 Catalytic activity study 74
3.3.3 Spectroscopy studies 77
3.3.4 Morphological characterization 81
3.3.4.1 Scanning Electron Microscopy coupled with EDS (SEM-EDS) 81
3.3.4.2 Atomic Force microscopy 84
3.3.5 Synchrotron-based soft X-ray spectroscopy 87
3.3.6 Laser ablation inductively coupled plasma mass spectrometry (LA-ICP-MS) ... 89
3.3.7 Active Sites quantification 90
3.4 Conclusion 92
3.5 Acknowledgments 92

Chapter IV. Electrochemical designed cyanide vacancies influence on CoFePBA-based catalysts boosted performance during the Oxygen Evolution reaction under mild conditions. 94
4.1 Introduction 95
4.2 Experimental Section 96
4.2.1 Catalyst preparation and substrate modification 96
4.2.1.1 CoFe Prussian Blue analogue 96
4.2.1.2 Activated CoFe Prussian Blue 96
4.2.2 Electrochemical characterization 97
4.2.3 Further characterization 97
4.3 **Results and discussion** 97
4.3.1 Synthesis and Characterization 97
4.3.1.1 Film synthesis 97
4.3.1.2 Morphological Characterization 98
4.3.1.3 Spectroscopy studies 99
4.3.1.4 Electrochemical paraments 101
4.3.2 Catalytic studies 104
4.3.3 LA-ICP-MS 109
4.3.4 Synchrotron-based soft X-ray spectroscopy 111
4.4 Conclusion 115
4.5 Acknowledgments 115
Chapter V. Conclusion and Perspectives 117
5.1 Addressal of objectives 117
5.2 Research perspectives 119
Bibliography 121
Appendix A 132
Appendix B 133
Appendix C 134
Appendix D 135
Appendix E 136

Overview

This thesis consists of five chapters described as follows:

Chapter I is an adaptation of the two published articles, with provided copyright permissions[1,2] and introduces the general research background, presenting the main problem and questions aimed to be answered. An overview on the production of green hydrogen and the water splitting process is presented, followed by a description of Prussian Blue analogues as great alternatives as water oxidation reaction catalysts. At last, the main objectives of this thesis are presented.

Chapter II is an adaptation of the article entitled "Photochemical Pre-Treatment to Quantify Iron in Thin Films"[3], with provided copyright permissions, and it presents how important is a photochemical pre-treatment for the quantification of the total iron from heterogeneous thin films composed of iron-based materials. The photochemical approach is used to ensure a full dissociation of iron ions before the quantification. This method is revealed to be highly effective and precise, having a wide range of applications for different iron-based catalysts.

Chapter III is an adaptation of the article entitled "Water oxidation performance enhanced by electrochemically designed vacancies on Prussian blue catalyst"[4], with provided copyright permissions, and it presents an alternative methodology to synthesize the Prussian blue, obtaining a catalyst with vacancies created by an electrochemical method. This catalyst showed an outstanding activity, with an onset overpotential of 361 mV. Using pyridine as a molecular probe, we identified the presence of vacant Fe^{2+} sites, and the quantification of these sites allowed us to estimate a TOF number of 0.2170 s^{-1} for the water oxidation reaction. These results indicate that defect engineering is a versatile strategy to boost the catalytic activity in Prussian blue analogues by increasing the number of active sites.

Chapter IV is an adaptation of the manuscript under preparation for publication entitled "Electrochemical designed cyanide vacancies influence on CoFePBA-based catalysts boosted performance during the Oxygen Evolution reaction under mild conditions" and it presents the creation of electrochemically formed cyanide vacancies in a CoFe Prussian blue analogue. The results shows that the material activation can improve the oxygen evolution in 35% in an overpotential of 400mV. Furthermore, the presence of vacancies is reported to improve the number of vacant Co^{2+} sites and spectroscopic studies show evidence of changes in the ligand-field

structure. Finally, synchrotron based soft X-ray spectroscopy provides evidence that the creation of vacancies can modulate the metallic sites oxidation states. These results open a great opportunity to study other PBA with those electrochemically formed vacancies, expecting outstanding activities towards the water oxidation reaction.

Chapter IV sums-up all the main conclusions for each chapter and presents the perspectives for future research.

Chapter I

Introduction and Objectives

The content of Chapter I is an adaptation of the two published articles.

The first one entitled "Hydrogen Environmental Benefits Depend on the Way of Production: An Overview of the Main Processes Production and Challenges by 2050" by Rafael L. Germscheidt, Daniel E. B. Moreira, Rafael G. Yoshimura, Nathália P. Gasbarro, Evandro Datti, Pãmyla L. dos Santos and Juliano A. Bonacin reprinted with permission from Advanced Energy and Sustainability Research, Copyright © 2021 Wiley-VCH GmbH, **Appendix B**. Reference: Adv. Energy and Sustainability Res. 2021, 2 (10), 2100093. DOI: 10.1002/aesr.202100093.

The second entitled "Is Hydrogen Indispensable for a Sustainable World? A Review of H2 Applications and Perspectives for the Next Years" by Theodora W. Von Zuben, Daniel E. B. Moreira, Rafael L. Germscheidt, Rafael G. Yoshimura, a Daniel S. Dorretto, Ana B. S. de Araujo, Airton G. Salles Jr., and Juliano A. Bonacin. reprinted with permission from Journal of the Brazilian Chemical Society, Copyright ©2023 Sociedade Brasileira de Química, **Appendix C** and **D**. Reference: J. Braz. Chem. Soc. 33 (8) • 2022. DOI: 10.21577/0103-5053.20220026.

Graphical Abstract

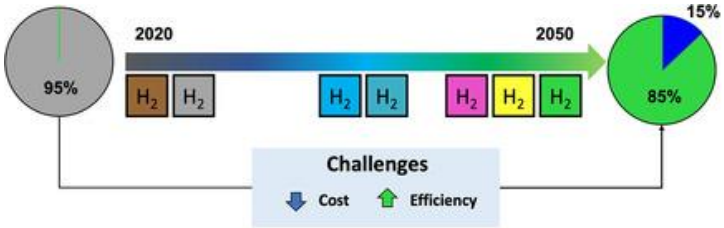

Adv. Energy and Sustainability Res. 2021, 2 (10), 2100093

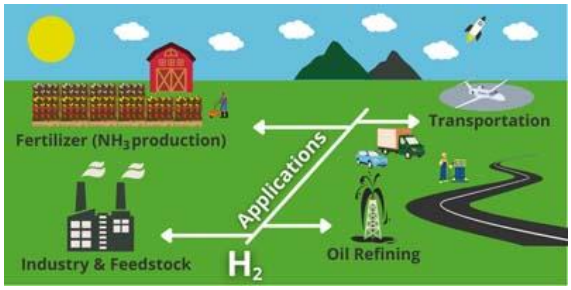

J. Braz. Chem. Soc. 33 (8) • 2022

1.1. Hydrogen environmental benefits depend on the way of production

Hydrogen is the smallest and the lightest element in the periodic table (atomic ratio 53 pm and atomic mass 1.008), and surprisingly it is the most abundant element in the whole universe. It is the 10th most abundant element on Earth (0.14%)[5] and it can be found in our atmosphere (0.6 ppm)[6], in water, in organic molecules or other chemical compounds. In the same way, hydrogen can be found in large quantities in the sun.[7,8] Hydrogen represents 73.4% of the sun's mass, being responsible for 85% of its energy, that comes from hydrogen atoms fusion, forming helium and releasing a huge amount of energy, approximately 10^{34} J/Year.[9]

The first report of molecular hydrogen is dated at the beginning of the 16th century when a gas was identified as a product of the reaction between sulfuric acid and iron. This gas was first identified as a unique substance by Henry Cavendish in 1776, however, it was only named in 1788 by Antoine Lavoisier, that named the substance from the Greek roots "hydro" (water) and "genes" (creator). Since then, H_2 has been extensively studied and used for a wide range of applications, as presented in **Figure 1**.[2,10]

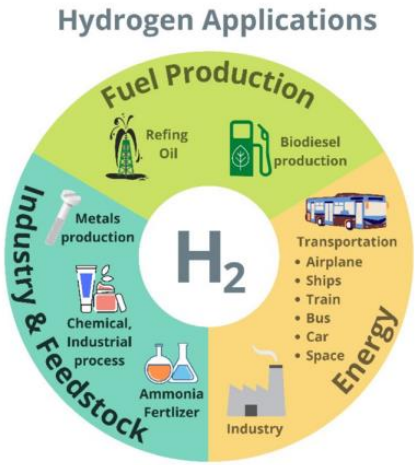

Figure 1. An overview of the applications of hydrogen.

Hydrogen is very important in the petrochemical industry, where it has a wide range of industrial applications, including hydrocracking (hydrogenation to produce refined fuels with smaller molecules and higher H/C ratios) and hydroprocessing (hydrogenation of sulfur and nitrogen compounds to further remove them as H_2S and NH_3) for the purification of petroleum and fuels. Besides that, hydrogen is essential in the base industry especially through the synthesis of

ammonia from the direct reaction with N_2 at high temperatures and pressure in the well-known Haber-Bosch Process.[11] It is worth mentioning that that 85% of the overall global ammonia production is converted into synthetic fertilizer, responsible for supporting the global food production, thus, if the ammonia production faces problems with feedstock costs (H_2), this could bring changes and challenges for the whole economy and food market. Hydrogenation can also be applied to decrease the degree of unsaturation in fats and oils and on some fine chemical synthesis. Hydrogen can also be used in the electronics industry as a protective and carrier gas, in deposition processes, for cleaning, in etching and in reduction processes. Another example is its use in the metallurgic industry in the reduction stages and also in the direct reduction of iron ore, which involves the separation of oxygen from the iron ore using hydrogen and synthesis gas (syngas). A strategic application of the H_2 is to consider it as a fuel,[4] being able to be applicable for direct combustion, by itself or in some blends with natural gas; and also in Fuel Cells (FCs), where it can provide a reliable and efficient energy power, that can be used in stationary power stations and also as a good candidate for transportation vehicles. [7,10,12–15]. Although it has a lot of applications, according to a sense from 2018,[11] 51.70% of total H_2 worldwide is used for refining, 42.62% is used for ammonia production and only 5.68% is used for other applications, including its use as a clean and renewable fuel. Furthermore, the demand for hydrogen has been reported to have increased in the past few years and is expected to continue increasing in the next few years or decades as the world searches for more sustainable solutions.[1,2]

Hydrogen has been drawing a lot of international interest, and the amount of countries that directly support investment in hydrogen technologies is increasing. Since the Sustainable Development Goals were adopted in 2015, governments have invested to reach the goals.[5,25,26] In 2019, the number of targets, mandates and policy incentives was around 50 actions, several policies that directly support the hydrogen application had been made, by countries of G20 and the European Union.[5]

As presented in **Figure 2**, in the last decades, the demand for hydrogen has been growing and will keep the pace until 2050.[2] Particularly in the Latin America, it is expected an increase of 67% in the hydrogen demand until 2030, to apply in the sector of iron, steel, ammonia, cement and methanol production, refining and transport.[27]

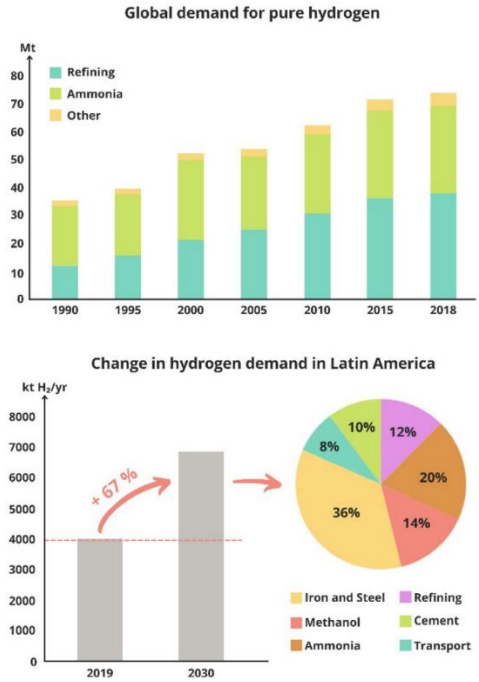

Figure 2. The chart describing the global demand for pure hydrogen (1990-2018) and the change in hydrogen demand in Latin America (2019-2030).[16,17,18,19]

Nonetheless, hydrogen environmental benefits depend on the way of production, which is determined by the Hydrogen Production Pathway (HPP). Therefore, the study and understanding of every HPP are essential for the development and advance of the so-called "hydrogen economy", mainly focused on the use of green hydrogen. During the analysis of HPP a few primary challenges must be conquered, such as the choice of the feedstock – (fossil fuel or water), the energy source needed to extract hydrogen from the feedstock and the catalyst that is needed to overcome some kinetic and thermodynamic limitations that are present regardless of the process.[8,20,21] A meticulous study on how to overcome these challenges can help with the development of an efficient and economical viable green HPP, which can contribute to a more sustainable future.

The level of cleanliness of the energy produced from hydrogen is related to the amount of greenhouse gases eliminated during the H_2 production. Furthermore, the sustainability of all energy chain also depends on the energetic input, the type of raw material, the design of the industrial process, and CO_2 emissions.[22,23]An interesting approach for classifying carbon emission during hydrogen production is the use of color labels. The color codes of the hydrogen production process might be the statement of sustainability from the suppliers to the consumers. This strategy allows a fast indication of the kind of hydrogen (in terms of carbon emission) you or a company are buying.

Therefore, it is expected an environmental responsibility and greater competitiveness from H_2 suppliers by sustainable products.[24,25]

The first proposed model for the H_2 classification is based on three colors, according to the CO_2 emission, as can be seen in **Figure 3**. Grey H_2 is produced through the steam reforming process and uses fossil fuels as raw material. In addition, there is no restriction to carbon emission, and it is considered "dirty" hydrogen. The process to produce Blue H_2 is like the grey one, however, the produced carbon is capture and stored, decreasing the CO_2 emissions. Other the other hand, green hydrogen is considered renewable hydrogen due to the use of water as a source of H_2 and renewable energy in the electrolytic process (water splitting process) what fits with the zero-emission carbon approach. **Figure 3** presents a comparative scheme of these three processes.[22,24,25]

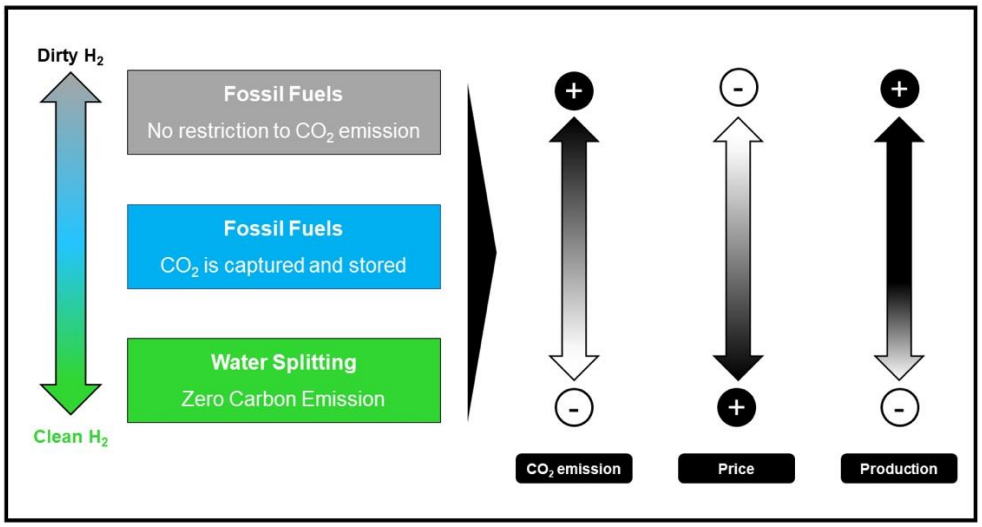

Figure 3. Scheme of three colors to classify the hydrogen production according to the carbon emission.

The H_2 chain is plural and complex and because of this, new color codes were added to improve the description of the cleanliness level of the hydrogen production. Based on this concept, a complete color codes table can be found in **Figure 4**.

The brown hydrogen (black hydrogen can be a synonym) is produced from coal in the gasification process, which generates large amounts of CO_2 and high environmental impact, even though the low cost of produced H_2 is hard to achieve. Gray and blue hydrogen were described before. Like the brown, blue, and gray hydrogen, turquoise hydrogen is also produced from fossil fuels, but the methane pyrolysis at high temperature allows the carbon elimination in solid form what reduces the CO_2 emission. The key point of this strategy is the source of energy that is used.

In other words, if the input energy is renewable, the process would be clean. Thus, it can have a lower environmental impact (**Figure 4**).

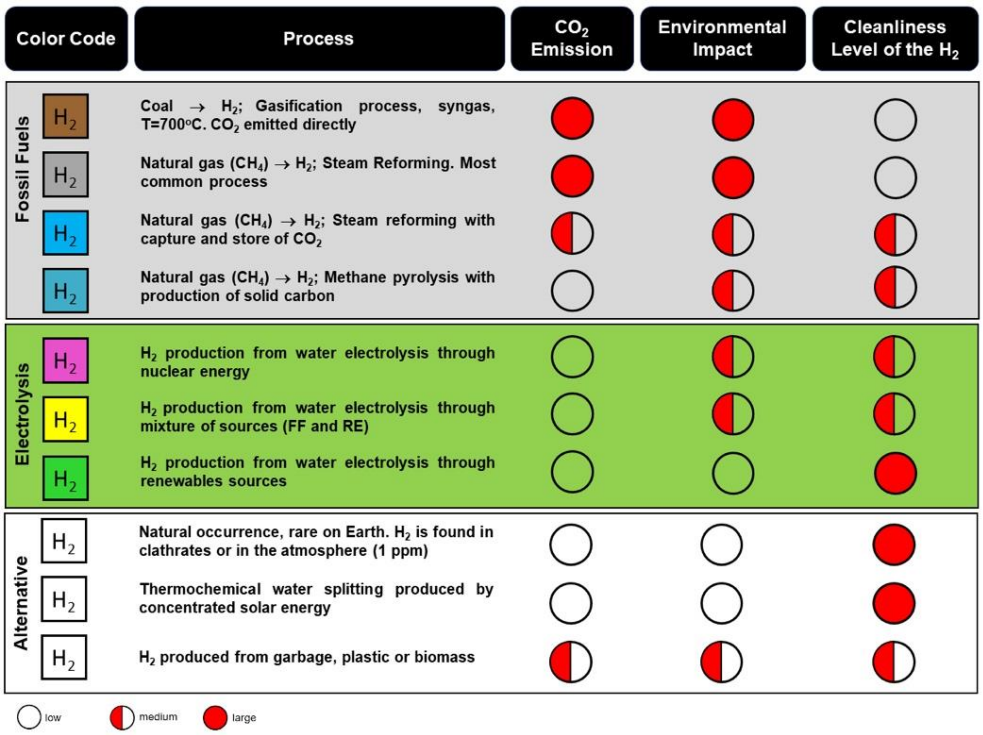

Figure 4. Color codes of hydrogen. Complete comparison among the processes according to the CO_2 emission, environmental impact, and cleanliness of the hydrogen produced; FF= fossil fuels and RE=renewable energy

Pink, yellow, and green hydrogen are produced from the electrolysis process (water splitting) and they use water as raw material. However, the final environmental impact depends also on the input energy. Pink hydrogen is obtained from the electrolysis process powered by nuclear energy and yellow uses the same strategy, but the H_2 is produced using the input of mixed origin (fossil fuel and renewable). Green hydrogen is produced by the cleanest process, where the water electrolysis is driven exclusively by renewable energy.[22] White color, for example, is used only to classify the H_2 from natural origin, and due to the rare occurrence on the Earth, there is no commercial interest.[26] This was the first proposal for the H_2-white. However, some authors have considered white hydrogen as a product of thermochemical water splitting produced by concentrated solar energy.[27] In addition, the company Recupera[28] has defined white hydrogen as H_2 produced from plastic, biomass, or garbage. The definition of white hydrogen is still opened.

In summary, the goal is to choose a HPP with a zero CO_2 emission, a low environmental impact, and a high cleanliness level of H_2. Thus, green hydrogen is produced by the cleanest process, where the water electrolysis is driven exclusively by renewable energy.[22] The challenge for incorporation of the green hydrogen in the hydrogen chain is the cost, since the price of sustainable hydrogen is approximately four times higher than those produced from the fossil fuels process.[20,29]

1.2. Green Hydrogen

The search for clean, renewable and environmentally friendly hydrogen sources has made water an excellent feedstock candidate to produce hydrogen.[30,31] The production of clean H_2 from water occurs by a system known as Water Splitting (WS), which in its simplest form uses an electrical current passing through 2 electrodes to complete the endergonic hydrolysis of water into hydrogen and oxygen. The overall process consists of two half reactions, in which the anodic process is called Oxygen Evolution Reaction (OER), where the Water Oxidation Reaction (WOR) takes place, and the cathodic process is known as Hydrogen Evolution Reaction (HER), where the hydrogen gas is produced, as it can be seen in the following reactions.[32–35]

$$Anodic\ Process: 2H_2O_{(l)} \rightarrow O_{2\,(aq)} + 4H^+_{(aq)} + 4\,e^- \qquad V_{ano} = 1.23V\ vs.RHE \quad (8)$$

$$Cathodic\ Process: 4\,H^+_{(aq)} + 4e^- \rightarrow 2\,H_{2\,(g)} \qquad V_{cat} = 0.00V\ vs.RHE \quad (9)$$

$$Global\ Process: 2H_2O_{(l)} \rightarrow O_{2\,(aq)} + 2\,H_{2\,(g)} \qquad V_{eq}\ 1.23V\ vs.RHE \quad (10)$$

The great limitation for hydrogen production through this process resides in the anodic reaction, where the oxygen evolution (water oxidation) takes place, which is the most energy-intensive and kinetically slow step in the overall water splitting process. The water oxidation process to oxygen implicates a complex electronic transfer involving 4 electrons and 4 protons.[36] Therefore, the water splitting is either kinetic and thermodynamic unfavorable, and in ideal conditions, a potential of 1.23V ($V_{equilibrium}$) must be applied to the system to start the process. In addition, efficient and stable catalysts are required to decrease the overpotential of the reaction

and an external energy source, such as electricity (electrolysis) or solar (photo-catalysis) must be used.[37,38]

The system where electrolysis of water takes place is known as electrolyzer, which basically consists of a cathode and an anode separated by a membrane immersed in an electrolyte. So far, three main electrolysis cells are used and studied: Alkaline Electrolysis Cells (AEC), Proton Exchange Membrane Electrolysis Cells (PEMEC) and Solid Oxide Electrolysis Cells (SOEC).[39] Figure 5 illustrates these cells set-up and their main differences.

AEC has been widely used for industrial and large-scale applications since 1920, being already available, stable and exhibiting a considerable low capital cost (around US$ 1180 / kW^{-1}).[40] Besides, this cell was shown to operate for over 55k hours, proving itself to be very stable, which is very important for this application. However, one of the main drawbacks for this cell is its low current density (<0.45 $A.cm^{-2}$) and high cell voltage (1.8-2.4V),[41–43] which can increase the cost for hydrogen production. Thus, some developments need to be done in order to make a more suitable cell, with a significant lower cost, which is still three times more expensive than steam reforming processes.[39,41,44,45]

PEMEC are based on a solid polymer electrolyte and they were developed in 1960 as an attempt to overcome the problems presented by the AECs, and they research has brought outstanding developments for electrolyzers applications.[45,46]

Membranes are the cornerstone for the PEMEC, and they are responsible for separating product gases, transporting protons, and supporting the cathode and anode catalyst layer. The most used membranes are based on a Perfluorosulfonic acid polymer, such as Nafion®, Fumapem®, Flemion® and Aciplex®.[41] Although all the beforehand cited polymers present great advantages for membrane applications, Nafion® is the one that usually is used, due to its excellent chemical and thermal stability, mechanical strength, high durability, high proton conductivity and the fact that it can operate at high current densities.[41,47,48] However, one of the main drawbacks for the use of Nafion® is its disposal, that can be very expensive due to the presence of fluorine in the structure. Thus, alternative membranes have been studied, yet they present low current densities and low durability, what make them unviable.[41,49]

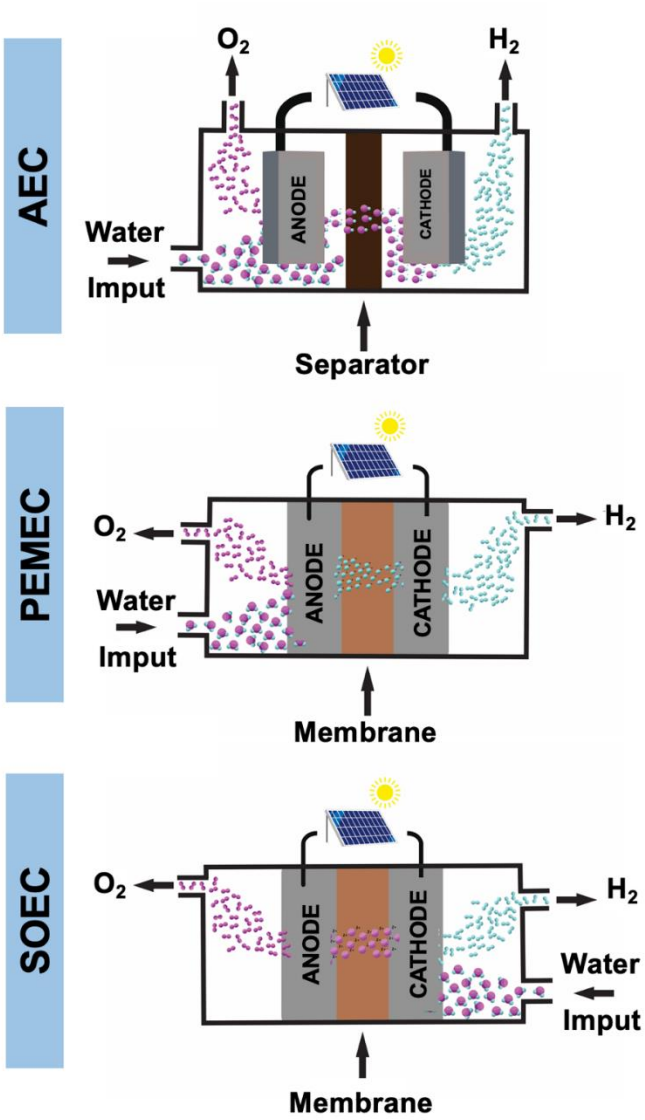

Figure 5. Main Electrolysis cells technologies set-up. They can be classified as: Alkaline Electrolysis Cells (AEC), Proton Exchange Membrane Electrolysis Cells (PEMEC) and Solid Oxide Electrolysis Cells (SOEC).[39]

Even in the same cell voltage as AFCs, PEMECs present high current density (1.0-2.0 $A.cm^{-2}$), efficiency and a great stability, operating for over 60k hours, being able to produce pure hydrogen. However, the main catalysts are made of noble metals, which increases the capital cost (around US$ 2300 / kW^{-1}).[42,43] The system also requires pure water, which limits its application. Hence, studies have been made trying to reduce the system complexity and its cost, aiming to find less expensive materials.[40,45,49]

SOEC is the more recent developed cell, and it is not widely commercialized since the system has demonstrated to work only on laboratory scales. The cell uses solid ion-conducting ceramics as the electrolyte, which allows it to operate at higher temperatures (900-1000 ºC).[46] These cells have high electrical efficiency, moderate current densities (0.3-1.0 $A.cm^{-2}$), operate at lower cell voltage (0.98-1.3 V),[42,43] low material cost and also the option to operate in reverse mode as a fuel cell or in co-electrolysis mode. Nonetheless, the high temperature operation can cause material degradation, which is a huge drawback and elevates the capital cost (higher than US$ 2400 / kW^{-1}). Therefore, the research in this area is focused on the development of catalyst materials that can be heated up to high temperatures and also on reducing the operating temperatures, in a way of making it commercially viable).[40,45,46,50]

Nevertheless, it is worth mentioning that all these data present for the electrolyzers are directly dependent on the stack level in the cells, which have an impact on the cells performance, efficiency and stability, therefore, it is an important parameter that is considered in the study of better systems for water electrolysis.[45]

In an overall water splitting electrochemical system the actual operational voltage (V_{op}) is different than the V_{eq} because it depends on the reaction's kinetics and on the cell design, being represented by the equation below:

$$V_{op} = V_{eq} + \eta_A + |\eta_C| + \eta_\Omega \qquad (11)$$

Where η_A and η_C are the overpotential for the anodic (OER) and cathodic (HER) reactions, and η_Ω is the additional overpotential required to compensate for resistance losses within the cell.[37] In an ideal system, η_A and η_C would be close to zero and the V_{op} would depend only on η_Ω, which could be minimized by the cell design. Nonetheless, this is not what happens in reality, in which the reactions face very high activation energy barrier due to the kinetics limitations, increasing the overpotential that needs to be overcome.[51] The system can become even more complex for photo-catalysis, where semiconductor materials are incorporated into the electrode in a way that the solar energy is directly harvested, requiring more mechanistic steps and lowering the overall production efficiency.[34,52] Thus, the research in water electrolysis processes focus on approaches to reduce this overpotential by improving electrodes, electrolytes and catalysts, trying to unravel ways to boost reaction kinetics.[33,38,53–56]

Among the numerous catalyst that have been studied, Ru, Ir and their respective oxides stood out as the state-of-art for water oxidation reaction, presenting the best electrocatalytic activities towards OER in both acidic and alkaline solution.[57] Ir, Ru and their respective oxides activity as water oxidation catalysts are ordered in the following sequence: Ru> Ir ≈ RuO_2> IrO_2. The overpotential needed to achieve a current density of 5.0 mA cm^{-2} is 300 and 400 mV for RuO_2 and IrO_2, respectively.[58] Even though both oxides have a good performance and activity during water oxidation, their main drawbacks are their low stability and high cost.[59]

The state-of-art catalysts for the hydrogen evolution reaction are based on Pt, which is found to be an efficient electrocatalyst, exhibiting a near to zero overpotential and high current densities.[35,60] Pt based catalysts present an overpotential of 0.05 V in acid media and are able to keep the same value even after 2 h of reaction. At an overpotential of 0.1 V, they are also able to achieve current densities of 110 ± 70 and 220 ± 80 mA cm^{-2} for two different studies with platinum electrodes, with differences in the electrolytes.[33,61]

Even though these catalysts are considered the state of art for water-splitting, their high cost and scarcity create a huge obstacle to their large-scale application. Hence, the development catalysts for HER and OER should be efficient, stable, cheap, operate at low overpotential, and based on earth-abundant elements. This is crucial to a suitable hydrogen generation through water splitting. In a view of that, an enormous amount of effort, both theoretical and experimental, has been put into the development of different catalysts based on earth abundant transition metals, especially from the first transition row (e.g. Co, Fe, Ni, Cu, Mn, Cr and Zn) as an attempt of substituting noble metals catalysts, making the water splitting an economic viable process for the hydrogen production.[32,33,35,38,55,56,62–66] Jaramillo *et al*.[33] published a study comparing the main catalyst for both OER and HER, working in alkaline and acid medium. In the paper, the authors present a benchmarking for these catalysts, showing how the activity of earth-abundant catalysts can be compared with the one from noble metals, demonstrating the main features that need to be improved for the development of suitable non-noble metal catalysts.

Even though a huge amount of research has been made in this area, the use of earth-abundant catalysts is still limited by their low activity and, most of the time, stability, which inhibit their applications for a large scale hydrogen production.[33–35]

Based on the development of the water splitting technology so far, the cost per kg of hydrogen is in the range of US$ 7.98 to 8.40 for electrolysis with an efficiency of up to 60% and

is about US$ 10.36 / kg for the photo-catalysis, and the efficiency up to 12%, what makes the electrolysis a better option for the water splitting. Nonetheless, this system is still too expensive, and the costs need to be reduced in order to be competitive with the grey hydrogen (steam reforming for example).[15,29,34,67]

Nonetheless, it is important to highlight that the Water Splitting process can only be considered a good and eco-friendly alternative for green H_2 production if the input energy in the electrolyzer is being supplied from renewable energy sources, otherwise, this system would not produce a 100% green and clean hydrogen.[21,68]

1.3. Prussian Blue

In the search for new catalysts classes, inorganic coordination polymers have emerged as a good alternative to address these challenges.[69] Among this new class of catalysts that have been studied, metal hexacyanoferrates represents an important part of it, where Prussian blue analogues (PBA) are a classic example.[4,70]

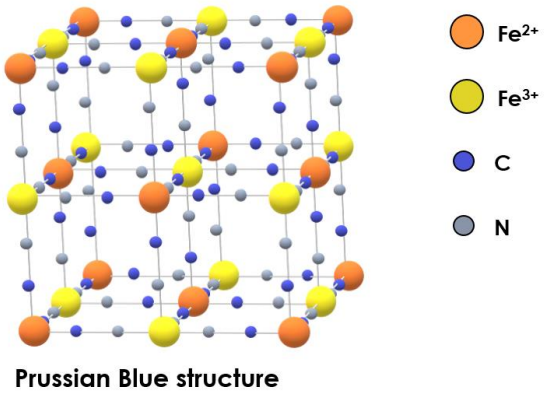

Figure 6. Prussian Blue main structure.

Prussian blue is the oldest synthetic coordination compound known, and it consists on a mixed-valence structure that holds both high and low spin oxidation states of iron on its structure, that is represented by $[Fe_4(Fe(CN)_6)_3]$, as presented in **Figure 6**.[71,72] The traditional proposed structure consists of two iron centers octahedrally coordinated, and linked by bridges with lattice constants varying from 10.13 to 10.18 Å.[73] The structure proposal assumes the N-coordinate center being Fe^{3+} and occupying the corners of a face-centered cubic (*fcc*) lattice of the crystal group

F4̄3m, while the C-coordinated center is Fe^{2+} and is at the middle of the edges.[73–75] Furthermore, some alkali-metal cations, usually potassium (K^+), is place within the structure to compensate the negative charges, and they occupy the half of the tetrahedral holes of the lattice.[73–75] Since cyanide C has a strong ligand field, Fe^{2+} assumes a diamagnetic low-spin d^6 configuration, whereas Fe^{3+} assumes a paramagnetic high-spin d^5 configuration linked to the weaker ligand field of cyanide N. Therefore, the strong blue color comes from the strong charge-transfer process that takes place between d^6 t_{2g} Fe^{2+}-C and hs d_5 t_{2g} Fe^{3+}-N, from where PB received its name.[76,77]

Moreover, the iron can be substituted by some other transition metals and an analogue structure known as Prussian blue analogues (PBA) can be obtained. PBAs are represented by $M_{1(x)}[M_2(CN)_6]_{(y)}$, where M_2 is an hexacyanometalate that plays a structural role and it can modulate the donor-acceptor effect to the other metal and M_1 a first-row transition metal and it is coordinated to the N atoms forming a 3D network.[78–80] This network adopts a face-centred cubic (*fcc*) structure in the *Fm3m* space group, with a cell parameter around to 10 Å. In the case of CoFe analogue, this material also presents the mixed spin/valence structure, and it is usually organized with Fe^{3+} d^5 in a low spin configuration, while Co^{2+} d^6 assumes the high spin configuration.[81,82] These materials have a wide range of applications,[69,78,80,83] and as catalysts, they had stood out due to its great performance and stability for the WOR in a neutral pH. Some studies have been carried out and report different PBAs performance and activity towards the WOR, however, most of them face the same problem, the low active sites that interfere with the catalytic activity.[35,36,83,84]

Despite their high stability and activity, the main shortcoming is their low concentration of active sites. Due to this, engineering the structure and defects is essential to lead to a high concentration of active sites, and consequently a higher catalytic activity.[69,84–86] Increasing the catalytic activity of a catalyst is the major challenge for scientists in many areas. In this sense, the modulation of defects in the catalysts can have direct impacts on their properties, like band structure tunning, conductivity, magnetism, and mainly in the performance. The most common known defect is the vacancy, which can lead to substantial structural perturbations in the catalysts, creating changes in the electronegativity, charge concentration, and redistribution, thus enhancing the catalyst activity.[87] A few researchers reported the generation of unusual cyanide vacancies in different PBAs using different methodologies, usually based on based on the use of extreme pH and temperature conditions, or even high energy plasma lasers, which exhibit low overpotentials

and high current densities for WOR in alkaline medium, exceeding the ones previously cited for the original Prussian blue analogues.[85,86,88]

1.4. Objectives

The main objective of this thesis is to investigate the electrochemical mechanisms of water oxidation using catalysts based on Prussian Blue analogues and to propose strategies to enhance their activity. The specific objectives of this research are as follows:

i. Propose a methodology to quantify iron for some iron-based catalysts thin films.
ii. Propose a strategy to overcome the PBA-based catalysts' main shortcoming of having low concentration of active sites.
iii. Investigate the active sites in Prussian Blue analogue catalysts, understanding how they work and the factors that influence their activity and performance towards OER.
iv. Investigate synchrotron-based soft X-ray spectroscopy techniques to probe the structure of PBAs and identify changes in the electronic configuration.

Chapter II

Photochemical Pre-Treatment to Quantify Iron in Thin Films

The content of Chapter II is an adaptation of the article entitled "Photochemical Pre-Treatment to Quantify Iron in Thin Films" by Rafael L. Germscheidt, Cleiber C. Morais, Danielle S. Francischini, Marco Aurélio Z. Arruda and Juliano A. Bonacin reprinted with permission from Journal of the Brazilian Chemical Society, Copyright ©2023 Sociedade Brasileira de Química, **Appendix C** and **D**.

Reference: J. Braz. Chem. Soc., Vol. 34, No. 7, 958-966, 2023. DOI: 10.21577/0103-5053.20230008.

Graphical Abstract

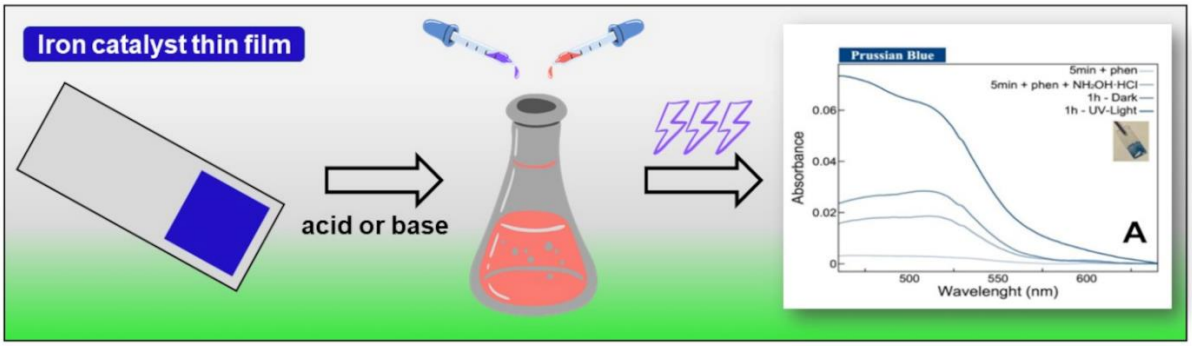

2.1 Introduction

The deposition of catalysts thin films on electrode surfaces is essential for heterogeneous electrocatalysis reactions. The evaluation of the metal content, numbers of active sites besides the level of conversion are extremely necessary to determine the efficiency, activity, and stability of a specific catalyst.[89,90] Parameters such as turnover number (TON), turnover frequency (TOF), and long-term stability depend on the quantification of active sites on the catalysts.[91,92]

Iron-based catalysts are widely used in the chemical industry. Furthermore, these catalysts produce outstanding activities and efficiencies in the water splitting process where the water is converted into green hydrogen.[89,93–96] These catalyst's activity and efficiency are directly related to the number of active sites, and it is usually linked to metal sites, as they facilitate electron transfer reactions and are the main responsible for the catalyst efficiency.[69,97–99] Thus, an accurate iron quantification is essential to evaluate an iron-based catalyst.

The determination of metal ions can be performed by several analytical techniques, such as atomic absorption spectroscopy (AAS), inductively coupled plasma optical emission spectrometry (ICP OES), inductively coupled plasma mass spectrometry (ICP-MS),[100,101] and spectrophotometry (UV/Vis).[102] Among these techniques, spectrophotometry stands out for being simple, efficient, fast, and presenting low cost for both sample preparation and equipment maintenance. Besides, its spectra is very simple to be interpreted.[103–106] The spectrophotometric determination in the UV-VIS region generally requires the use of other compounds to trigger some changes in the species of interest (analytes), in order to increase the analytical sensitivity and selectivity.[102,106]

Given this scenario, the biggest challenge to calculate the amount of iron in these catalysts is the fact that most of them are based on complexed structures and/or molecules, where the iron atoms are complexed with different ligands. Therefore, an additional sample preparation step is required before performing spectrophotometric analysis. This is an important step, and it is responsible for providing a dissociation of the iron ion from its ligands and allowing its coordination with the compound responsible for increasing the analytical sensitivity and selectivity, typically 1,10-phenanthroline for iron quantification.

There are different methods presented in the literature for sample preparation for elemental analysis, including the use of ultrasonic waves, acid digestion, high temperature hydrolysis,

microwave radiation degradation, the use of organic solvents, combustion and finally photochemical methods using UV light.[107–110] The use of photolysis, a photochemical process that uses light (UV or Visible)[111] stands out as a fast, cheap and environmentally friendly method, using only energy source and no side solvent or heating source to easily promote the complex dissociation by labializing the main ligands.[108,112] Hance, photolysis has been widely applied in the last years to dissociate Fe ions from complex structures and/or molecules, allowing an effective labialization of different ligands, such as cyanide (CN^-), oxides, organic ligands, chloride (Cl^-) and so on.[108,112,112–116]

Therefore, herein we present a photolabilization strategy of iron to allow precise quantification of this metal from some iron-based catalysts, such as Prussian blue, cobalt-iron Prussian blue analog, hematite, nickel-iron oxyhydroxide, and cobalt-iron oxide.

2.2 Experimental Section

2.2.1 Catalyst preparation and GCE modification

Before the catalyst's film deposition, FTO substrates of 1 × 2.5 cm^2 were cleaned using isopropyl alcohol in an ultrasonic bath for 10 minutes, rinsed with distilled water, and cleaned again in an ultrasonic bath using distilled water for 10 minutes. After that, the substrates were annealed in a muffle at 400 °C for 30 minutes.[69]

2.2.1.1 Hematite (Fe_2O_3)

Hematite films were obtained by immersing the electrode in a solution containing 0.1 mol L^{-1} of $FeSO_4$, 0.1 mol L^{-1} of $FeCl_3$. Then metallic iron was reduced over the electrode surface by applying a constant potential of -1.1 V x SCE for 300 s. The electrode was dried and then, the film was submitted to thermal treatment in a muffle at 400 ºC for 150 minutes.

2.2.1.2 Bimetallic hydroxide (NiFe(oxy)OH)

Bimetallic hydroxide films were obtained according to the method previously reported by our group.[117] Since the goal of this work was only the iron quantification in the catalyst, following the methodology, we also used 3D printed electrodes for the deposition of NiFeOOH catalyst. The electrode activation process was also followed before the catalyst deposition. Then, the electrode

was immersed in a solution containing 90 % of $NiSO_4$ and 10 % of $FeSO_4$ with the total metal content of 10 mol L^{-1}. Electrodeposition was carried out by chronopotentiometry as previously reported, by applying a cathodic current density of 50 μA cm^{-2} for 1125 s.

2.2.1.3 Prussian Blue (PB)

Prussian Blue films were obtained by immersing the electrode in a solution containing 1 mmol L^{-1} of $[Fe(CN)_6]^{3-}$, 1 mmol L^{-1} of $FeCl_3$, 0.1 mol L^{-1} of KNO_3, and 0.1 mol L^{-1} of HCl. Then 10 cycles were performed from 0.37 to 0.8 V X SCE, on a scan rate of 8 mV s^{-1}. After this, a blue film was observed on the electrode.

2.2.1.4 CoFe Prussian Blue analogues (CoFePBA)

CoFePBA films were obtained as reported. Cobalt(II) chloride (12 mmol) was dissolved in 80 mL of Milli-Q water to form a solution A. Potassium hexacyanoferrate(III) (8 mmol) was dissolved in 80 mL of Milli-Q water to form a solution B. Then, solution A was added into solution B under magnetic stirring for 1 hour. After continuous stirring for 2 hours, the homogeneous solution was maintained at a low temperature for 12 hours. The precipitate was collected by centrifugation and exhaustively washed with Mili-Q water to ensure the removal of any trace of precursors and after this, the solid was dried at 60 °C overnight. The films were prepared by a drop-casting method. The ink of catalyst was prepared by a mixture of the solid compounds (5 mg), Milli-Q water (100 μL), DMF (200 μL), and Nafion® (20 μL). Then, the mixture was sonicated for 30 min to obtain a homogeneous ink and 25 μL of the ink was dropped into an FTO electrode to cover a 1 cm^2 area. The electrodes were dried at a vacuum system to remove the solvent.

2.2.1.5 CoFe oxide ($CoFeO_x$)

CoFe oxide was obtained from the CoFePBA framework. So, the modified electrode was submitted to thermal treatment in a muffle at 400 ºC for 150 minutes.

2.2.2 Preparation for iron quantification

Prior to the iron determination methodology, the oxide films were dissolved with 5 mL of a 0.1 mol L^{-1} hydrofluoric acid (HF) solution, and the Prussian blue films dissolved with 5 mL of a 0.1 mol L^{-1} sodium hydroxide (NaOH) solution, in an ultrasonic bath, to assure complete removal

of the film. The obtained solutions were transferred to 25 mL volumetric flasks. These final solutions were then used for the Fe determination analysis.

2.2.3 Electronic Spectroscopy

Spectra of aqueous solutions in the UV–Visible region were obtained using a Bel Photonics UV-M51 UV–visible absorption spectrophotometer, with a 1 cm quartz cuvette, in the region from 200 to 600 nm.

2.2.4 Calibration Curve Validation

The limit of detection (LOD) for this calibration was obtained from the standard deviation of the blank, according to Equation 1, where F is a factor of 3.3, SD is the standard deviation of the blank (0.00046) and b is the slope of the regression line. And the limit of quantification (LOQ) was also obtained from the standard deviation of the blank, according to Equation 2.[118,119]

$$\mathrm{LOD} = \frac{\mathrm{F\ x\ SD}}{\mathrm{b}} \qquad (\textbf{Equation 1})$$

$$\mathrm{LOQ} = \frac{\mathrm{10\ x\ SD}}{\mathrm{b}} \qquad (\textbf{Equation 2})$$

The obtained results for LOD and LOQ were 1.3132 x 10^{-7} and 3.8163 x 10^{-7}, respectively, which are smaller than the calibration curve first point (1.18402 x 10^{-6}), thus, the obtained calibration curve is accurate for these concentrations.

Aiming to ensure that the amount of iron was accurate the method was tested with iron samples spiked at two levels of concentration (200.0 and 1.000 μmol L^{-1}). For this, solutions with a known concentration of iron chloride ($FeCl_3$) were prepared, mixed with phenanthroline and an excess of $NH_2OH{\bullet}HCl$ (to reduce Fe^{3+} to Fe^{2+}), and analyzed by the calibration curve. $FeCl_3$ was chosen since it is an easily soluble salt, dissociating into Fe^{3+} and Cl^- in solution, therefore, having all iron atoms free in solution to be coordinated with phenanthroline, after being reduced to Fe^{2+}.

2.2.5 Accuracy check for Fe quantification by Inductively Coupled Plasma Mass Spectrometry (ICP-MS)

2.2.5.1 Sample Preparation

By a solution content 1000 ng mL^{-1} of $[Fe(CN_6)]^{4-}$, six solutions with different Fe concentration were prepared: 100, 150, and 200 ng mL^{-1}. Each final solution was acidified to 2 % (v/v) of sub-distilled HNO_3 (14.3 mol L^{-1}) in deionized water (18 MΩ cm^{-1}, Millipore, Bedford, USA). The analytical curve to Fe quantification was prepared in 2 % (v/v) HNO_3 solution with the following concentrations: 0, 1, 5, 10, 15, 20, 30, 60, 100, 150, and 250 ng mL^{-1} using Fe from ICP-MS standard solution (SRM 3126a – SpecSol, NIST USA). The ^{54}Fe, ^{56}Fe, and ^{57}Fe isotopes were evaluated to verify the ideal analytical parameters such as linearity, LOD and LOQ, as also the analytical recovery (80 – 12 0%).

2.2.5.2 ICP-MS Instrumental Parameters

The analysis was performed via ICP-MS (iCAP TQ, Thermo Fisher Scientific), in high sensitivity mode single quadrupole (SQ), using He gas as the collision gas to interference removal and kinetic energy discrimination (SQ-KED). The Ar gas was used as the nebulizer gas. Prior to the analysis, the equipment was daily checked for oxides and double-charged ion formation below 4%, being within the ideal working limit. The instrumental parameters of analysis were: 0.9943 L min^{-1} as nebulizer gas flow, 0.80 L min^{-1} as auxiliary gas flow, 4.425 mL min^{-1} as He gas flow, and 1550 W as radiofrequency power.

2.2.5.3 ICP-MS Results

According to the results obtained for each Fe isotope (**Table 1**), ^{56}Fe showed results closest to optimal analytical recovery value (80 – 120 %), adequate linearity (R>0.99), and low LOD and LOQ values, thus being chosen to evaluate the iron concentration in the samples of interest.

Table 1. Figures of merit to Fe quantification

	Analytical curve		
	^{54}Fe	^{56}Fe	^{57}Fe
y = ax + b	y = 3312x + 32209	y = 59497x + 593350	y = 1561x + 14245
R	0.9951	0.9945	0.9950
LOD[a] (cps)	0.28	0.31	0.39
LOQ[b] (cps)	0.95	1.04	1.29
Recovery (%)	82.8	**87.1**	71.5

[a]Limit of Detection; [b]Limit of quantification

2.3 Results and Discussion

2.3.1 Fe concentration calibration

The use of phen to quantify Fe^{2+} ions is a well-known method since this bidentate chelating agent has two nitrogen atoms at the ortho positions of the rigid half-ring structure, which can coordinate with Fe^{2+} ions, forming a complex,[102] as it can be seen in **Figure 7a**. This molecule is known as a π-acceptor ligand and its coordination with Fe^{2+} produces a specific color in the visible region (orange-red color) assigned, as mentioned before, to metal-to-ligand charge transferences (Fe(*d*) → phen (π*)). In the $[Fe(phen)_3]^{2+}$ complex, the metal d-orbitals will give rise to the highest occupied molecular orbitals (HOMO), while the p-orbitals from the carbon and nitrogen in the phen, will give rise to the lowest unoccupied molecular orbitals (LUMO), **Figure 7a.** The absorption band on the UV-Vis electronic spectrum of $[Fe(phen)_3]^{2+}$ (**Figure 7b**) in a smaller wavelength, 267 nm, can be assigned to the intraligand π → π* transitions for phen. Furthermore, the adsorption bands identified in higher wavelengths, 475 and 510 nm, can be assigned to the metal to ligand charge transference (MLCT) Fe(*d*) → phen (π*) transitions. The maximum absorbance for the MLCT transition is found around 510 nm and its intensity is directly proportional to the $[Fe(phen)_3]^{2+}$ complex concentration in the solution.[120,121]

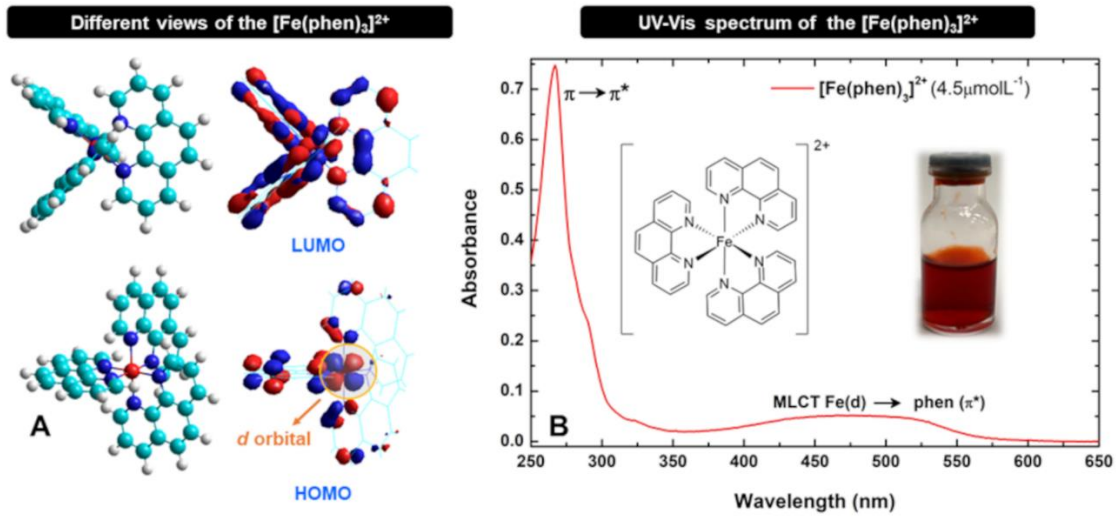

Figure 7. A) Structure of the $[Fe(phen)_3]^{2+}$ complex and its frontiers orbitals; **B)** UV-Vis electronic spectrum of $[Fe(phen)_3]^{2+}$ (concentration: 4.5 μmol L^{-1}) and picture of a concentrated solution of the complex.

The $[Fe(phen)_3]^{2+}$ complex is produced immediately in the presence of Fe^{2+} ions and phen in an aqueous solution and it can be easily detected by UV-Vis spectroscopy. However, its formation does not occur instantly if the iron ions are already complexed with other ligands, which is the case for some iron-based catalysts, such as Prussian Blue (PB), hematite, or some iron oxyhydroxide. Thereby, it is not possible to use this methodology directly to quantify the amount of iron in these samples due to their low dissociation kinetics and solubility product constant.

Prussian Blue, for example, is a kind of coordination compound formed by the mixture of Fe^{3+} and $[Fe(CN)_6]^{4-}$ and its structure and analogues are widely studied to be used as catalysts.[4] In this case, Fe^{3+} ions coordinate with N of the cyanide group to produce a 3D framework. The called "insoluble Prussian blue" ($Fe_4[Fe(CN)_6]_3 \bullet nH_2O$) is a very stable blue solid, and it has the value of K_{ps}= 3 x 10^{-41}.[122] Considering the evaluation of the iron content in a PB film, the first step to analyze this metal content in a thin film is to solubilize the material. This step can be easily done in this case with an alkaline solution. During the solubilization, Fe^{3+} (can produce a hydroxy/oxo) and $[Fe(CN)_6]^{4-}$ are formed. Then, it is necessary to replace the cyanide ligand by phen.

Studies show that although these aqueous complexes dissociate slowly in the darkness, upon exposure to UV light they can dissociate easily, releasing cyanide.[108,112] Given this motivation, $[Fe(CN)_6]^{4-}$ solutions were initially used to obtain a pattern for the iron concentration when complexed with phenanthroline, acquiring a calibration curve in different concentrations, from 1.2 x 10^{-6} to 7.1 x 10^{-4} mol L^{-1}, as seen in **Figure 11**. The solutions were submitted to UV-A

light incidence for 1 h, in a photoreactor (**Figure 8**). This light provides the necessary energy for the complex dissociation to happen and consequently the complexation with phenanthroline present in the solution. After 1h, it was possible to observe a change in the color, with an orange-red color appearance (**Figure 9**), with a color intensity related to the sample concentration, as can be seen in **Figure 11a**. Besides, it was also possible to identify the band related to the $[Fe(phen)_3]^{2+}$ complex in the UV-Vis spectrum at 510 nm (**Figure 11b**).

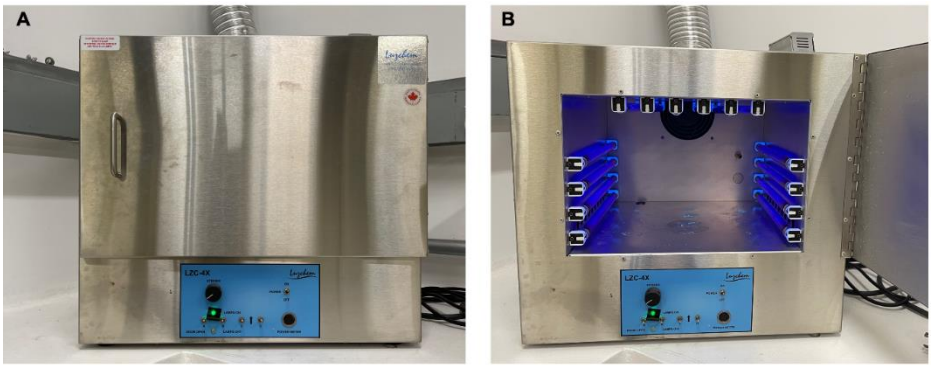

Figure 8. Commercial LuzChem LZC-4X UV Light reactor with 14 UV-light.

Figure 9. $[Fe(CN)_6]^{4-}$ solutions with phen before (left) and after (right) the exposure to the UV-Light.

The comparison among the UV-A light wavelength, the intensity and the $[Fe(CN)_6]^{4-}$ UV-Vis spectrum (**Figure 10a**) allows a discussion about the mechanism of the reaction. As it can be seen, the $[Fe(CN)_6]^{4-}$ spectrum has a characteristic band at 330 nm, which can be assigned to the $^1T_{1g} \rightarrow {}^1A_{1g}$ transition.[123,124] The UV-light wavelength ranges from 297 to 422 nm, and the part

that overlaps with the $[Fe(CN)_6]^{4-}$ absorption band is around 297-365 nm. This shows a direct overlap between the UV-light absorption bands and the band interactions between iron and cyanide. Based on this, two different possible UV-light-dependent mechanisms were suggested in **Figure 10b**, and both of them can happen and contribute to the formation of the $[Fe(phen)_3]^{2+}$ complex. In the first proposal, the UV-light exposure contributes to the dissociation of $[Fe(CN)_6]^{4-}$, which results in the formation of $[Fe(OH_2)_6]^{4-}$. Then, this complex, in the presence of phenanthroline and by a substitution mechanism, changes the ligands and forms the complex of interest, $[Fe(phen)_3]^{2+}$. The other possibility is the dissociation by the UV-light exposure with a direct complexation of iron and phenanthroline, without the need for the intermediate aquo complex.

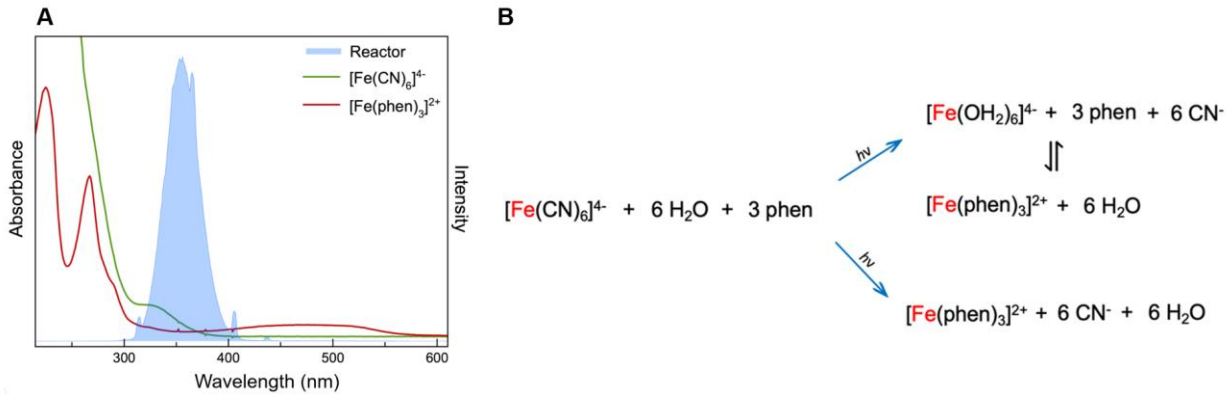

Figure 10. A) UV-Vis spectrum of $[Fe(CN)_6]^{4-}$ solutions (green line), after its complexation with phenanthroline, $[Fe(phen)_3]^{2+}$ (red line) and wavelength intensity spectrum of the UVA-light reactor (blue). B) Mechanism proposal scheme for the formation of $[Fe(phen)_3]^{2+}$ from $[Fe(CN)_6]^{4-}$ after UV-light exposure.

After the complex formation by the UV-light exposure, the band was identified on the UV-Vis spectrum, and this band absorbance intensity was related with the Fe concentration, allowing the obtention of a linear calibration curve, with an $R^2 = 0{,}9997$ (**Figure 11**).

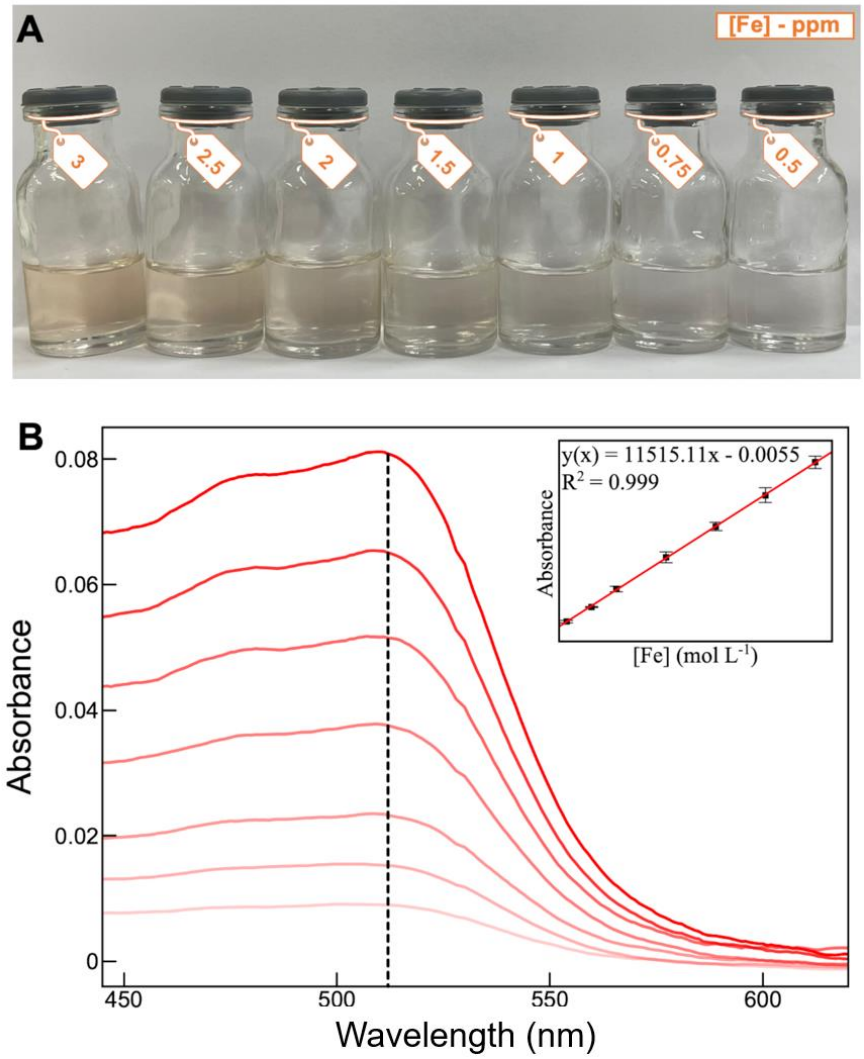

Figure 11. A) Solutions of $[Fe(CN_6)]^{4-}$ in different concentrations (from 0.5 to 3 ppm) after the exposure to UV light; **B)** Calibration curve for $[Fe(CN_6)]^{4-}$ with phenanthroline and UV-Light incitation. Insert indicates the obtained calibration curve with an error bar obtained from n=3.

To obtain a more accurate result on the iron quantification, which is an extremely important factor for the TON or TOF calculation, for example, the calibration curve was obtained 3 different times, using different solutions. The results were similar, and the amount of iron was calculated using an average of the 3 analyses:

$$y(x) = 11515x - 0.0055$$

The calibration curve was validated and tested with spiked iron sample, and through the limit of detection (LOD) and limit of quantification (LOQ), and more details can be seen in the experimental section. The obtained result for LOD and LOQ were 1.3132 x 10^{-7} and 3.8163 x 10^{-7}, respectively, which are smaller than the calibration curve first point (1.18402 x 10^{-6}), thus, the obtained calibration curve is accurate for these concentrations. As it can be seen in **Table 2** and **Figure 12**, for the spiked samples, satisfactory recovery values of 97.56 and 96.10 % were obtained for both evaluated samples, indicating an effective determination of Fe without significant matrix effects.

Table 2. Iron quantification using $FeCl_3$, NH_2OH•HCl and phen by the proposed method (n=3).

Added (µmol/L)	Found (µmol/L)	Recovery (%)
200.0	192.0 ± 0.250	97.56
1.000	0.960 ± 0.035	96.10

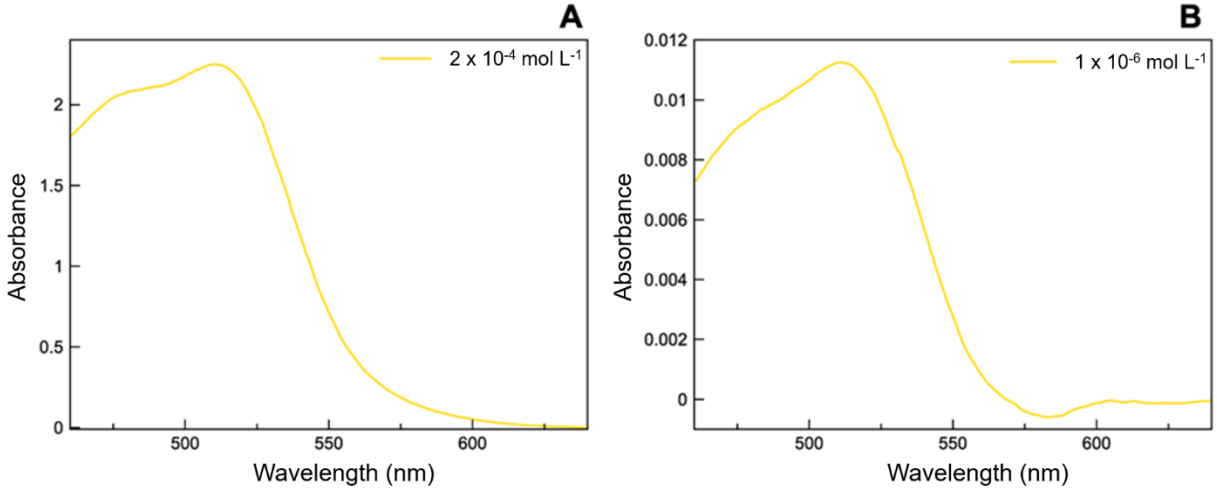

Figure 12. UV-Vis spectrum of $FeCl_3$ solutions in different concentrations. (A) 2 x 10^{-4} mol L^{-1}; (B) 1 x 10^{-6} mol L^{-1}.

Furthermore, the accuracy was checked by comparing the quantification of iron also with ICP-MS analysis and the method details can be found on the experimental section. The same samples were also analyzed by the technique proposed by this paper, and a comparison between the results can be seen in **Table 3** and **Figure 13.** The results indicate an accurate determination of Fe with the proposed technique, validating the method with ICP-MS recoveries ranging from 90 to 120 %.

Table 3. Comparison between ICP-MS and UV-Vis.

ICP-MS[a] (nmol)	UV-Vis (nmol)	Recovery ICP-MS (%)
19.47 ± 0.06	18.47 ± 0.33	94.83
27.07 ± 0.14	24.53 ± 0.09	90.64
34.26 ± 0.42	39.73 ± 1.81	116.0

[a]inductively coupled plasma mass spectrometry

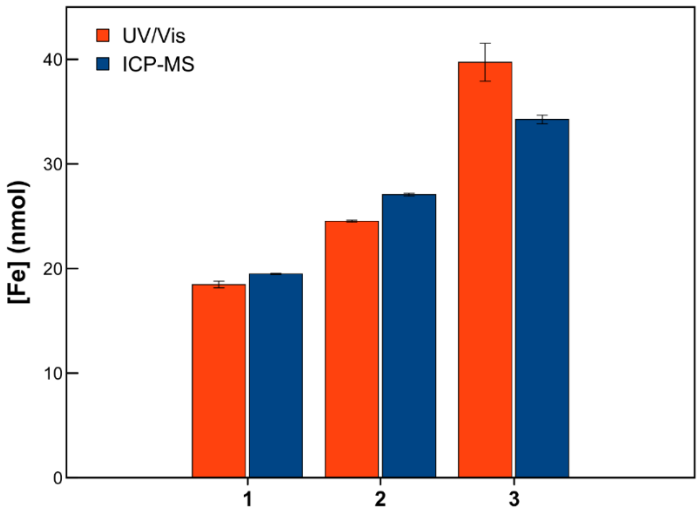

Figure 13. Quantification comparison between ICP-MS and UV-Vis. Numbers on x axis (1, 2 and 3) represent the 3 samples that were tested for the method validation.

2.3.2 Iron quantification in different catalysts

After the calibration curve preparation and testing with $FeCl_3$ and $[Fe(CN)_6]^{4-}$ + UV-A light, the method was applied for the iron determination in a Prussian Blue catalyst. The PB film was prepared and dissolved with NaOH into a solution to be analyzed, according to the details provided in the experimental section.

The study for the determination of the total iron amount was carried out in 4 different conditions. Firstly, the catalyst solutions were analyzed only with the addition of phen, which can indicate the amount of free Fe^{2+} at the beginning of the reaction (*5 min + phen*). Then, an excess of a reducing agent (hydroxylammonium chloride - $NH_2OH{\bullet}HCl$) was added to the solution to make sure that all free iron was converted into Fe^{2+} (*5 min + phen +* $NH_2OH{\bullet}HCl$). Furthermore, the second solution (*5 min + phen +* $NH_2OH{\bullet}HCl$) was split into two others. One of them was kept

in dark for 1h (*1h – Dark - phen + NH_2OH•HCl*) and the other was added into the UV reactor for UV-light exposure (1h – UV – phen + NH_2OH•HCl). In this way, we were able to evaluate the UV-light exposure effect. The results can be seen in **Figure 14**, **Table 4**, and **Table 5**.

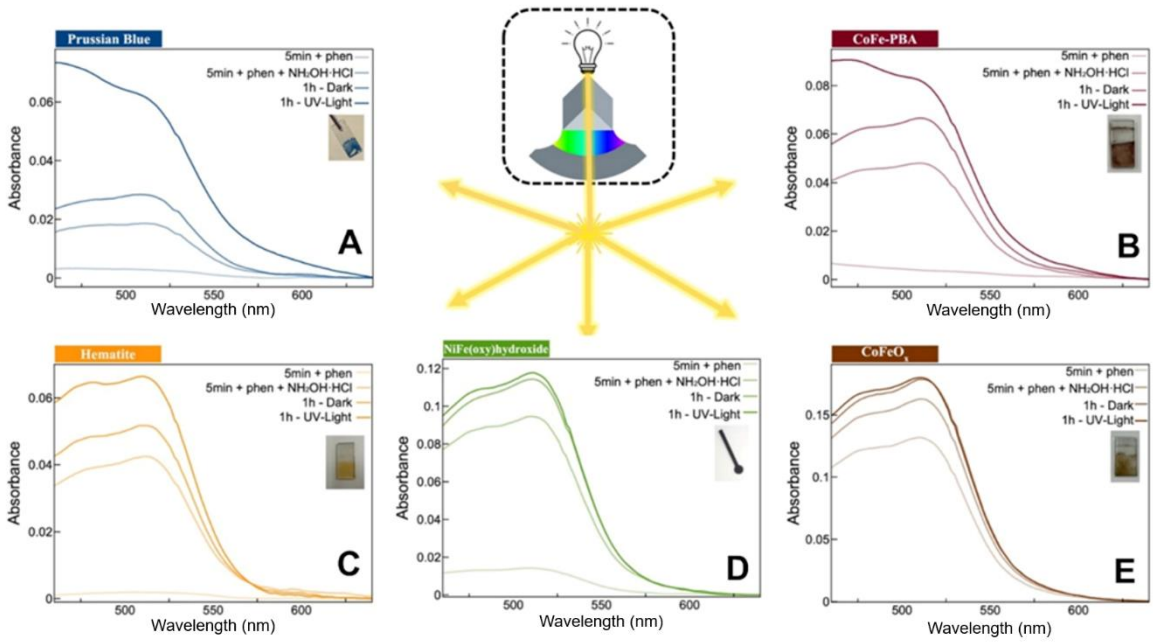

Figure 14. UV-Vis electronic spectrum for iron determination on catalysts. **A)** Prussian Blue; **B)** Co-Fe Prussian Blue analogue (CoFe-PBA); **C)** Hematite (Fe_2O_3); **D)** Ni-Fe (oxy)hydroxide ($NiFe_xOOH$); **E)** Co-Fe oxide ($CoFeO_x$) in different conditions.

The PB structure was shown to be very stable, and its initial analysis showed an amount of iron of 17.15 ± 1.60 nmol and 21.54 ± 1.06 nmol for only phenanthroline addition and after the addition of NH_2OH•HCl, respectively. This small amount of Fe^{2+} free, in the beginning, proves the need for an external energy source to help with the Fe^{2+} dissociation, after 1h, it was possible to observe an increase in the iron amount, 51.45 ± 0.33 and 145.5 ± 4.0 nmol, for dark and UV-light exposure, respectively. The results are presented in **Table 4**.

The $[Fe(phen)_3]^{2+}$ formation mechanism would be the same as the one proposed for $[Fe(CN)_6]^{4-}$ (**Figure S4**). Thus, this method can be suitable to quantify iron in the Prussian blue structure, as long the solution is exposed to UV-light for 1h before the analysis. This approach ensures the total dissociation of iron from cyanide, allowing the obtention of precise iron

quantification. This final iron amount, in nmol, could be further used to calculate TOF and evaluate the catalyst's activity and efficiency, for example.

Table 4. Iron concentration in nmol for each catalyst in different conditions of analysis (n=3)

	Prussian Blue	**CoFePBA**	**Fe_2O_3**	**NiFe(oxy)OH**	**$CoFeO_x$**
5min – Without $NH_2OH.HCl$	17.15 ± 1.60	6.180 ± 0.040	14.33 ± 0.45	41.48 ± 1.21	297.2 ± 1.1
5min – With $NH_2OH.HCl$	21.54 ± 1.06	36.82 ± 0.05	104.2 ± 0.8	215.6 ± 0.5	364.1 ± 0.5
1h – Dark	51.45 ± 0.33	155.5 ± 0.1	124.2 ± 3.2	260.7 ± 0.1	398.0 ± 3.2
1h – UV-Light	145.5 ± 4.0	190.8 ± 0.9	157.2 ± 1.9	266.4 ± 0.7	400.6 ± 0.5

Since the quantification method was shown to be highly effective for PB thin films, the same method was applied for the study and quantification of a PB analog prepared with cobalt and iron. CoFe-PBA is an analog to the Prussian blue, in which Fe^{3+} can be substituted by Co^{2+}, being represented by $Co_3[Fe(CN)_6)_2]\bullet nH_2O$. These Co-PBA stand out for their great activity towards the oxygen evolution reaction since their high conductivity gives rise to exposure of more active sites and facilities the electron transfer during oxygen evolution reaction.[69,83,125] Its structure was also shown to be very stable in the beginning, and its initial analysis showed an amount of iron of 6.180 ± 0.040 and 36.82 ± 0.05 nmol for only phenanthroline addition and after the addition of $NH_2OH\bullet HCl$, respectively.

This indicates that a low content of iron was available at the beginning of the reaction to be coordinated with phen. This small amount of iron available in the beginning indicates a similar behavior to PB and the need for UV-light exposure to allow iron dissociation. After 1h, it is possible to observe an increase in the iron amount, 155.5 ± 0.1 and 190.8 ± 0.9 nmol, for dark and UV-light exposure, respectively. These results indicate that UV-light exposure contributes to the total dissociation of iron from cyanide. The $[Fe(phen)_3]^{2+}$ complex formation mechanism would be the same as the one proposed for $[Fe(CN)_6]^{4-}$ (**Figure 10b**), and both proposals, with and without the formation of the aquo intermediate would be possible. Moreover, as it can be seen in **Figure 15**, the cobalt-phenanthroline complex has absorption bands around 200 and 294 nm, and it does not present any band close to 510 nm, therefore, even if some phenanthroline is present in the solution

is being coordinated to Co, it does not interfere with the iron quantification. Thus, this method can also be considered suitable for iron quantification on PBAs thin films, with precise and accurate results, see **Table 4** and **Figure 14**.

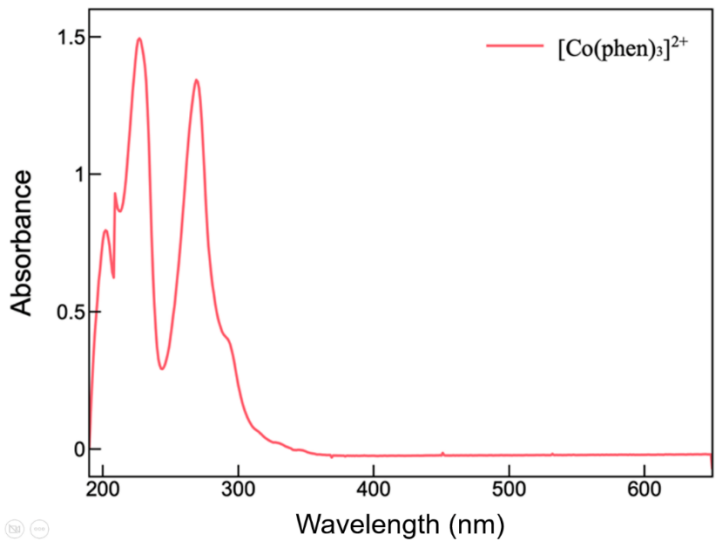

Figure 15. UV-Vis electronic spectrum of $[Co(phen)_3]^{2+}$ solution.

Considering the obtained results for PB and PBA, the method was also applied for iron quantification in other iron-based catalyst's thin films, such as Hematite (Fe_2O_3), bimetallic Ni-Fe oxyhydroxide (NiFeOOH), and a bimetallic CoFe oxide (CoFeOx), and the film preparation details can be found in the experimental section.

Hematite (**Figure 14c**) has a rhombohedral structure, consisting of an intense structure connected to the Fe^{3+} cation in octahedral coordination with oxygen in the hexagonal closed packing system, and it is widely used as a catalyst.[126,127] The predominance of Fe^{3+} in the structure was proven by the first analysis, by only adding phenanthroline, in which the amount of iron present was 14.33 ± 0.45 nmol, and after the addition of NH_2OH•HCl, the iron amount increased to 104.2 ± 0.8 nmol. After 1h, it is possible to observe an increase in the iron amount, 124.2 ± 3.2 and 157.2 ± 1.9 nmol, for dark and UV-light exposure, respectively. In **Table 4** is possible to see all results.

This result indicates that the UV-light exposure ensures the total amount of iron quantification, assuring that every iron atom is free to be coordinated with phenanthroline. However, the absence of UV-light (dark) also allowed a high amount of free iron after 1h (**Table 4**). Two pathways could be proposed to happen during the metal labilization and coordination of Fe^{2+} with phen. One is based on UV-light labilization and the other takes place in the dark (**Figure**

16b). The mechanisms were proposed according to the association between the UV-light reactor wavelength intensity and the Fe_2O_3 absorption spectrum (**Figure 16a**).

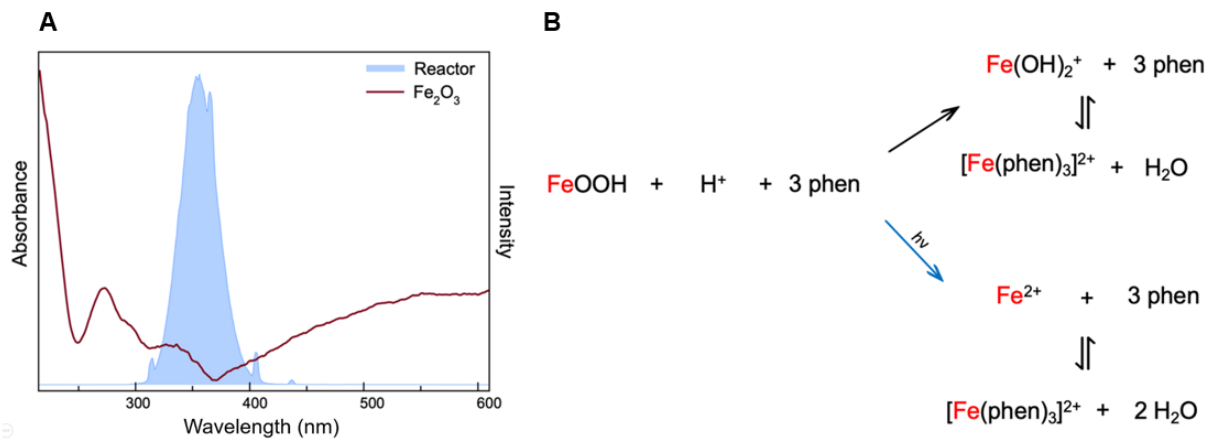

Figure 16. A) UV-Vis spectrum of Fe_2O_3 solutions (dark red line), and wavelength intensity spectrum of the UVA-light reactor (blue). B) Mechanism proposal scheme for the formation of $[Fe(phen)_3]^{2+}$ from Fe_2O_3 accounting for dark reaction and UV-light exposure.

As can be seen, the hematite spectrum has characteristics bands at 270, 294, and 333 nm. These bands can be assigned to the ligand-to-metal charge-transfer transitions and partly from the contributions of the Fe^{3+} ligand field transition $^6A_1 \rightarrow {}^4T_1$ (^4P), $^6A_1 \rightarrow {}^4E$ (^4D), and $^6A_1 \rightarrow {}^4T_2$ (^4D).[128,129] The UV light reactor wavelength ranges from 297 to 422 nm, and the part that overlaps with the hematite absorption bands is around 297- 365 nm, comprising UV wavelengths, having a direct effect on the band interactions between iron and oxygen.

Based on that, for the time-dependent mechanism, it is believed that in solution, the iron oxide forms FeOOH, and in the presence of acid (H^+), it can form $Fe(OH)_2^+$; then, by a ligand substitution reaction, in the presence of phenanthroline, can form the color complex $[Fe(phen)_3]^{2+}$. Thus, this method is also observed as a suitable method for iron quantification in Hematite films, presenting promising results. Furthermore, even though UV-light exposure does not have a greater effect on the iron dissociation, it is still necessary to ensure a total quantification of iron, as it can be seen in **Table 4**.

Ni(oxy)hydroxides (**Figure 14d**) were also studied since they are well-known structures with a wide application as catalysts, especially for the water oxidation reaction. Also, its activity had been shown to increase when doped with other first-row transition metals, particularly iron.

And since the catalyst activity is directly related to the amount of iron that is present in the structure, iron quantification in these catalysts is essential.[117,130] The predominance of Fe^{3+} was also found in this structure, since by only adding phenanthroline the amount of iron present was 41.48 ± 1.21 nmol, and after the addition of NH_2OH•HCl, the iron amount increased to 215.6 ± 0.5 nmol. After 1h, it is possible to observe an increase in the iron amount, 260.7 ± 0.1 and 266.6 ± 0.7 nmol, for dark and UV-light exposure, respectively. The results indicate that the UV-light effect in the dissociation of iron is almost neglectable, being responsible for only 2.22% of the total amount of iron (**Table 5**). The $[Fe(phen)_3]^{2+}$ complex formation mechanism would be the same as the one proposed for hematite (**Figure S8**), mainly following the time-dependent mechanism, which is responsible for the formation of 97.88% of the $[Fe(phen)_3]^{2+}$ complex. This may be related to a different and weaker bond between iron and oxygen, due to the presence of another metal (Ni), a different atom with a higher electronegativity in the structure, contributing to an easier and faster dissociation. This easier dissociation may be related to the fact that since Ni has a higher electronegativity, this would concentrate the electronic density around Ni and the bond between oxygen and Fe would become weaker, therefore, facilitating the labilization of the iron-oxygen bond; thus, making the UV-light exposure almost irrelevant. Besides, according to the literature, the coordination of phenanthroline to nickel atoms has an absorption band around 292 nm,[131] and it does not present any band close to 510 nm, therefore, even if some phenanthroline that is present in the solution is being coordinated to Ni, it does not interfere with the iron quantification. Therefore, the method of iron quantification with phenanthroline can also be applied for some iron-based (oxy)hydroxides, even without the need for UV-light exposure.

$CoFeO_x$ (**Figure 14e**) was also studied since it has been extensively studied as a catalyst for both electrochemical and photoelectrochemical water splitting, being able to achieve outstanding results. And the understanding of iron amount can help understand the catalyst activity.[132] The results indicate that $CoFeO_x$ has a predominance of Fe^{2+} on its structure, since by only adding phenanthroline the amount of iron present was 297.2 ± 1.1 nmol, and after the addition of NH_2OH•HCl, the iron amount increased to 364.1 ± 0.5 nmol. After 1h, it is possible to observe an increase in the iron amount, 398.0 ± 3.2 and 400.6 ± 0.5 nmol, for dark and UV-light exposure, respectively. The results indicate that the UV-light effect in the dissociation of iron is almost neglectable, since the small difference in the amount of iron in the dark and with UV-light exposure, around 2.6 nmol, is covered by the standard deviation. The $[Fe(phen)_3]^{2+}$ complex

formation mechanism would be the same as the one proposed for hematite (**Figure S8**), only following the time-dependent mechanism, which is responsible for the total dissociation of iron atoms and formation of the $[Fe(phen)_3]^{2+}$complex. Thus, it is possible to conclude that a mix of metals, sepecially when using metals with higher electronegativity, changes the stability of Fe-O bonds, making the dissociation easier, which makes the use of UV-light unnecessary. Besides, as it was aforementioned and can be seen in **Figure S7**, the cobalt-phenanthroline complex has absorption bands around 200 and 294 nm, and it does not present any band close to 510 nm, therefore, even if some phenanthroline is present in the solution is being coordinated to Co, it does not interfere with the iron quantification. Therefore, the method of iron quantification with phenanthroline can also be applied for some iron-cobalt-based (oxy)hydroxides, presenting great results, even without the need for UV-light exposure.

All obtained results can be found in **Table 4** and the percentage of iron in each analysis is summarized in **Table 5**.

Table 5. Free Fe^{2+} percentage in each condition, assuming the last analysis as 100% of free iron.

	Prussian Blue	**CoFePBA**	**Fe_2O_3**	**NiFe(oxy)OH**	**CoFeOx**
5min – Without $NH_2OH.HCl$	11.79 %	3.24 %	9.19 %	15.57 %	74.20 %
5min – Without $NH_2OH.HCl$	14.81 %	19.29 %	66.29 %	80.93 %	90.88 %
1h – Dark	35.37 %	81.46 %	78.99 %	97.88 %	99.35 %
1h – UV-Light	100.0 %	100.0 %	100.0 %	100.0 %	100.0 %

Table 5 presents a comparison of the percentage of available Fe^{2+} in each of the 4 conditions, assuming the last (1h – UV-Light) provides a total iron dissociation, thus, 100.0 %. As it can be seen, PB and CoFe-PBA have a slower iron dissociation, when compared to iron oxides and hydroxides, and present small values for free Fe^{2+} before 1h. Besides, PB is completely dependent on UV-light exposure for a considerable amount of its dissociation, proving its low solubility. CoFe-PBA also depends on UV-light exposure; however, its structure bands are weaker, and a higher amount of iron is dissociated even without UV light. Iron oxide and (oxy)hydroxide were shown to be more soluble, presenting a higher amount of free iron even before 1h. Although hematite still depends on UV-light exposure for a complete iron dissociation, for NiFeOOH and

$CoFe_x$ the UV-light effect on the dissociation is irrelevant. Hence, even if there are some differences in the catalyst's dissociation behavior, also differences related to the $[Fe(phen)_3]^{2+}$ complex formation for further spectroscopic iron quantification, the method was proven to be suitable for the quantification of iron in different thin films, with great and precise results.

2.4 Conclusion

The method proposed for iron quantification in thin films using 1,10-phenanthroline, preceded by a primary treatment using UV-light to ensure a full dissociation of iron ions was shown to be highly effective, precise, and accurate. The analysis for different iron-based catalysts shows that the method has a wide range of applications in this area, being able to be applied for different structures. Besides, the method stands out as an easy and practical method, that can be performed in a fast way, at a low cost, and providing great results.

2.5 Acknowledgments

All authors are grateful for the financial support of Brazilian Funding Agencies. This study was financed in part by the Coordenação de Aperfeiçoamento de Pessoal de Nível Superior - Brasil (CAPES) - Finance Code 001 and Process (88887.613265/2021-00), Conselho Nacional de Desenvolvimento Científico e Tecnológico CNPq (grant number 303231/2020-3 and 308203/2021-6) and Fundação de Amparo à Pesquisa do Estado de São Paulo, FAPESP (grant#2013/22127-2, 2014/50867-3, grant#2017/23960-0, grant#2017/11986-5, 2017/50085-3, grant#2018/25092-9, 2018/25207-0, 2019/00018-3, 2019/24445-8, 2019/00063-9, grant#2021/05976-2).

Chapter III

Water oxidation performance enhanced by electrochemically designed vacancies on Prussian blue catalyst

The content of Chapter III is an adaptation of the article entitled "Water oxidation performance enhanced by electrochemically designed vacancies on Prussian blue catalyst" by Rafael L. Germscheidt, Danielle S. Francischini, Mariana B. Silva, Marco A. Z. Arruda, André L. B. Formiga, Túlio C. R. da Rocha, Juliano A. Bonacin reprinted with permission from ACS Applied Energy Materials Copyright © 2022, American Chemical Society, **Appendix E**.

Reference: ACS Appl. Energy Mater. 2022, 5, 8, 9447–9454. DOI: 10.1021/acsaem.2c00994.

Graphical Abstract

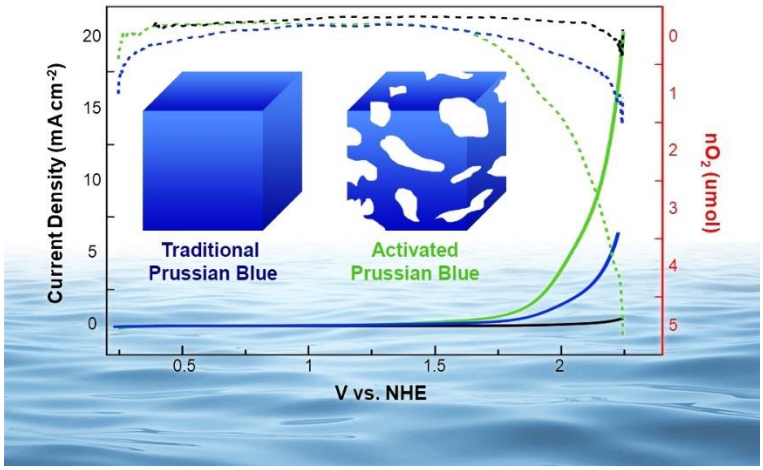

3.1 Introduction

Hydrogen is considered the most promising clean fuel for the future, however, its cleanness is directly related to the production pathway.[1,133] Therefore, water splitting (WS) has been gaining attention in the past years, since it is the process of producing H_2 directly from water, via 2 half-reactions, known as the oxygen evolution reaction (OER) or water oxidation reaction (WOR) and the hydrogen evolution reaction (HER).[69,125] Although the overall process may seem simple, the WOR presents itself as the bottleneck reaction and requires a catalyst to be efficient.[90]

Different classes of catalysts for WOR have been studied in the past years, however, noble metal catalysts are not viable in the long term. Thus, the challenge for scientists is to develop catalysts based on Earth-abundant elements and with simple and inexpensive preparation. Among them, metal hexacyanoferrates, in which Prussian blue analogues (PBA) are one of the most promising examples, stand out due to their great performance, activity, and stability under mild conditions.[69,80,83,125,134] Despite their high stability and activity, the main shortcoming is their low concentration of active sites. Due to this, engineering the structure and defects is essential to lead to a high concentration of active sites, and consequently a higher catalytic activity.[69,84–86]

Increasing the catalytic activity of a catalyst is the major challenge for scientists in many areas. In this sense, the modulation of defects in the catalysts can have direct impacts on their properties, like band structure tunning, conductivity, magnetism, and mainly in the performance. The most common known defect is the vacancy, which can lead to substantial structural perturbations in the catalysts, creating changes in the electronegativity, charge concentration, and redistribution, thus enhancing the catalyst activity.[87] A few researchers reported the generation of unusual cyanide vacancies in different PBAs using different methodologies, which exhibit low overpotentials and high current densities for WOR in alkaline medium, exceeding the ones previously cited for the original Prussian blue analogues.[85,86,88]

Despite advances in research concerning PBA, a full understanding of the mechanism and surface reactions remains a challenge and *in situ* techniques can be crucial for these studies. In this context, scanning electrochemical microscopy (SECM), an *in situ* electrochemical tool can be used to probe surface reactions, reaction intermediates and it works for both quantitative and qualitative analysis.[135] In SECM, an ultramicro-electrode (UME) works as a probe, positioned in the vicinity of the sample surface based on the recorded current response, and the measurements can be

performed using different operational modes.[136] SECM operating on generation-tip collection (SG/TC) mode has been used to study OER for heterogeneous catalysts, being able to identify spots with a higher production of oxygen (concentration of active sites), giving information about when the O_2 evolution actually starts (onset potential) and also comparing O_2 evolution reaction rates among different catalysts.[137–139] During these measurements, oxygen is evolved by the substrate, where the catalyst is supported and diffuses onto the tip biased at the potential to reduce oxygen. Therefore, the higher the tip current response, the more oxygen is being evolved.[139]

Here we report a novel methodology to synthesize the Prussian blue and promote the improvement of its properties on water oxidation by electrochemically formed vacancies. The outstanding performance of Prussian blue with defects in the water oxidation reaction was followed by SECM studies and the oxygen evolution was measured during the process. Furthermore, we also proposed an alternative strategy to study and quantify the number of active sites in this type of catalyst.

3.2 Experimental Section

3.2.1 Catalyst preparation and GCE modification

Before the modification, the GCE was carefully polished successively with 1, 0.5 and 0.3 μm alumina to remove the electrode contamination and to make its surface smooth, then it was sonicated in isopropanol for 15 minutes to remove the alumina particles and finally, rinsed with Milli-Q water. Then, the GCE was used on the electrodeposition step as the working electrode, saturated calomel electrode as a reference electrode and a platinum wire as an auxiliary electrode. The potential values are reported in a function of the NHE reference electrode (Normal Hydrogen Electrode). To calculate this potential, the following equation was used.

$$E \text{ vs. NHE} = E \textit{ vs. } \text{SCE} + 0.224 \text{ V}$$

3.2.1.1 Traditional Prussian Blue

The TPB film was deposited over the FTO electrode according to the method well stablished and optimized in the literature.[140] For this, the electrode was immersed in a solution containing 1 mmol L^{-1} of $[Fe(CN)_6]^{-3}$, 1mmol L^{-1} of $FeCl_3$, 0.1 mol L^{-1} of KNO_3 and 0.1 mol L^{-1} of

HCl. Then 8 cycles were performed from 0.594 to 1.024 V, on a scan rate of 8 mV s^{-1}. After this, a blue film was observed on the electrode. The electrode was dried before further tests.

3.2.1.2 Activated Prussian Blue

The electrode was immersed in a solution containing 1 mmol L^{-1} of $[Fe(CN)_6]^{4-}$, then a potential of 2.224 V was applied to the WE for 60 seconds. After this, a blue film was observed on the electrode. The electrode was dried before further tests. The material activation parameters such as the best solution concentration, best voltage and best electrochemical reaction time were previously optimized in order to obtain the best film composition and growth.

3.2.2 Electrochemical characterization

Cyclic voltammetry was used to obtain information on the presence and the characteristics of the film on the substrate. In these experiments, the electrolytic solution used was 0.5 mol L^{-1} potassium nitrate, KNO_3 (Aldrich).

Linear sweep voltammetry was used to study the activity of the film during the Water oxidation reaction. In these experiments, the electrolytic solution used is the same used during the CV experiments.

EIS experiments were performed using a 0.5 mol L^{-1} solution of KNO_3 as a supporting electrolyte. Since WOR is only controlled by kinetics, such as charge transfer rates, to have a real comparison between the catalysts during the catalysis, EIS measurements were acquired at constant potentials in the catalytic turnover region (2.024 V vs. NHE) with a frequengy ranging from 1 x 10^5 to 0.1 Hz. In this way, electrochemical circuit for the surface under study can be regarded in analogous to the simple Randle's cell (Figure 2c - inset), indicating the occurrence of a charge-transfer controlled reaction.[141]

3.2.3 3D Printed SECM assembling and calibration

3.2.3.1 3D printed SECM design

The SECM cell and positioner had their design adapted from previous reports on literature[142–144] using TinkerCAD™, a free online 3D CAD design tool, as it can be seen in **Figure 17**. Standard tessellation language (STL) file was obtained and then the model was sliced on

Simplify3D software to generate the G-Code language, which instructs movements of 3D-printer (RepRap Graber i3). The SECM was printed with ABS filament and the printing parameters were set to a resolution of 0.2 mm per layer, nozzle temperature of 230 ºC and bed temperature of 100 ºC. After the printing processes, all the parts were easily assembled. The electrochemical cell allows the assembling of a 4 electrodes arrangement, due to the necessity of the use of 2 working electrodes (WE1 – Modified with the catalyst/WE2 – Platinum tip microelectrode). As an electrode (GCE) was used on the bottom of the cell, a rubber O-ring was used to fix the working electrode in the center of the cell and to prevent any leakage that could compromise the measurements.

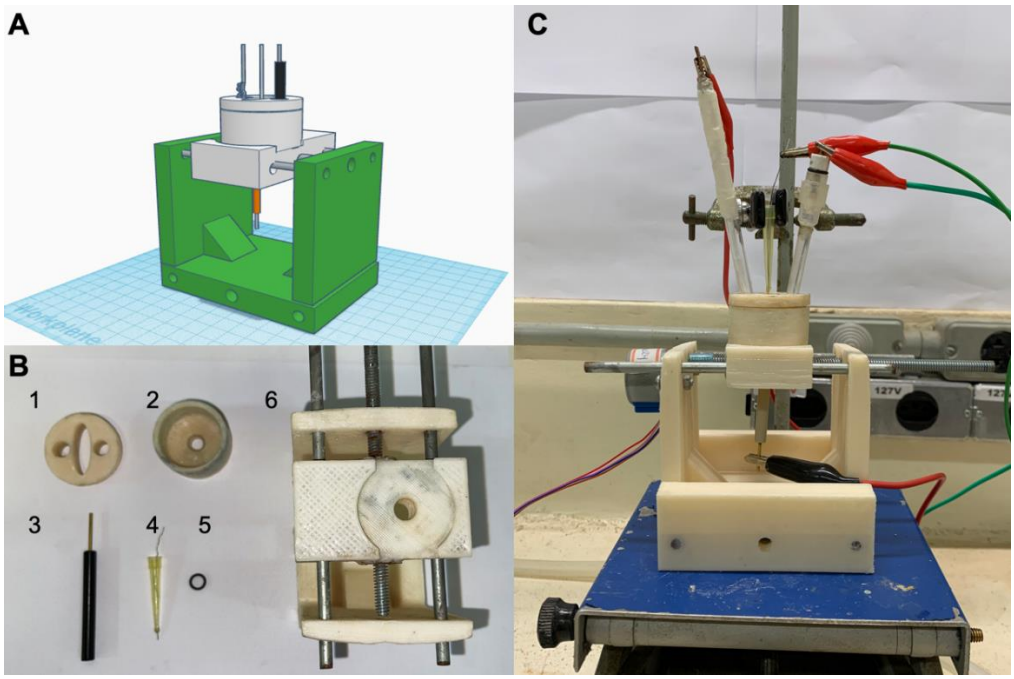

Figure 17. 3D Printed Scanning Electrochemical Microscope (SECM) scheme. A) 3D design made on ThinkerCat for printing details. B) 3D printed parts to assemble the 3D-Printed SECM. 1- Electrodes' support, 2- Electrochemical cell, 3- Glassy Carbon electrode, 4- Platinum tip electrode, 5- O-ring to facilitate the assembling, 6- SECM structure to hold the electrochemical cell. C) Assembled and working 3D Printed SECM.

3.2.3.2 Oxygen Evolution Studies

The water oxidation studies were performed on the 3D printed SECM cell, operating at the substrate generation – tip collection mode (SG/TC), using a 4 electrodes arrangement. Using this mode, O_2 is generated on the WE1 surface, during the WOR, furthermore it diffuses towards the WE2, biased at the potential required to reduce O_2, and the measured current can be related to the

O_2 evolution, see **Figure 18**. The modified GCE was used as the WE1, saturated calomel electrode as a reference electrode, a platinum wire as an auxiliary electrode, and a micro sized platinum wire as the WE2. Using Linear Sweep Voltammetry (LSV), performed on the WE1, from 0 to 2.224 V, the WOR activity was evaluated. At the same time, a constant potential of -0.31 V was applied to the WE2, while the current was monitored to identify the moment where O_2 would start being evolved (changes on the reduction current), see **Figure 18**. By comparing both plots, it was possible to determinate the real onset potential for the OER also having a better approach to identify the best section to obtain the Tafel plots.

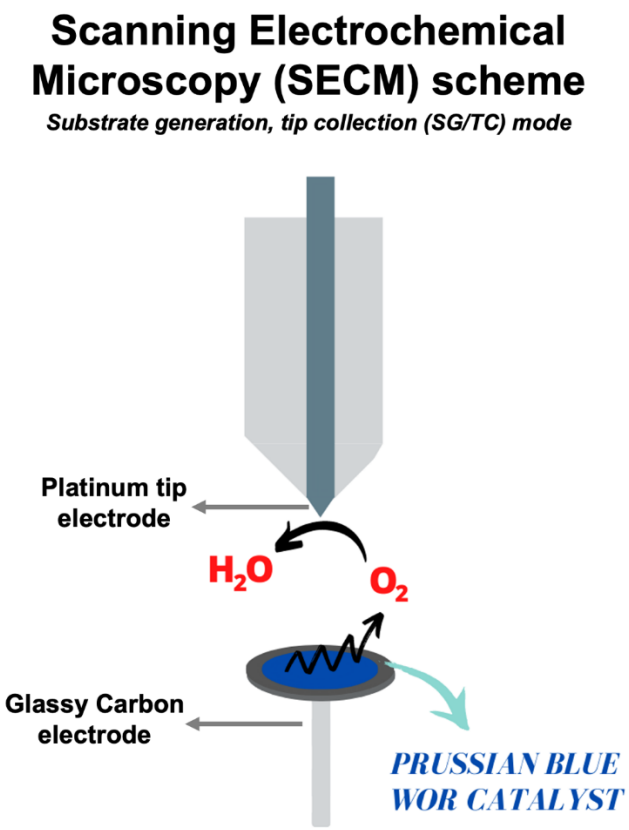

Figure 18. Scheme for Scanning Electrochemical Microscopy operating in the Substrate Generate/Tip Collection mode, used to identify and sense O_2 production during WOR with Prussian Blue catalysts.

3.2.3.3 Oxygen Evolution Studies

The produced oxygen was measured by platinum microelectrode. The obtained reduction current was previous related to the amount of dissolved oxygen, calibrating the PME with a dissolved oxygen (DO) sensor, Hanna instrument.

For the calibration, an electrolyte solution (KNO_3) was purged with air to get it saturate with O_2. Then, the dissolved oxygen was measured and straight up the reduction current was measured (by applying -0.31 V for 60 s). The solution was then purged with N_2 for 20 minutes, however the current and the dissolved oxygen concentration were measured every 2 minutes, to obtain a calibration curve. The calibration was obtained 3 times, to have a more conclusive value (**Figure 19**).

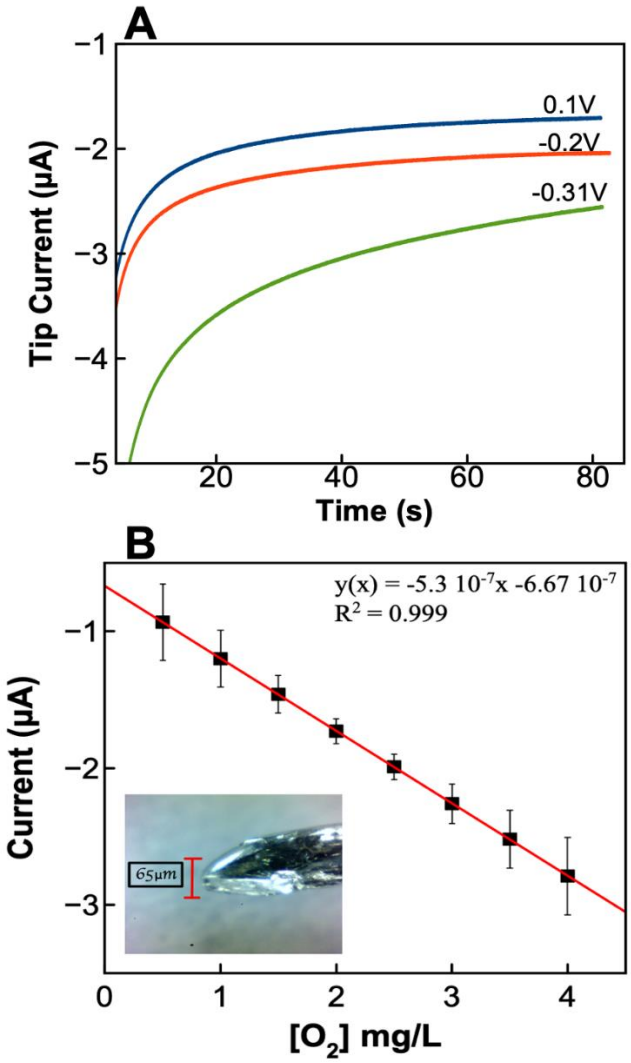

Figure 19. Platinum tip electrode calibration. A) Study for the best reduction potential for the identification and reduction of O_2. B) Tip electrode calibration for different concentration of O_2 in an KNO_3 solution. The calibration was made using HANNA electrode. Inset represents a microscopic image of the tip's surface end.

3.2.3.4 TOF Calculation

To calculate TOF numbers, a constant potential was applied to the WE1 (different overpotentials), and the reduction current was monitored on the WE2, and the resulted value was transformed into nO_2 evolved by using the calibration curve line equation. These values were used to calculate TOF according to the equation previously reported.

Using the O_2 reduction current obtained from the calibrates tip electrode, the turnover number (TON) and turnover frequency (TOF) were calculated by the following equations:

$$\text{TON} = \frac{mols\ \text{oxygen}}{mols\ catalyst}$$

$$\text{TOF} = \frac{TON}{time\ (s)}$$

To obtain the number of mols of catalyst that were deposited on the electrode surface, after the electrochemical deposition, the GCE was lixiviated with an alkaline solution to remove the catalyst from its surface, and then the total amount of iron was quantified by a spectrophotometric method, according to **Figure 20**.

The total iron in Prussian blue films was quantified through the spectroscopic method with 1,10-phenanthroline. The use of phen to quantify Fe^{2+} ions is a well-known method since this bidentate chelating agent has two nitrogen atoms at the ortho positions of the rigid half-ring structure, which can coordinate with Fe^{2+} ions, forming a complex.[102] This complex can easily be quantified by spectrochemical analysis, since the absorption band on the UV-Vis electronic spectrum of $[Fe(phen)_3]^{2+}$, assigned to the MTCL Fe(*d*) → phen (π*) transitions, has an intensity directly proportional to the $[Fe(phen)_3]^{2+}$ complex concentration in the solution.[120] This quantification was preceded by a film dissolution on NaOH and a UV-light treatment. The photochemical approach was used to ensure a full dissociation of iron ions (cyanide labilization), providing the necessary energy for the complex dissociation to happen and consequently the complexation with phenanthroline present in the solution. An excess of a reducing agent (hydroxylammonium chloride - $NH_2OH{\bullet}HCl$) was also added to the solution to make sure that all free iron was converted into Fe^{2+}.

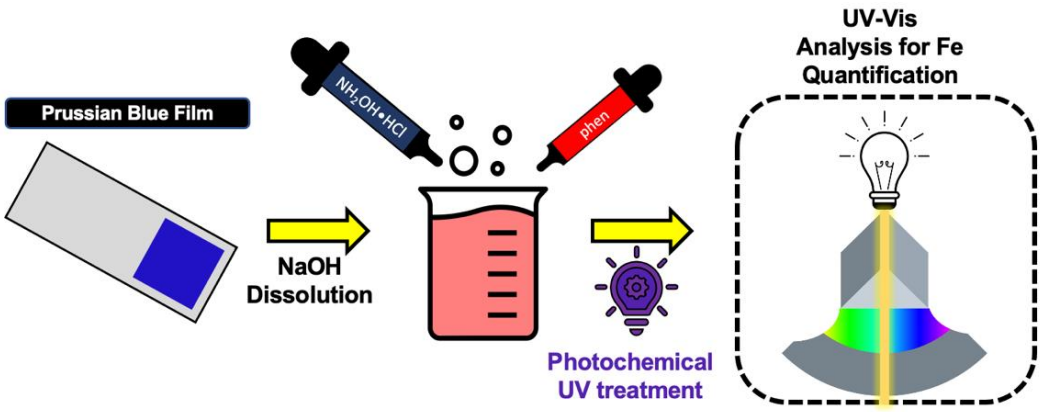

Figure 20. Iron spectrochemical quantification for Prussian Blue films using 1,10 – phenanthroline, carried out by a previous photochemical treatment with UV-light to labialize the cyanide and free Fe atoms to be coordinated with phen.

3.2.4 Electrochemical Active Surface Area (ECSA) and Heterogeneous electron transfer rate constant (K^o_{obs})

The electroactive areas were evaluated by CV measurements performed at different scan rates from 2.0 to 12 mV s^{-1}, according to the Randles–Ševčíck equation (3)[145], where Ip is the peak current, A is the electrode area, C is the concentration of the redox probe, D is the diffusion coefficient, n is the number of electrons transferred. The redox probe used was Hexaamminerutheniumm(III) chloride - $[Ru(NH_3)_6]Cl_3$. The results can be seen on **Figure 21** and Table 1, and ECSA was used to calculate current density (j).

$$I_p = 2.69\ x\ 10^5 ADC^{\frac{1}{2}} n^{\frac{3}{2}} v^{\frac{1}{2}}$$

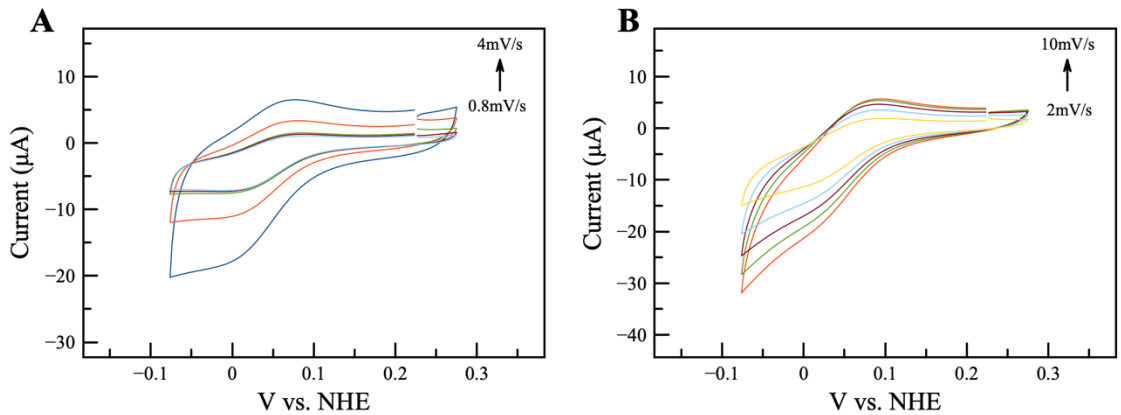

Figure 21. Cyclic voltammetry performed using $[Ru(NH_3)_6]Cl_3$ probe in different scan rates. A) Traditional Prussian Blue. B) Activated Prussian Blue.

The heterogeneous electron transfer rate constant (k°_{obs}) was determined by the Nicholson method[146] and calculated using equation bellow, where D is the diffusion coefficient (9.10×10^{-6} $cm^2\ s^{-1}$ for $[Ru(NH_3)_6]^{3+}$), α is assumed to correspond to 0.5, n is the number of electrons transferred in the electrochemical process, F is the Faraday constant, ν is the scan rate, R is the gas constant, T is the temperature and ΔE_p is the peak-to-peak separation.

$$\mathbf{k}^{\circ}_{obs} = \left[2.18\left(\frac{D\alpha nF\nu}{RT}\right)^{\frac{1}{2}}\right] exp\left[-\left(\frac{\alpha^2 nF}{RT}\right)\Delta E_p\right]$$

3.2.5 FTIR Spectroscopy

Infrared spectra of the samples were obtained using an Agilent Cary 660 FTIR spectrometer in the ATR mode with a diamond crystal in the range of 400 to 4000 cm^{-1}, resolution of 4 cm^{-1}.

3.2.6 RAMAN Spectroscopy

Raman analyses were performed using a Confocal T64000 spectrometer (Jobin Yvon, USA) using a 532 nm laser, resolution of 2.9 cm^{-1}, with a 100x LWD objective. The distance between the laser and the sample was adjusted with respect to the laser focus, using the camera coupled to the equipment. Spectrum was acquired in 60s, in the range of 100-690 cm^{-1}, with 5 accumulations, and

in 30s, in the range of 2000-2200 cm^{-1}, with 5 accumulations. All Raman spectra were recorded after instrument calibration on the internal standard silicon wafer (~ 520.7 cm^{-1}).

3.2.7 UV-Vis Spectroscopy

Spectra of FTO modified electrodes in the UV–Visible region were obtained using a HP8453 UV–visible absorption spectrophotometer, using a 3D printed cuvette that allowed the measurements to be done directly on the FTO electrode, 0,5x2 cm. The 3D cuvette was designed on TinkerCAD™ and then 3D printed following the same methods described for the SECM cell.

For pyridine quantification, spectra of aqueous solutions in the UV–Visible region were obtained using a Bel Photonics UV-M51 UV–visible absorption spectrophotometer, with a 1 cm quartz cuvette, in the region from 200 to 450nm.

3.2.8 SEM

The morphologies of the samples were examined with a Quanta 250 field emission scanning electron microscope (FEI Co., USA), equipped with an Oxford X-MAX50 energy dispersive spectrometer (EDS) (Oxford, UK). The samples were mounted in a conductive carbon tape followed by carbon sputtered coating in a Bal-Tec MD020 instrument (Balzers).

3.2.9 AFM

The topography and surface potential of the samples were further analysed with Atomic Force Microscopy (AFM) and Kelvin Probe Force Microscopy (KPFM). The AFM and KPFM images were obtained simultaneously using a Flex AFM C3000 (Nanosurf, Switzerland), operating under dry atmosphere and with a Pt/Ir coated tip (EFM-10, Pointprobe®), resonance frequency of 75 kHz and a force constant of 2.8 N m^{-1}.

3.2.10 XPS and XAS

XPS and XAS measurements were performed at the IPE beamline of Sirius at the Brazilian Synchrotron Light Laboratory using the photoemission endstation at the A branch. XPS was measured using a PHOIBOS 150 analyser from SPECS. Total electron yield XAS was obtained by measuring the drain current using a Stanford electrometer. Samples were freshly prepared and transferred to the vacuum chamber within few hours to minimize accumulation of carbon

contaminants at the surface. XPS spectra were measured using a photon energy of 1200 eV using a pass energy of 20 eV. No considerable charging was observed, and kinetic energies are reported as measured. Before collecting a complete set of spectra for each element, several survey scans were measured at different spots of the sample to evaluate sample homogeneity and eventual beam damage. Quantitative XPS analysis were performed by using the area of the of the most intense peaks of each element after Shirley background removal correction by photoionization cross section, inelastic mean free path, and ring current. For the XAS spectra a linear background was subtracted from the data and the intensities were normalized to 1 after the edge jump around 740 eV.

3.2.11 Laser Ablation Inductively Coupled Plasma Mass Spectrometry (LA-ICP-MS)

Laser ablation inductively coupled plasma mass spectrometry (LA-ICP-MS) is one of the important techniques applied to elemental imaging because not only provides high spatial distribution (5 – 110 µm) and sensitivity from the ICP-MS, but also requires minimum sample preparation steps,[147] which contributed to the applications in medical[148] and environmental assessments,[101,149] as an example. This hyphenated technique consists of a high-power laser beam focused on the sample surface by x,y,z coordinates, and its interaction with the sample promotes the evaporation of a small portion of such sample in the incident region and a dry aerosol is then formed. The aerosol is transported towards the ICP-MS, in which a plasma with high energy promotes the atomization and ionization process of the chemical elements, and the ions are analyzed by the mass to charge ratio (m/z) through a mass detector, and the signal intensity is detected. The final elemental image is created by correlating the signal intensity for each ion with the laser coordinates (x,y) by adequate software.[147,150]

3.2.11.1 Instrumentation and Measurements of LA-ICP-MS

The qualitative elemental spatial distribution of Fe and C was evaluated using a New Wave UP-213 laser ablation system (LA) with an Nd:YAG (at 213 nm) laser source and a quadrupole-based inductively coupled plasma mass spectrometer (ICP-MS, PerkinElmer ELAN DRC-e). The

LA-ICP-MS analysis measurements were performed in a 10,000-class clean room and the operations conditions from ICP-M were optimized daily with an Mg, In, Be, Ce, and U solution to check the production of mono charge ion, oxide, and double charge species, which their presence was always lower than the tolerable limit of 3%. The LA-ICP-MS parameters were optimized for glass sample analysis using NIST 612 certified reference material (Trace element in glass) and the instrumental conditions used are summarized in **Table 2**.

Table 2. Optimized instrumental operational conditions and measurement by LA-ICP-MS.

Instrumental settings	
RF Power (W)	1300
Nebulizer gas flow (L min^{-1})	1.2
Auxiliary gas flow (L min^{-1})	1.6
Data acquisition parameters	
Reading mode	Peak hopping
Detector mode	Dual
Sweeps	3
Dwell time (ms)	20
Integration time (ms)	60
Monitored isotopes	^{13}C, ^{57}Fe
Laser conditions	
Wavelength of Nd:YAG laser (nm)	213
Laser ablation intensity (%)	90
Frequency (Hz)	20
Spot size (μm)	100
Scan speed (μm s^{-1})	60
Average energy output (mJ)	1.80
Average fluence (J cm^{-2})	25.6
Warm up time (s)	7
Wash out time (s)	10

Laser ablation acquisition was conducted in line scan mode, with parallel lines of 0.24 mm from the distance between each laser line, producing a scan reading of the sample surface with 30 ablation lines in the TPB surface and 34 ablation lines in the APB surface. The ablated material was transported to the ICP using argon as the carrier and nebulizer gas. After each ablation line,

the chamber was purged during 10 s with argon for cleanup. The final images were built using the freely available LA-iMageS software at http://www.la-images.net/.[151]

3.3 Results and Discussion

3.3.1 Synthesis and Characterization

Traditional Prussian blue (TPB) and activated Prussian blue (APB) were electrodeposited on a Glassy Carbon Electrode (GCE) according to the procedures described in the Experimental Data section in the Supporting Information. Experimental descriptions and details of the equipment are also included in the Supporting Information section.

Traditional Prussian blue film was electrochemically deposited over the electrode through the classic voltammetric method using Fe^{3+} ions and $[Fe(CN)_6]^{3-}$ complex.[140,152] The curves of the electrodeposition process are presented in **Figure 22 A**, the image of the produced film can be seen in **Figure 22 B**. Although the classical process to produce Prussian blue films is well-known, amperometric methods bring additional new prospects and challenges, thus, the strategy consists in applying a high and constant potential to the electrode in a solution containing $[Fe(CN)_6]^{4-}$ that is oxidized along with some cyanide groups. We named this material activated Prussian blue (APB). **Figure 1C** shows the evolution of the measured current as the activated Prussian blue film is deposited over the electrode surface (**Figure 22 D**). This classic process has different proposals about what could can take place during the film growth, nonetheless, it is more likely that the film is formed during the cathodic scan, when Fe^{3+} is reduced to Fe^{2+} (step 1) and coordinates with $[Fe(CN)_6]^{3-}$ (step 2). It is important to highlight that step 1 is potential dependent, while step 2 will only depend on the species diffusion onto the electrode.

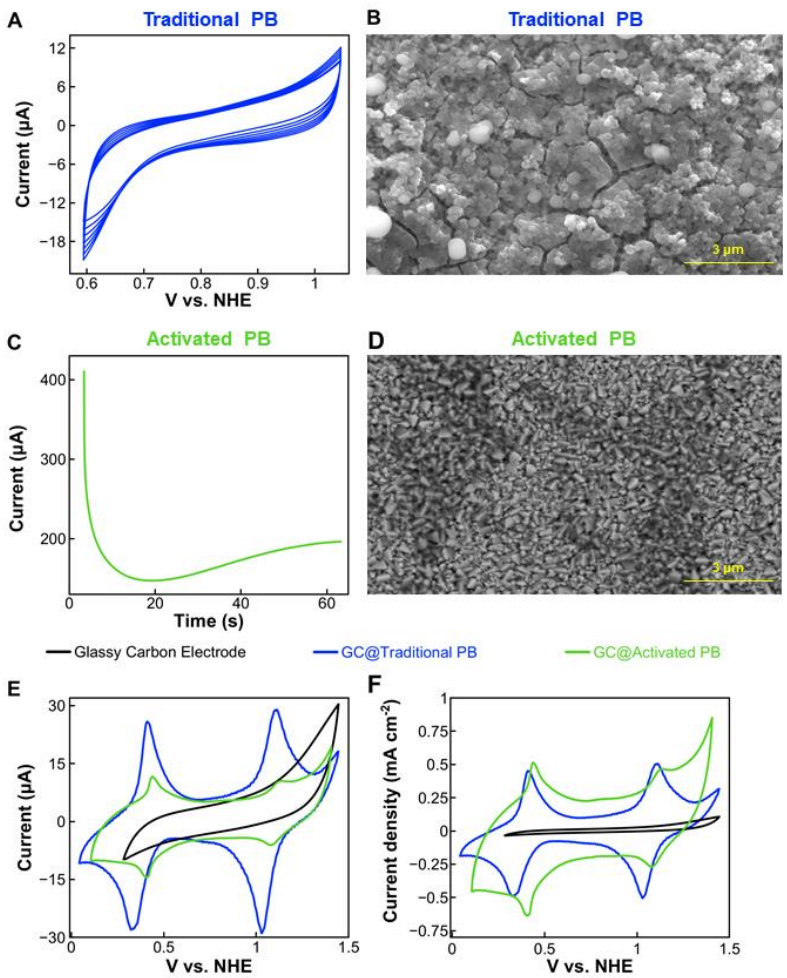

Figure 22. Electrochemical data for traditional Prussian blue (blue line), activated Prussian blue (green line) and bare glassy carbon electrode (black line). A) Cyclic voltammetry performed for traditional Prussian blue synthesis. B) Scanning Electron Microscopy (SEM) image obtained from Traditional Prussian Blue film. C) Amperometric methods performed for activated Prussian blue synthesis. D) Scanning Electron Microscopy (SEM) image obtained from Activated Prussian Blue film. E) Cyclic voltammetry performed at 50 mV s^{-1} in 0.5 M KNO_3 solution for Glass Carbon electrode modified with the catalysts. F) Cyclic voltammetry normalized by the current density calculated from ECSA.

Both films were characterized by cyclic voltammetry, as shown in **Figure 22 E** and **F**. TPB and APB show an iron redox process assigned to the oxidation/reduction of Prussian White to Prussian Blue ($Fe^{2+}/Fe^{2+} \rightarrow Fe^{3+}/Fe^{2+}$) under potential below 0.5 V, and a second process assigned to the oxidation/reduction of Prussian Blue to Berlin Green ($Fe^{3+}/Fe^{2+} \rightarrow Fe^{3+}/Fe^{3+}$), under potential beyond 1.0 V. The electrochemical data obtained from the cyclic voltammogram are presented in **Table 6**. In addition, the heterogeneous electron transfer rate constant[153] (k^0_{obs}) is 1.0 x 10^{-3} cm s^{-1} for TPB and 2.2 x 10^{-3} cm s^{-1} for APB, which reinforces the idea of different electronic structures.

Table 6. Electrochemical parameters of the first and second electrochemical process of TPB and APB.

	E_{a1} (V)	E_{c1} (V)	ΔE_1 (mV)	E_{a2}(V)	E_{c2}(V)	ΔE_2 (mV)	$k^0_{obs} \times 10^{-3}$ (cm s^{-1})
TPB	0.40	0.33	70	1.10	1.03	70	1.0
APB	0.45	0.41	40	1.13	1.08	50	2.2

E_{a1}: anodic peak potential for the 1st process; **E_{c1}**: cathodic peak potential for the 1st process; **E_{a2}**: anodic peak potential for the 2nd process; **E_{a2}**: cathodic peak potential for the 2nd process; **1st process:** (Fe^{2+}-N-C-Fe^{2+} → Fe^{3+}-N-C-Fe^{2+}); **2nd process**: (Fe^{3+}-N-C-Fe^{2+} → Fe^{3+}-N-C-Fe^{3+})[154,155]

Both electrochemical processes of APB take place in slightly higher potentials than TPB, suggesting iron species with different chemical environments.[152,156,157] This potential shift to high values indicates that although APB presents a cyclic voltammogram similar to TPB, it has a different structure.

3.3.1.1 X-ray Diffraction (XRD)

XRD analysis were carried out and can be seen in **Figure 23**. In both diffractograms, TPB and APB, it is possible to identify the diffraction peaks related to the Prussian Blue structure, at 2θ = 17.5°, 24.7° and 54.2° correspond to the hkl planes (200), (220) and (600) and (620), respectively (according to the JCPDS card No 01-0239). Only on TPB it was possible to identify the diffraction peak at 2θ = 35.4° corresponding to the hkl plane (400). However, those peaks in both materials have different intensities, having a lower intensity for APB, indicating a few differences in the PB structure with material electrochemical activation and possible vacancies creation. Nonetheless, the presence of those peaks on APB indicates that characteristics of PB structure were kept by the activated material. Besides, they both have the diffraction peaks for FTO (substrate).[158] It is also possible to find peaks for the reactants, such as $K_3[Fe(CN)_6]$ (Δ), $K_4[Fe(CN)_6]$ (#) and KNO_3 (*), that were present in the solution during the film formation.

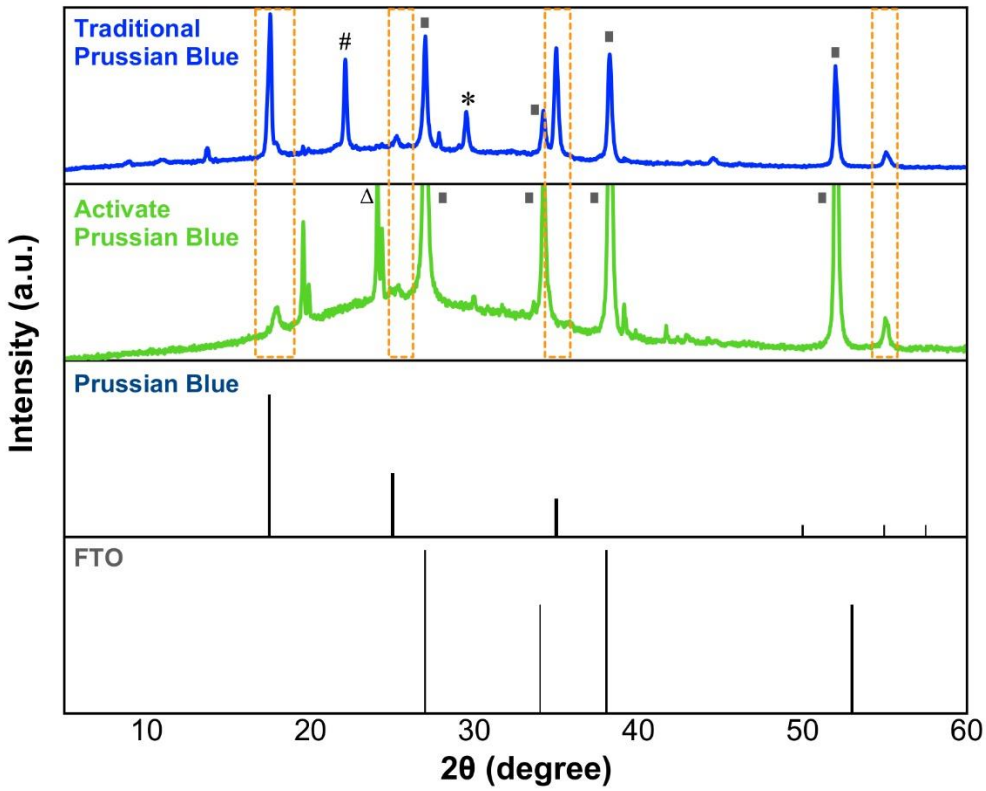

Figure 23. Comparison of X-Rays diffraction patterns of Traditional Prussian blue, Activated Prussian blue, Prussian blue (obtained from literature data base, JCPDS card No 01-0239) and FTO (obtained from literature data base).[158] In both catalyst's diffraction patterns it is possible to identify peaks related to Prussian Blue (highlighted in orange), FTO (□), $K_3[Fe(CN)_6]$ (Δ), $K_4[Fe(CN)_6]$ (#) and KNO_3 (*)

3.3.1.2 Vibrational Spectroscopy

Aiming to have a better understanding about the catalysts structure, Raman analysis were also carried out on FTO modified electrodes and the results can be seen on **Figure 24**. For both films, it is possible to identify 2 main bands around 2158 and 2094 cm^{-1}, which can be assigned to the A_{1g} and E_g mode of ν(CN) stretching vibration, respectively. These are the bands that are characteristic of Prussian blue analogues structures.[155,159] On the TPB spectra, it is possible to identify a third band, around 2025 cm^{-1}, which can be assigned to the stretching vibration of $[Fe(CN)_6]^{3-}$, a band that is characteristic of Berlin Green, where there is a predominance of Fe^{3+} ions, due to the oxidation process. The presence of this band in the TPB is also in the agreement with the UV-Vis analysis, showing a higher concentration of Fe^{3+} in the TPB and of Fe^{2+} on APB. However, the results show that the different route of synthesis and the PB "activation" did not

change the main Prussian blue structure. The spectra for the catalysts after the catalysis (dashed lines) indicate no change in the structure, maintaining the bands characteristic to the PB, the ν(CN) stretching vibration, indicating no oxide was formed on the structure. For TPB it is also possible to observe an increase in the intensity of the band around 2025 cm^{-1}, indicating an increase on Fe^{3+} in the structure, since the material has been submitted to higher potentials, and it not all ions are capable to reduce and return to their initial state. Even after catalysis, it not possible to observe this band in the APB spectra, indicating, once again, the predominance of Fe^{2+} and, the material's ability to return to the initial oxidation state.

As an attempt to prove no FeOOH by-product is formed during the TPB activation, vibrational Raman spectroscopy was carried out on the films. As it can be seen in the spectrum (**Figure 25 A**) and the assignment bands table (**Table S1**), no band related to FeOOH is found in the Prussian Blue either before or after the activation process. It can only be identified the bands related to metal (Fe)-CN vibrations. The bands around 1575 and 1880 cm^{-1} that are common to most of the films are related to a glass (FTO-substrate) photoluminescence caused by the excitation using the laser 785 nm during the measurements.[160] Besides, cyclic voltammetry comparing the films (**Figure 25 B**) show a different characteristic for FeOOH when compared to APB and TPB, thus, no FeOOH by-product is formed after the activation.

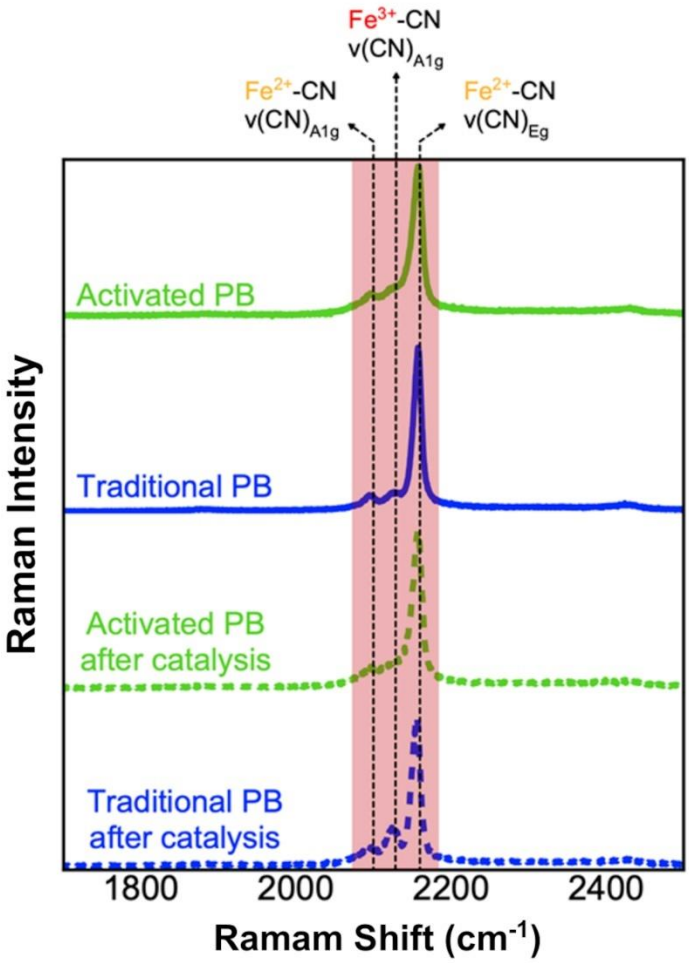

Figure 24. Raman spectra obtained from the materials before and after the catalysis.

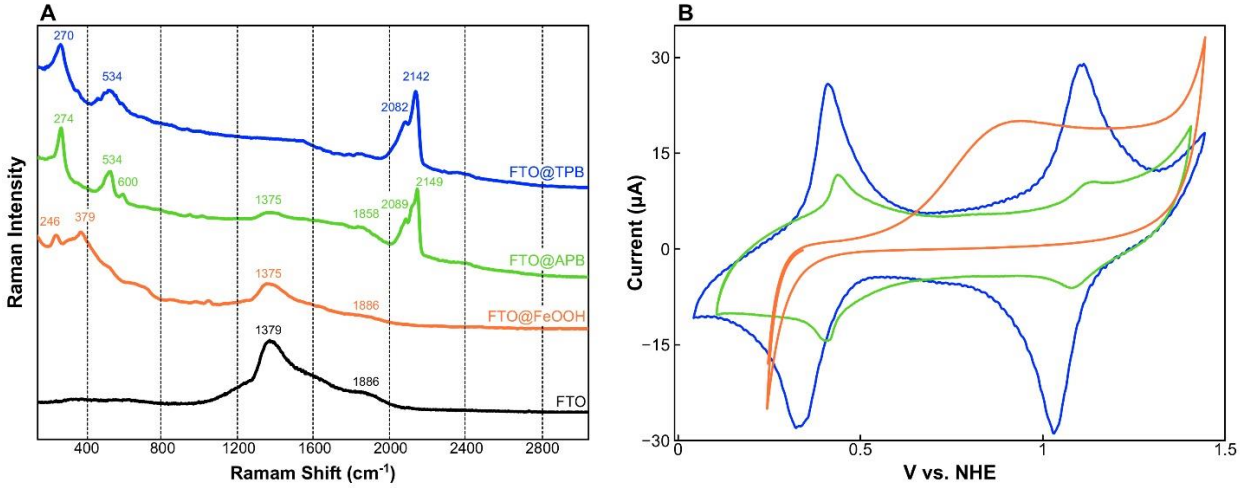

Figure 25. Films comparison with FeOOH. A) Raman spectra obtained using a 785 nm laser excitation for the modified FTO electrodes. B) Cyclic voltammetry performed in 0.5 M KNO3 in the modified FTO electrodes.

Table 7. Raman bands assignment.[159–161]

	B_{1g} FeOOH	Fe-CN-Fe	A_g FeOOH	Fe^{3+} F_{1u} δ(MC)	Fe^{2+} F_{1u} δ(MC)	Substrate (glass)	Substrate (glass)	E_g ν(CN)	A_{1g} ν(CN)
FTO@TPB	-	270	-	534	-	-	-	2082	2142
FTO@APB	-	274	-	534	600	1375	1858	2089	2149
FTO@FeOOH	246	-	379	-	-	1375	1886	-	-
FTO	-	-	-	-	-	1379	1886	-	-

Vibrational spectra (FTIR) of FTO electrodes modified with both catalysts before and after the catalysis was performed and can be seen on **Figure 26**. For both catalysts, before the catalysis, it is possible to identify the vibrational band around 2062 and 2064 cm^{-1} for APB and TPB, respectively. Those peaks are characteristic of C≡N stretching vibration, which is considered as the fingerprint for cyanide-based coordination compounds, thus, very common for Prussian Blue analogues.[83,86,162] This indicates that, the Prussian blue analogue structure remains, regardless the differences in the synthesis and the presence of vacancies. Another important band that appears in the analysis is the broad band at around 3415 cm^{-1}, which is related to the O-H stretching mode of the water molecule.[86] Since this band only appears for the APB, this supports our idea that CN^- vacancies were created and water molecules start to occupy these vacancies, facilitating the intermediate access to the active sites, making the APB a better catalyst towards the WOR. It is also possible to observe that after the catalysis, the bands shifted towards higher wavenumbers, 2074 and 2070 cm^{-1}, for APB and TPB, respectively. This shift is related to an increase on the metal oxidation state,[83] indicating that the potential application causes it to increase, in order to interact with the WOR intermediates, and some of them do not return to its initial state. This can give us insights about the reaction mechanism, showing that the metal center actively participates on the electron transfer process that takes place during the WOR oxidation.

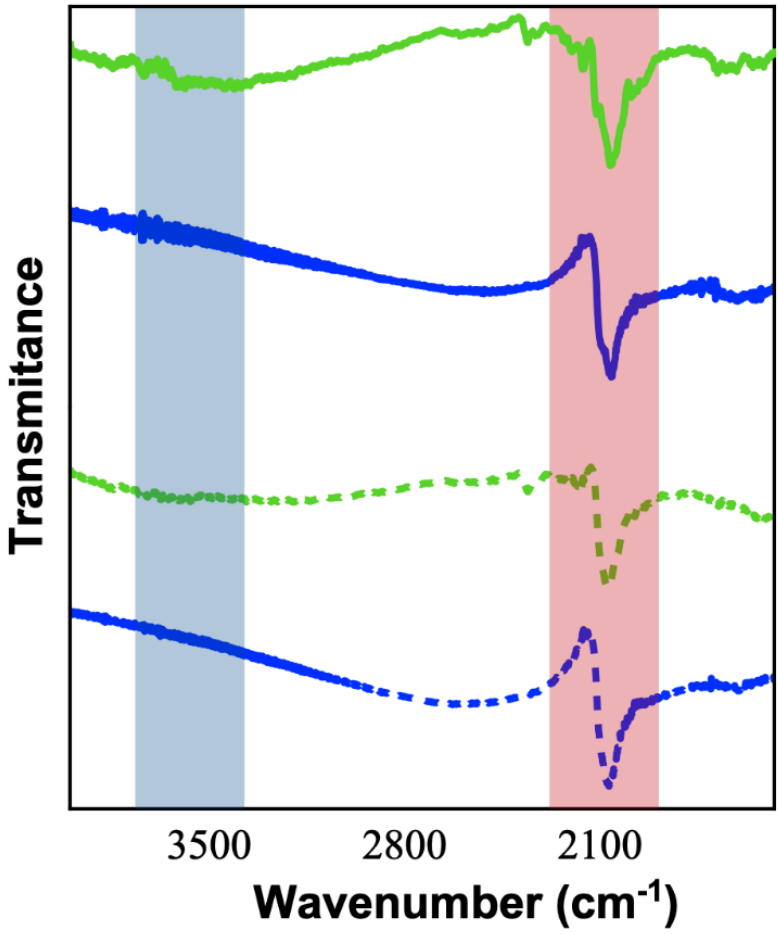

Figure 26. Vibrational spectroscopy characterization of the Catalysts (FTIR). Activated Prussian Blue Before Catalysis (Green straight line), Traditional Prussian Blue Before catalysts (blue straight line), Activated Prussian Blue After Catalysis (Green dashed line) and Traditional Prussian Blue After Catalysis (blue dashed line).

3.3.2 Catalytic activity study

TPB and APB films had their catalytic activity evaluated towards WOR. Hence, a scanning electrochemical microscopy cell was manufactured in a 3D printer (**Figure 17**). The operating principle of this device is detailed in **Figure S6**. The arrangement with two working electrodes allows the evaluation of the catalyst current densities, along with an evaluation of the amount of O_2 being evolved, according to the SECM substrate generation/tip collection (SG/TC) operation mode (**Figure 18**). The obtained results can be observed in **Figure 27** and **Table 8**. The oxygen evolution for APB starts first, exhibiting a lower onset overpotential, 361 mV, while the traditional Prussian blue presented an onset overpotential of 471 mV (**Figure 27 A**). Furthermore, the current

density for APB at 995 mV (the highest applied overpotential) is more than 2 times higher than the one obtained by TPB at the same potential. The overpotential to reach j = 1 mA cm^{-2} is 711 and 599 mV for TPB and APB, respectively, with a difference of 112 mV between the materials, showing the activation process for the APB catalyst had a direct impact on its activity towards WOR.

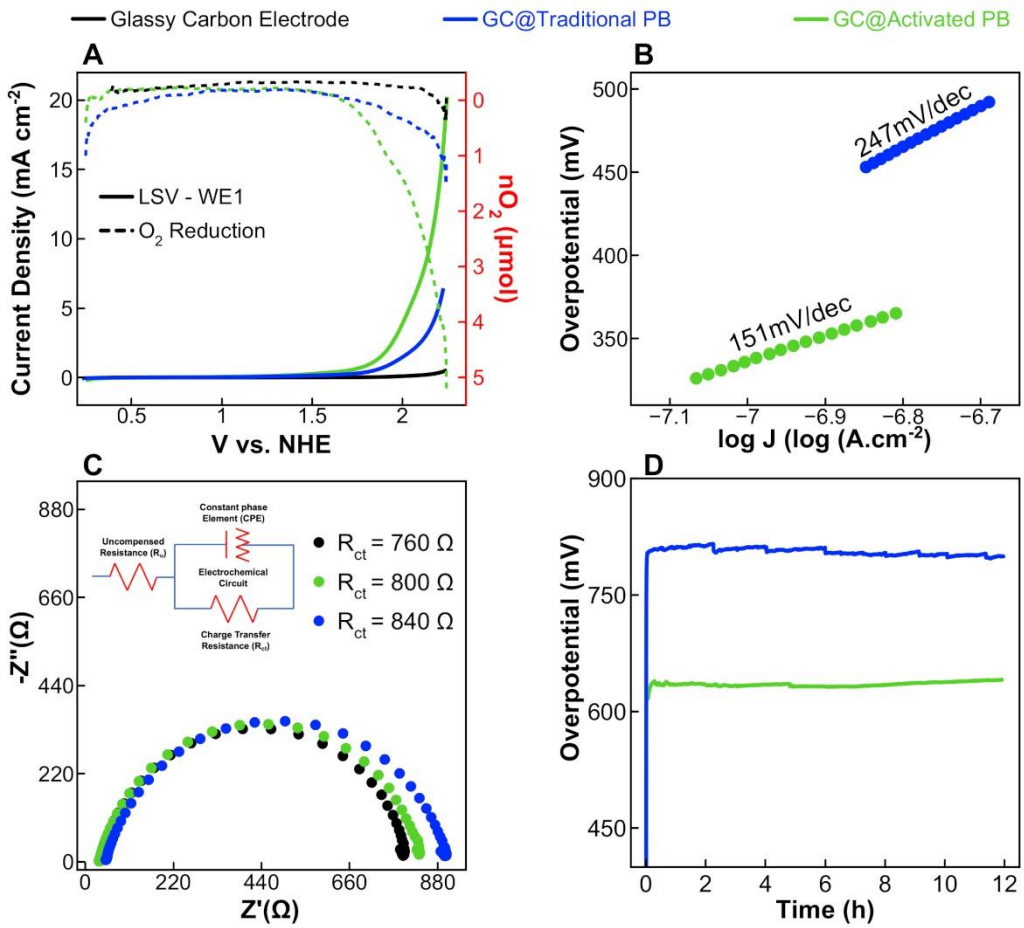

Figure 27. Water Oxidation reaction catalysis studies. Traditional Prussian Blue (blue line), Activated Prussian Blue (green line) and bare glassy carbon electrode (black line). A) Linear Sweep voltammetry (LSV) performed at 10 mV s^{-1} in 0.5 M KNO_3 solution in the 3D printed SECM cell, with two working electrodes set up, operating in the SG/TC mode. Straight line represents the LSV on the WE1 and dashed line represents the O_2 reduction current on WE2. B) Tafel slopes for the catalysts. C) Electrochemical Impedance Spectroscopy (EIS) performed at 1.9 V vs. NHE 1 in 0.5 M KNO_3 solution. D) Stability test performed at 1 mA cm^{-2} in 1 in 0.5 M KNO_3 solution for 12 hours.

The oxygen evolution was evaluated based on the top lines (dashed lines) in **Figure 27 A**, where 5.2 μmol of O_2 was produced at 995 mV with the APB, and 1.5 μmol with the TPB at the same overpotential. These numbers show that the production of O_2 for the APB was approximately 3.5 times higher compared to the TPB, indicating that it has clearly improved the performance

towards the WOR. The oxygen quantification details are presented in Supporting Information Section 4.3. The calibration curve for O_2 measurement is shown in **Figure 19**.

Under overpotential of 550 mV, APB presents a TOF of 1.5 x 10^{-2} s^{-1}, while TPB presents a TOF of 1.6 x 10^{-3} s^{-1}, which is almost 10 times smaller than the APB (see **Table 8**). Based on these results, it is possible to state that APB has faster kinetics and higher O_2 production than TPB.

Table 8. Electrocatalytic information for both catalysts.

Catalyst	ESCA (cm^2)	Onset η (mV)	η (1 mA cm^{-2})	η (5 mA cm^{-2})	Tafel (mV/dec)	Total Fe (nmol)#	TOF (s^{-1}) #
TPB	0.092	361	711	971	247	145.5	1.6 x 10^{-4}
APB	0.031	471	599	800	151	138.2	1.5 x 10^{-2}

#iron quantification (**Figure 20**) and TOF calculation are described in the experimental section for this Chapter.

The obtained Tafel slopes can provide information about how current density increases with the applied overpotential.[163] The corresponding plots are presented in **Figure 27 B**, where it is possible to observe a linear behavior between η= 300 and 360 mV, and η= 440 and 500 mV, with Tafel slopes of 151 and 247 mV/dec for APB and TPB, respectively. These results indicate the reaction mechanism in these materials can be different, whereas it is difficult to interpret the pathway followed by the reaction since surface intermediates, coverage, mechanisms, and rate-determining steps cannot be stated just by this analysis.[164] However, these values indicate the reaction kinetics for APB is faster, making it a better catalyst than the TPB. Moreover, the APB Tafel slope is very similar to previous results presented in the literature for PBAs.[69,83,84]

Electrochemical impedance spectroscopy (EIS) data show that modifying the GCE affects the charge transfer process between the electrode and the electrolyte. As it can be seen in **Figure 27 C**, the electrochemical fit circuit presents an uncompensated resistance (R_u) and a charge-transfer resistance (R_{ct}) in series, and a constant phase element (CPE) in parallel connection with R_{ct}. Since we worked with a modified electrode, the CPE is an expression of the capacitor element considering the electrode surface is not ideally smooth with exactly equal imaginary impedance components. However, the values of Y^0 for CPE are very small and almost do not change for the catalysts and the bare electrode. This is related to the fact that the capacitor impedance becomes negligible and acts only as a short-cut, facilitating the current flow. Thus, the impedance is only

dictated by R_u and R_{ct}.[141] The reported values for R_u were used for the IR drop compensation for the catalysis study and the R_{ct} values were considered to be the charge-transfer resistance for the catalysts and the bare electrode, as it can be seen in **Figure 27 C**. As expected, the R_{ct} increases with the GCE modification, since the electrode surface is not in direct contact with the electrolyte. When comparing both catalysts, they present R_{ct} of 800 and 840 Ω for APB and TPB, respectively. These results indicate the creation of defects on APB decreased the R_{ct}, suggesting a better electron transference inside the material, and this could explain the catalysis improvement. These results agree with the k^0_{obs} values shown above.

Stability tests were also carried out and they have showed the catalysts' activity operating at 1 mA cm^{-2} during 12 hours of electrolysis (**Figure 27 D**). Both catalysts have presented good stability at neutral pH. after 12 h. APB has an overpotential of 615mV at the beginning of the test, increasing it to 624 mV at the end, losing approximately 1.44% of its activity. Traditional Prussian Blue decreased its overpotential from 793 mV to 780 mV (1.63% lower). It is worth mentioning that there is no previous report of the TPB being a good catalyst for WOR, however, a change in the catalyst synthesis route to produce defects, created a new class of iron PB, having a great activity towards WOR, probably related to changes in the structure that facilitates the oxidation of water.

3.3.3 Spectroscopy studies

The electronic spectra of the films can be seen in **Figure 28**. For lower wavelength values (**Figure 28 A**), both catalysts present two distinct bands. The first band is assigned to the $^1T_{1g} \rightarrow {}^1A_{1g}$ ligand field transition of Fe^{2+} and the second one to the $^2T_{1g} \rightarrow {}^2T_{2g}$ ligand field transition of Fe^{3+}.[123] A bathochromic shift for the Fe^{2+} band when comparing TPB (λ = 365 nm) and APB (λ = 398 nm) is observed. This shift can be associated with the formation of more CN^- vacancies on the APB structure, leading to the coordination of water molecules on these vacancies. This could be explained by the fact that the ligand aquo (σ-donor) is a weaker π acceptor than cyanide, thus, the substitution of CN^- by H_2O would decrease the metal d orbitals splitting, therefore, decreasing its energy and shifting the band towards higher wavelengths, as observed.[165,166] For the second band, assigned to transitions on Fe^{3+}, the shift is almost negligible, located around λ = 416 and 425 nm

for TPB and APB, respectively. This small shift shows the changes in the structure are probably being created only at the Fe^{2+} sites.

Figure 28 B shows intervalence charge-transfer band, characteristic of Prussian Blue. This band represents the intervalence between Fe^{2+}-CN-Fe^{3+} and Fe^{3+}-CN-Fe^{2+} states.[165,167] When we compare the intervalence band of TPB ($\lambda = 723$ nm) and APB ($\lambda = 679$ nm), it is possible to observe a hypochromic shift. The intervalence band position is related to the PB level of oxidation, in which a higher level of oxidation shifts the band to higher wavelengths, having higher energy due to some destabilization in the structure.[165,167,168] Thus, these results indicate that APB has a lower level of oxidation, suggesting Fe^{2+} is predominant in its structure. In the case of TPB, this band appears at higher wavelengths, indicating a higher level of oxidation, with relatively more Fe^{3+} present in its structure. Hence, combining the observations from the ligand field and intervalence transitions, we propose the enhanced activity of APB arising from the presence of Fe^{2+} with an altered coordination shell comprised of water molecules partially substituting the CN^-.

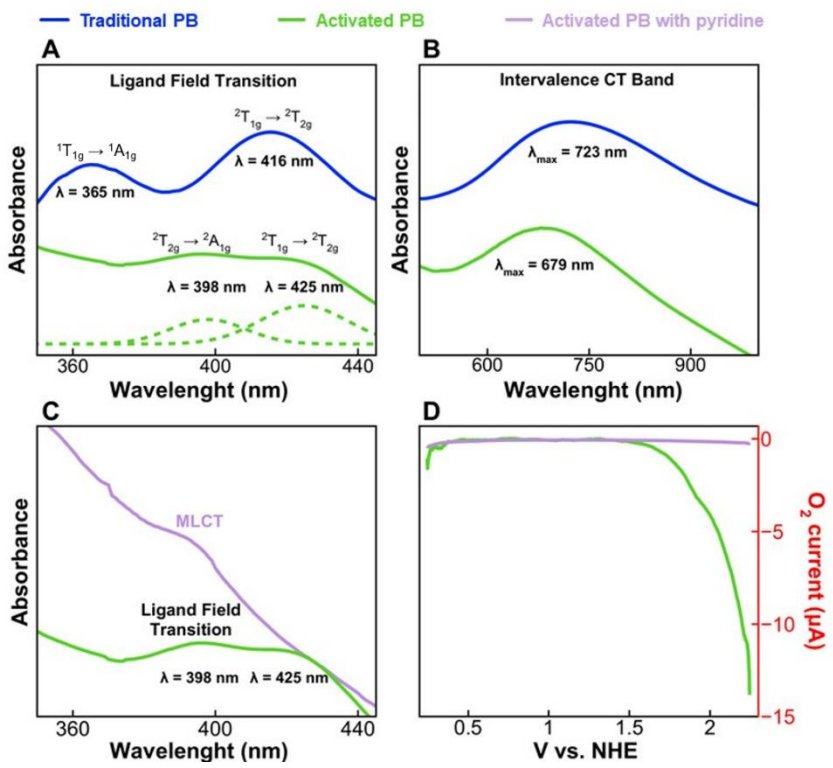

Figure 28. Spectroscopy studies and test with pyridine. Traditional Prussian Blue (blue line), Activated Prussian Blue (green line) and Activated Prussian Blue with pyridine (green dashed line). A) UV-Vis electronic spectrum from 350 to 460 nm of catalysts on FTO electrodes. B) UV-Vis electronic spectrum from catalyst's intervalence band, from 550 to 950 nm. C) UV-Vis electronic spectrum from 350 to 460 nm of Activated Prussian Blue with and without pyridine. D) O_2 evolution current of Activated Prussian Blue with and without pyridine.

As an attempt to verify the presence of vacancies in the APB structure, the modified electrode was immersed in pyridine. As a ligand, pyridine should coordinate to the vacant sites, replacing aquo ligands, and a metal-ligand charge transfer (MLCT) band in the electronic spectra must be observed. **Figure 28 C** shows the APB electronic spectra before and after the immersion in pyridine, and the MLCT band can be observed, indicating the coordination of pyridine into the defective Fe^{2+} site.[162,169] Besides, catalysis experiments were performed again, after the APB film immersion in pyridine, and no O_2 production was observed (**Figure 28 D**), indicating that the Fe^{2+} active sites were blocked by pyridine. This is another indication of the presence of vacancies on APB and that the active sites are the Fe^{2+}. The same test was carried out for TPB film, and no significant changes were observed in the electronic spectra (**Figure 28**).

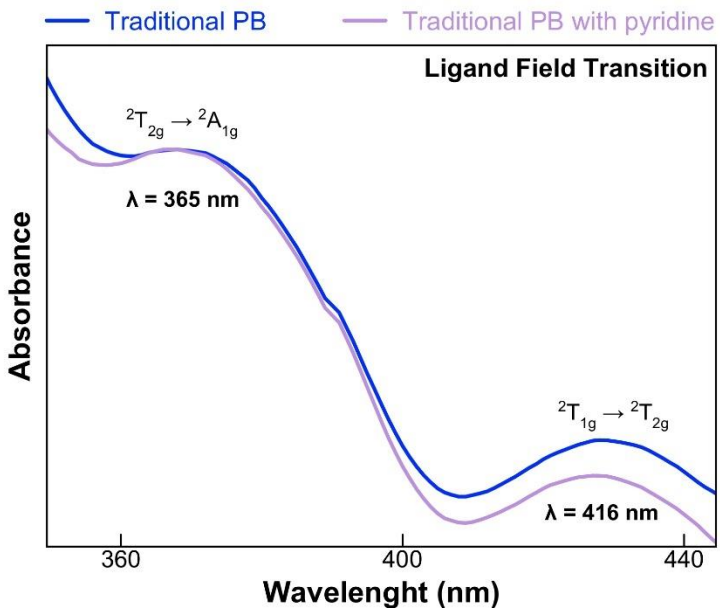

Figure 29. Spectroscopy studies and test with pyridine for Traditional Prussian Blue film.

Since the preliminary analysis indicates CN^- leaving the structure, mass spectroscopy (MS) was carried out in the solution after the film deposition, believing when CN^- leaves the structure, it reacts with the water present in the solution, forming isocyanate (OCN^-), that can form later an adult with hydronium (H_3O^+), forming OCN^---$^+OH_3$. This adult could be identified by mass spectrometry, having a mass to charge ratio of 62.02 (**Figure 30**), endorsing the proposal that CN^- is removed from the APB framework, allowing the coordination with water.

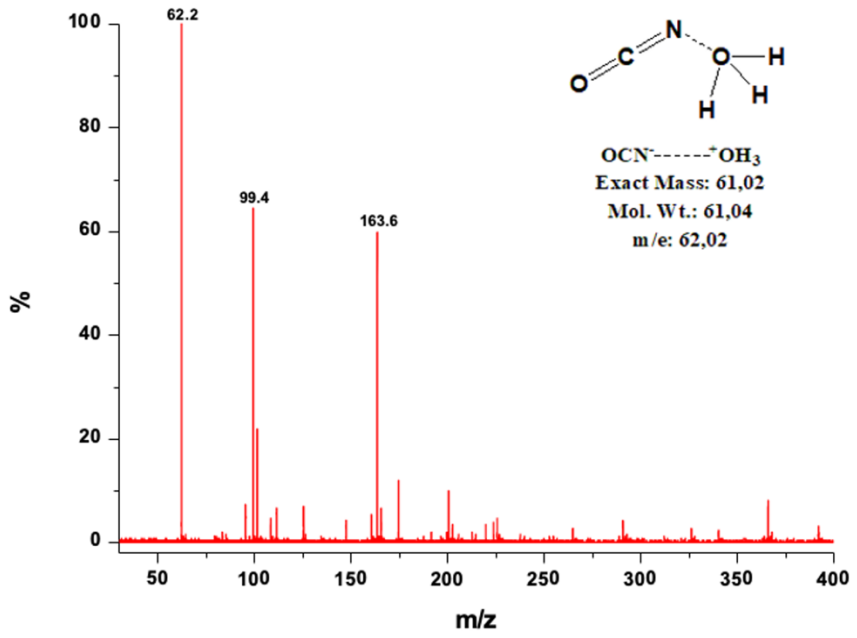

Figure 30. Mass spectra obtained from the $[Fe(CN)_6]^{4-}$ solution after Activated PB was synthetized to identify the Isocyanate ion.

Based on the previous results and the experimental evidence, herein we proposed a general scheme for the formation of defects in the APB structure (**Figure 31**). We believe these defects are characterized as cyanide (CN^-) vacancies, and H_2O molecules take their place, enhancing the WOR performance. Nonetheless, more *in-situ* experiments and DFT calculations must be carried out in order to validate this proposal.

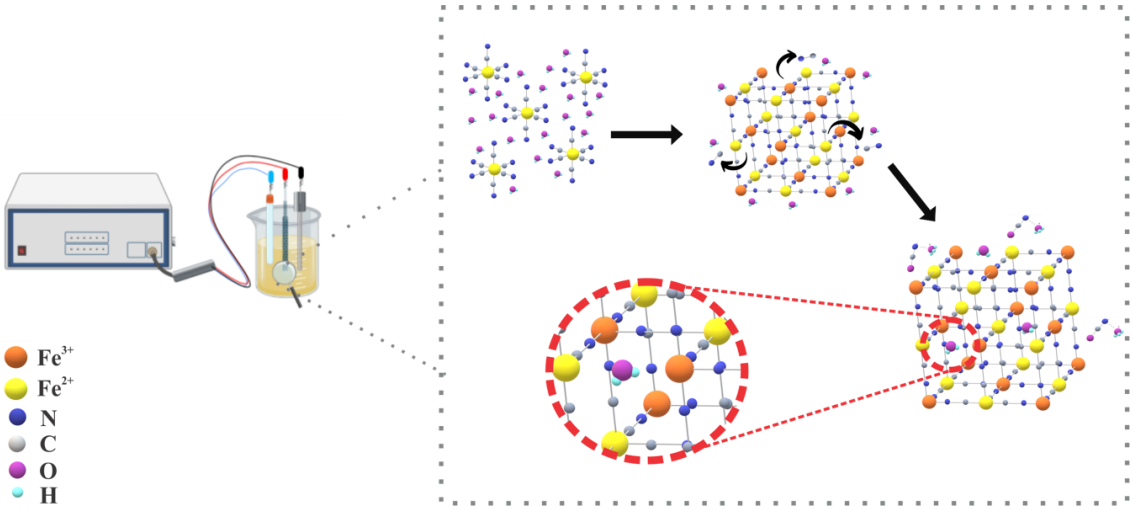

Figure 31. Scheme proposal for the vacancies creation on Activated Prussian Blue.

3.3.4 Morphological characterization

3.3.4.1 Scanning Electron Microscopy coupled with EDS (SEM-EDS)

The catalysts' morphology was also evaluated using scanning electron microscopy coupled with EDS (SEM-EDS), to have a better understanding on how the catalyst was on the electrode surface. As it can be seen on **Figure 32**, both catalysts are widely distributed over the surface, however TPB presents larger particles than APB, which is probably related to the film thickness, due to the different deposition methods that were used. Another interesting feature is that TPB appeared as cubic particles, while APB appeared as shapeless particles, showing that the catalyst "activation" probably influenced the morphology. Although, for both catalysts EDS analysis show the presence of iron, carbon and nitrogen all over the surface, showing that the materials are presented on a great area of the electrode. Further morphological characterization was conducted, and more SEM images were obtained, with a greater approximation (**Figure 33**). These new images confirm the TPB particles are bigger and spread in a higher volume over the FTO substrate. Besides, the particles present themselves as a cluster, where the cubic particles are aggregated. Meanwhile, although the APB particles are well spread over the film (EDS analysis confirms Fe homogeneously spread over the film - **Figure 34**), they are presented as smaller non-aggregated particles, and it can be responsible to increasing the electrode surface area, improving the electrode's performance towards WOR. Furthermore, these differences in the morphology are related to the different electrochemical synthesis methods that were used.

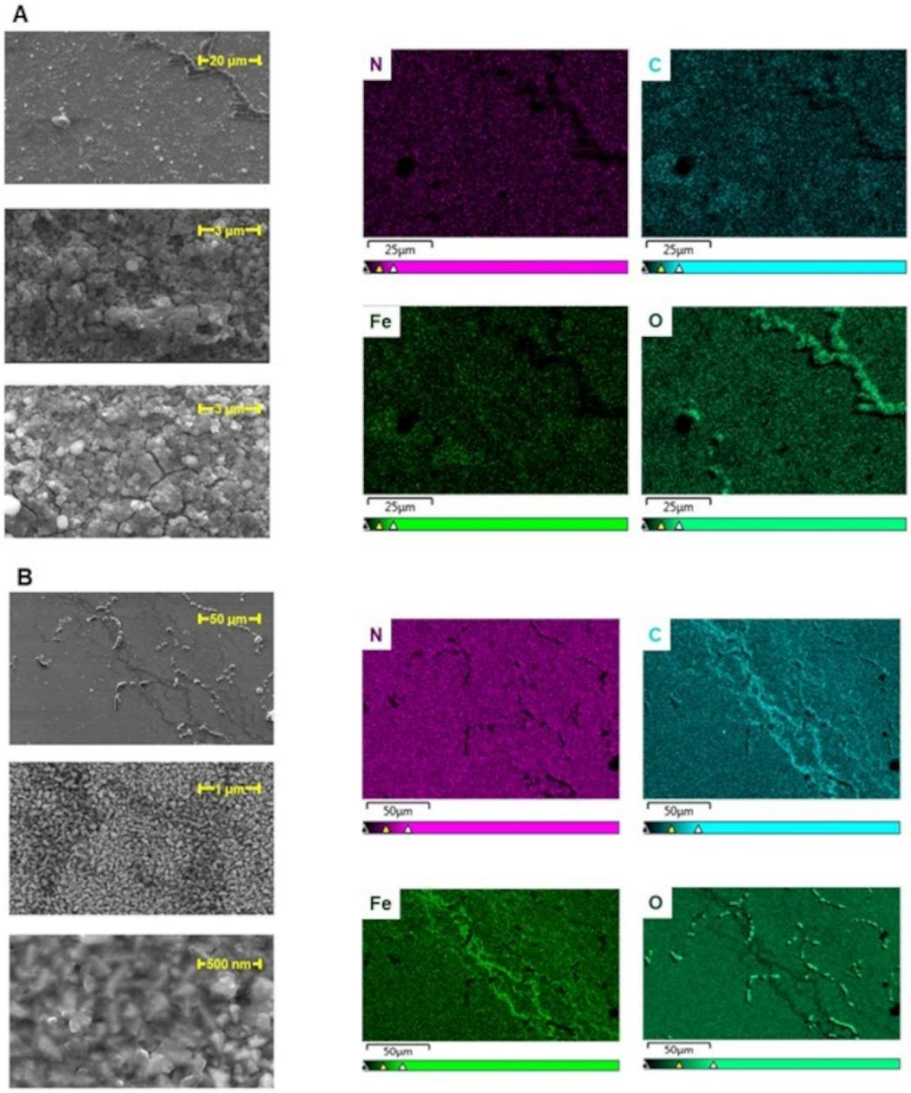

Figure 32. Scanning Electron Microscopy (SEM) with EDS mapping of the catalysts. (A) Traditional Prussian Blue. (B) Activated Prussian Blue.

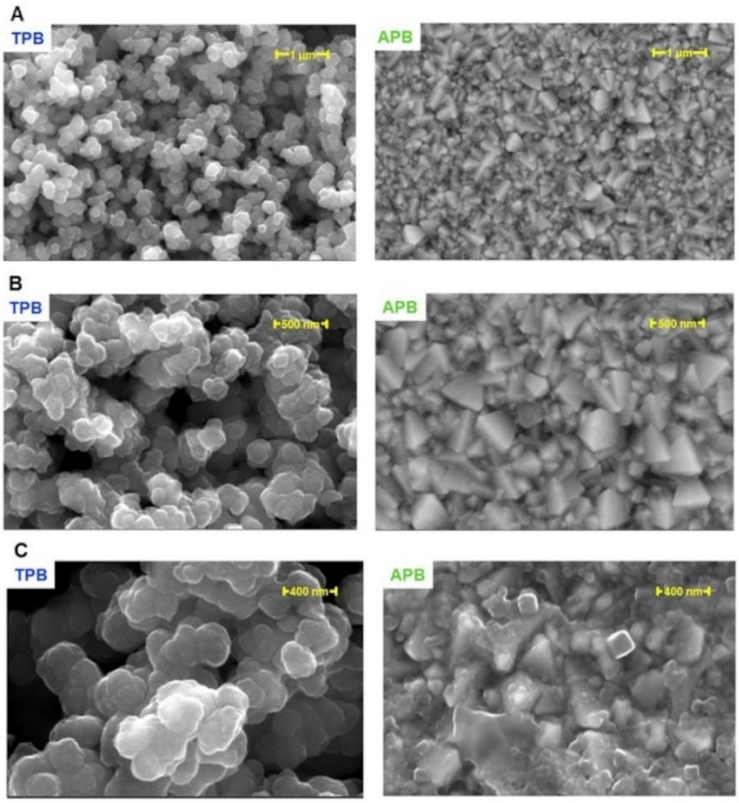

Figure 33. Scanning Electron Microscopy (SEM) of the catalysts. (A) Amplified in 30,000 times. (B) Amplified in 60,000 times. (C) Amplified in 120,000 times.

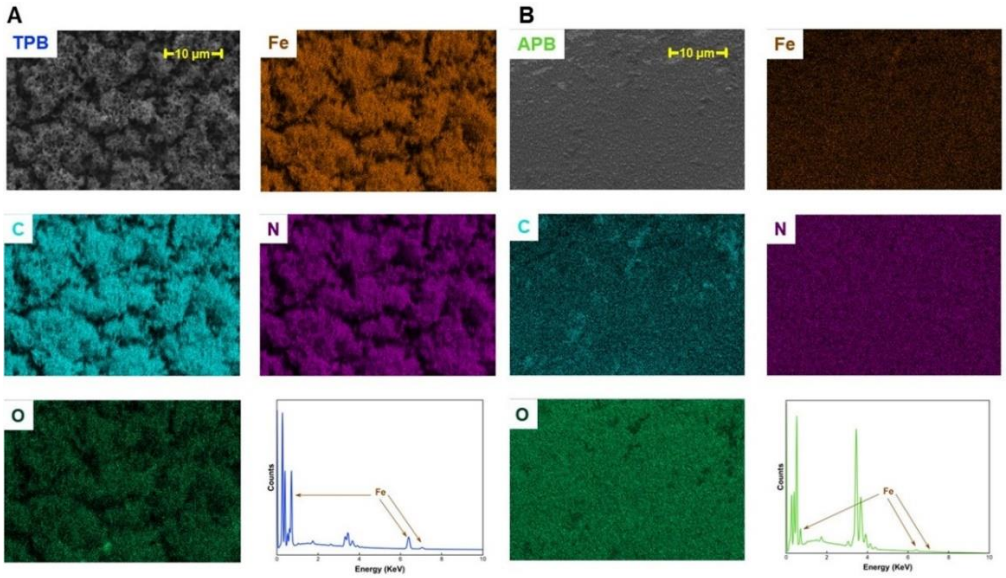

Figure 34. Scanning Electron Microscopy (SEM) coupled with EDS of the catalysts. (A) Traditional Prussian Blue. (B) Activated Prussian Blue.

3.3.4.2 Atomic Force microscopy

The films surface structure and surface potential were also evaluated using atomic force microscopy and Kelvin probe force microscopy. Although both films are widely distributed over the surface, 2D and 3D AFM images of the films, shown in **Figure 35**, reveal that TPB films do not cover the surface evenly, while APB films present a more even distribution over the surface. Additionally, KPFM images shown in **Figure 35** allow us to highlight areas where a smaller amount of the catalyst is observed on the surface (dark blue regions) in contrast with areas with greater accumulation of material (red regions). In this sense, although KPFM images show a heterogeneous distribution of surface potential for both films (which can be attributed to incomplete coverage of the substrate surface on the analysed region), it can be observed that APB films present high surface potential points distributed all over the analysed surface, while there are only concentrated higher surface potential regions on TPB films. Furthermore, we compare TPB and APB films applying the same size scale to AFM and same voltage scale to KPFM images: the images presented in **Figure 36** highlight that APB particles are smaller (average size = 0.2997 μm) and present greater surface potential (average potential = 0.6879 V) compared to TPB material (average values are 0.9440 μm and 0.3635 V). The average size observed agrees with the morphological characterization, confirming that APB films present smaller structures compared to TPB films. On the other hand, the increase in surface potential of APB compared to TPB indicates a surface with lower charge dissipation capacity which can be associated to the electrochemically CN^- vacancies created.

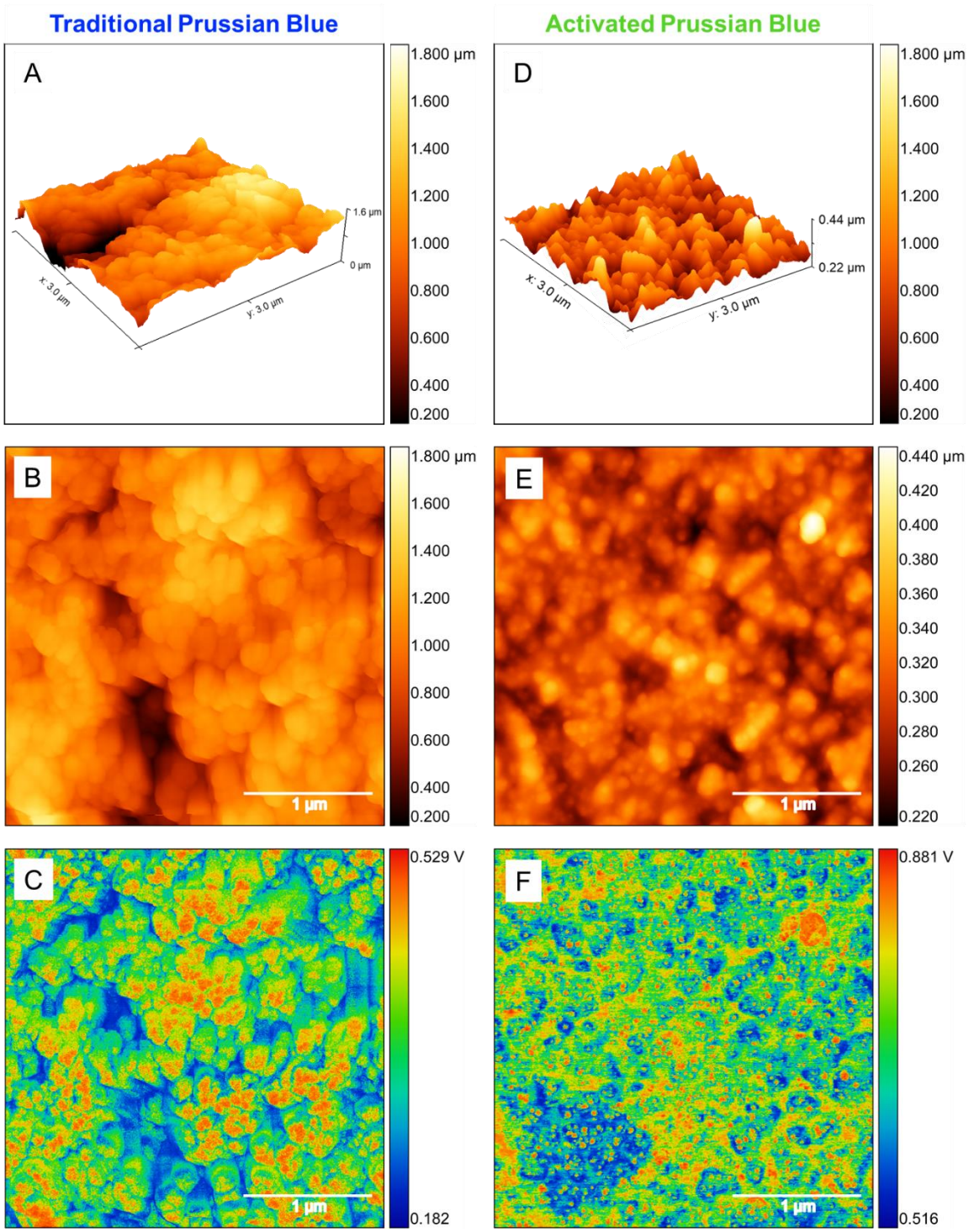

Figure 35. AFM and KPFM images of the samples obtained in a 3 µm x 3 µm area of the films. A) 3D and B) 2D AFM image of TPB film; C) KPFM image of TPB film; D) 3D and E) 2D AFM images of APB film; F) KPFM image of APB film.

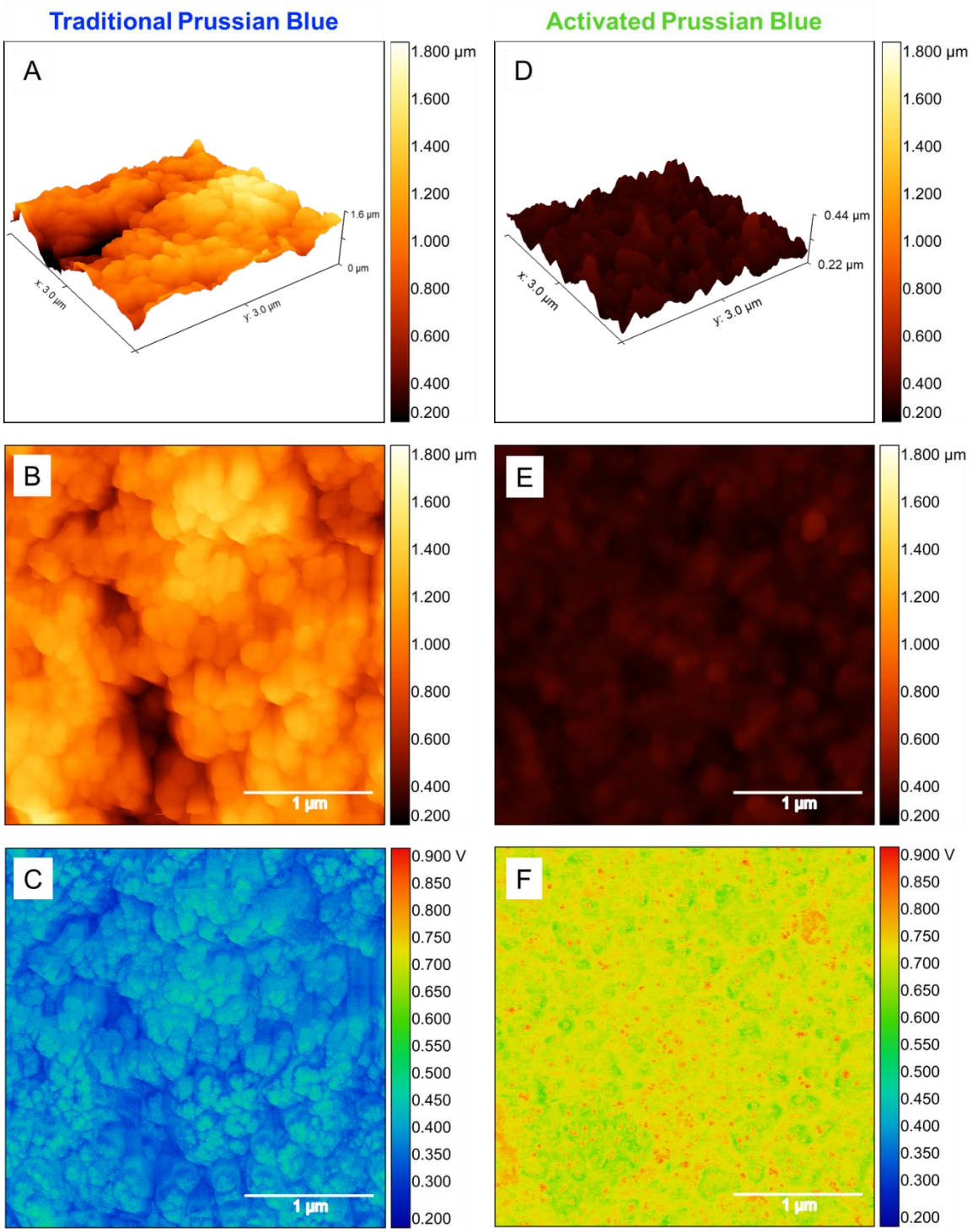

Figure 36. AFM and KPFM images of the samples obtained in a 3 µm x 3 µm area of the films under the same scale A) 3D and B) 2D AFM image of TPB film; C) KPFM image of TPB film; D) 3D and E) 2D AFM images of APB film; F) KPFM image of APB film.

3.3.5 Synchrotron-based soft X-ray spectroscopy

Synchrotron-based X-ray photoelectron spectroscopy (XPS) and soft X-ray absorption spectroscopy (XAS) (experiments were performed at IPÊ beamline of the synchrotron light source Sirius, at the Brazilian Synchrotron Light Laboratory (LNLS)), were used to probe the surface composition and Fe speciation of the films to assist the understanding of the nature of the defects on APB. As it's shown in the survey plot (**Figure 37 A**), from 1200 to 0 eV, the peaks related to Fe 2p (708 eV), O 1s (531 eV), Sn 3d (485 eV), N 1s (397 eV), C 1s (284 eV) and K 2p (284 eV) can be identified. The presence of Sn can be assigned to the substrate used as the electrode; fluorine doped tin oxide coated glass.

By analysing the Fe 2p peak, it is possible to obtain information about different oxidation states presented in the films. In both cases, it is possible to identify the presence of Fe^{2+} and Fe^{3+} on the film surface (**Figure 37 B**), agreeing with the well-known Prussian Blue structure, formed by a mixed $Fe^{2+/3+}$ valence. TPB presented peaks around 708 and 710 eV assigned to $2p_{3/2}$ Fe^{2+} and Fe^{3+} respectively, and peaks around 720 and 723 eV assigned to $2p_{1/2}$ Fe^{2+} and Fe^{3+} respectively, also presenting a satellite at 715 eV, assigned to Fe^{2+}. Meanwhile, APB presented peaks around 708 assigned to $2p_{3/2}$ Fe^{2+}, and peaks around 721 and 723 eV assigned to $2p_{1/2}$ Fe^{2+} and Fe^{3+} respectively, also presenting a satellite at 716 eV, assigned to Fe^{2+}.[170] The observed differences in the Fe 2p peak between TPB and APB indicates that although the films are similar in elementary composition, the structure and oxidation state over the film surface are different. The ratio between Fe^{2+}/Fe^{3+} is 1.15 and 2.31 for TPB and APB respectively, indicating a predominance of Fe^{2+} in the APB structure. This is in accordance with our experimental data, since APB was synthesized only from $[Fe(CN)_6]^{4-}$, indicating that only a part of these iron atoms are oxidized, and the mixed valence in the Prussian Blue framework is predominated by Fe^{2+}, indicating differences in the material's structure after the material activation.

X-Ray absorption spectroscopy (XAS) measurements were also carried out in the films and the Fe L-edge was analyzed in both cases (**Figure 37 C**). The main differences in the spectra related to the L2 and L3 areas main shape are related to the predominance of Fe^{2+} in the APB structure, thus, its spectra is similar to the one of $K_4[Fe(CN)_6]$, while the one for TPB resembles the $K_3[Fe(CN)_6]$ spectrum.[171] Furthermore, the APB spectra is shifted in 0.3 eV towards lower energies when compared to the TPB spectrum. This shift is observed for all peaks except the one at lowest energy (708 eV), which is assigned to the transition to the additional t_{2g} hole in the d manifold on

going from low-spin Fe(II) (t_{2g}^6) to low-spin Fe(III) (t_{2g}^5). The energy position of this feature relative to the main multiplet packet is affected by both 10Dq and multiplet interactions, thus it would not be affected by changes in the LUMO energy caused by a different crystalline field arrangement. As proposed by *Hocking et al,*[171] when a stronger π acceptor is replaced by a weaker π acceptor, the metal d orbitals splitting decreases, leading to a decrease in the LUMO energy, thus, this effect appears in the XAS spectra with a shift towards lower energies. Since in the APB XAS spectra it is observed a shift towards lower energies. The observed shift towards lower energies observed in the APB XAS spectrum indicates the replacement of CN^- (strong π acceptor ligand), by a weaker π acceptor ligand. These results support our proposal of created vacancies: CN^- ligands were removed from the structure through the activation process and replaced by aquo ligands, which are weaker π acceptor ligands compared to CN^-. Therefore, this is spectroscopy evidence of the creation of CN^- vacancies in the APB structure.

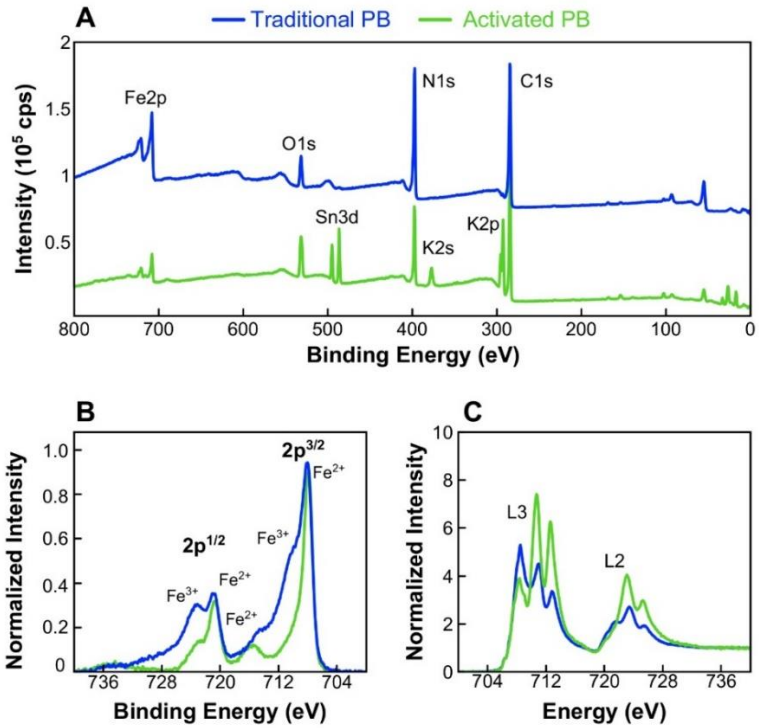

Figure 37. Synchrotron based soft X-ray spectroscopy for TPB (blue) and APB (green). A) XPS survey spectra with main peaks assigned to their respective elements and transitions. B) high resolution Fe 2P spectra. C) Fe L-edge XAS spectra.

3.3.6 Laser ablation inductively coupled plasma mass spectrometry (LA-ICP-MS)

Laser ablation inductively coupled plasma mass spectrometry (LA-ICP-MS)[101,147,148] analysis was carried out as an attempt to obtain qualitative information about the Fe/C ratio and spatial distribution on the film and to confirm the vacancy formation. The results presented on **Figure 38** and **Figure 39** indicate the distribution of Fe and C over the TPB and APB films and both films show a homogeneous distribution of iron all over the film, indicating a good film deposition. The difference in the Fe signal intensity concentration for both films can be related to the different electrochemical method of synthesis, not indicating great differences in the materials.

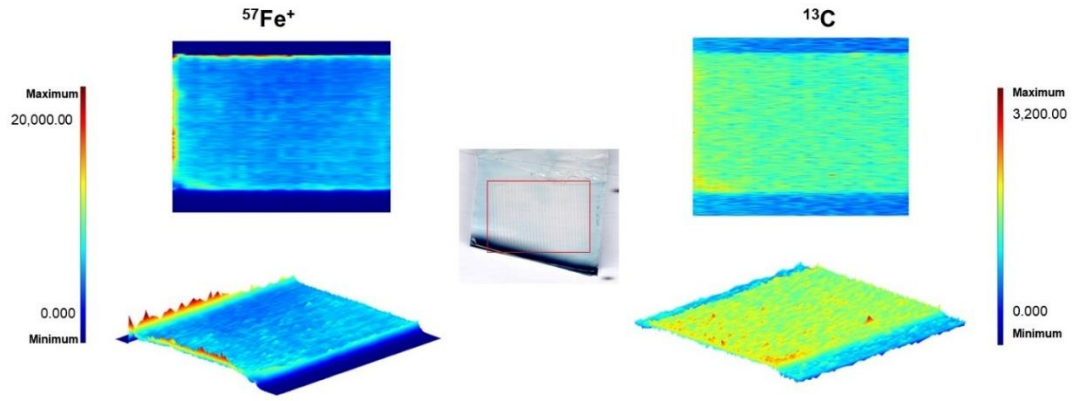

Figure 38. LA-ICP-MS qualitative mapping for Fe on TPB film. Inset represents the film picture with the scan area highlighted.

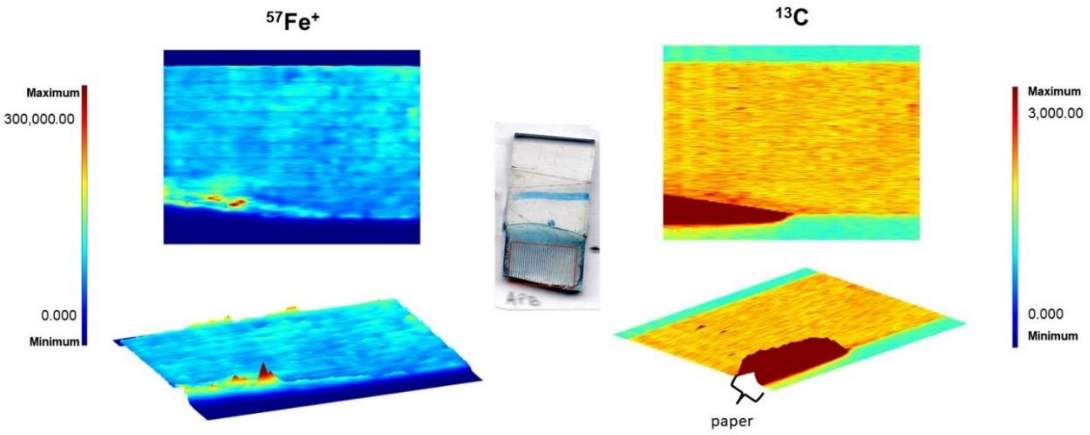

Figure 39. LA-ICP-MS qualitative mapping for Fe and C on APB film. Inset represents the film picture with the scan area highlighted.

Furthermore, these results were used to study and identify the presence of vacancies in the APB film. Since we believe the film has CN^- electrochemically formed vacancies, the removal of CN^- from the structure would increase the ratio between Fe and C. Therefore, to analyze and identify the presence of vacancies in the APB structure we investigated and compared the Fe/C ratio for both films. **Figure 40** shows a 3D mapping on the Fe/C ratio intensity for both films, indicating a higher Fe/C ratio for APB with an average value of 39.7, while for TPB shows a Fe/C ratio in the range of 2.7 (**Figure 40**), which is close to the nominal value for the Prussian Blue structure, 2.9.[39] According to this, APB has the Fe/C ratio 14.7 times higher than TPB, indicating a lower concentration of carbon in the APB, and it can confirm the loss of carbon (as CN^-) during the film synthesis. Therefore, these results and their comparison can confirm APB activation process and synthesis route have created CN^- vacancies on the film, and it directly affects and improves the catalyst activity and performance towards WOR, resulting in a lower overpotential and higher TOF values, as it has been previously discussed. Besides, it is also worth mentioning that increasing the Fe/C ratio by 14.7 times had also increased the TOF by almost 10 times; thus, the creation of vacancies in the structure enabled the catalyst to produce more O_2.

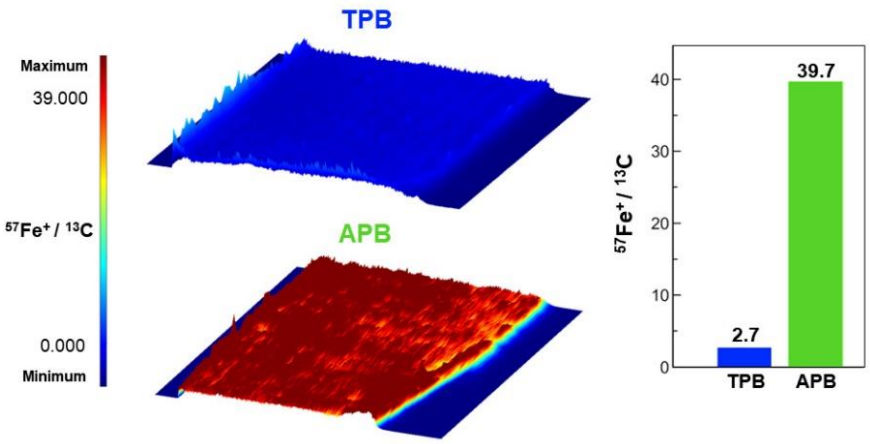

Figure 40. Laser ablation inductively coupled plasma mass spectrometry (LA-ICP-MS) qualitative mapping to obtain the ratio between Fe/C in the TPB and APB films.

3.3.7 Active Sites quantification

Based on the results and with the belief the active sites in the APB are vacancies in Fe^{2+}, we proposed a method to quantify these active sites and obtain a more accurate value for TOF. Since previous experiments proved the coordination of pyridine in the active sites (**Figure 28**),

eradicating the catalysis, it was used for quantifying active sites in the APB. In this way, after immersing the films in pyridine, washing them with water and dissolving them in NaOH, the pyridine left in the catalyst solution was quantified by a spectroscopic method, and the result is believed to be direct related to the number of active sites. We made this assumption since the pyridine coordinated to the active sites during the film immersion, became part of the solution after the film dissolution. The pyridine concentration was obtained according to a calibration curve previous prepared.

As it can be seen in the pyridine electronic spectrum (**Figure 41**) 3 main peaks can be identified around 252, 256 and 258 nm, with a maximum at 258 nm. Since pyridine is a heterocyclic compound, these peaks can be assigned to the electronic transitions resulting from the combination of $\pi \rightarrow \pi^*$ and $n \rightarrow \pi^*$ transitions. In this work, the maximum absorbance at 258 nm was used for the calibration curve and pyridine quantification, further relating it to the number of active sites in the APB.

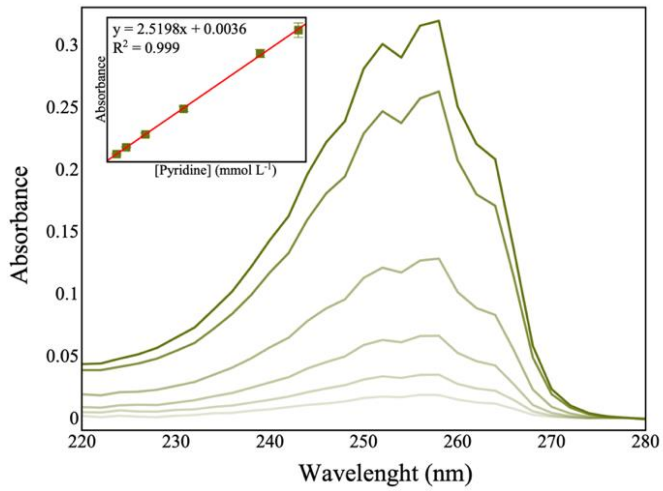

Figure 41. Calibration curve for pyridine for different solution concentrations using UV-Vis spectroscopy.

In this sense,

Table *9* presents a comparison between ECSA, the total amount of Fe, the number of active sites, TOF_{total}, and TOF_{cat} for APB. As it can be seen, when TOF is calculated using the total amount of iron, is in the range of 10^{-2}. However, when the number of active sites is exclusively considered, it increases to a range of 10^{-1}, increasing it by 14.80 times. Thus, this experiment shows an outstanding activity for a PBA never reported before (0.2170 s^{-1}). Besides, it is important to

highlight that these results are related to a PBA containing only iron atoms, without the modification with other elements (*e.g.* Co, Ni, Cu, etc.)

Table 9. Electrocatalysis information for APB, based on the quantification of active sites with pyridine.

	ECSA *(± 0.008)*	**Total Fe** *(± 0.50)*	**Fe Active sites** *(± 0.97)*	**TOF_{total}** *(± 0.0023)*	**TOF_{cat}♣** *(± 0.0110)*	**TOF_{total}/TOF_{cat}**
APB	0.0313 cm^2	138.15 nmol	8.81 nmol	0.0149 s^{-1}	0.2170 s^{-1}	14.78

♣ Since TPB does not have enough vacancies for pyridine coordination and quantification, TOF_{cat} was only calculated for APB.

3.4 Conclusion

In summary, we presented an alternative and simple way to synthesize Prussian blue with vacancies created by an electrochemical method. The new material was used as a catalyst, showing an outstanding performance in the water oxidation reaction. Spectroscopic analysis using pyridine as a molecular probe indicated the presence of vacant Fe^{2+} sites on APB structure, and the quantification of these sites allowed the obtention of a higher TOF number never reported. Since this is a simple method to produce vacancies in an Earth-abundant element catalyst, our results open a great opportunity to study other PBA with those electrochemically formed vacancies, expecting outstanding activities towards the water oxidation reaction.

3.5 Acknowledgments

The authors are grateful for the financial support of Brazilian Funding Agencies. This study was financed in part by the Coordenação de Aperfeiçoamento de Pessoal de Nível Superior - Brasil (CAPES) - Finance Code 001, Conselho Nacional de Desenvolvimento Científico e Tecnológico CNPq (grant#308203/2021-6) and Fundação de Amparo à Pesquisa do Estado de São Paulo, FAPESP (grant#2014/50867-3, grant#2017/11986-5, grant#2017/50085-3, grant#2018/25092-9, grant#2018/25207-0, grant#2019/00063-9, grant#2019/2445-8, grant#2021/05976-2). This research used facilities of the Brazilian Synchrotron Light Laboratory (LNLS), part of the Brazilian Center for Research in Energy and Materials (CNPEM), a private non-profit organization under

the supervision of the Brazilian Ministry for Science, Technology, and Innovations (MCTI). The IPE beamline staff is acknowledged for their assistance during the experiments 20220865.

Chapter IV

Electrochemical designed cyanide vacancies influence on CoFePBA-based catalysts boosted performance during the Oxygen Evolution reaction under mild conditions

The content of Chapter IV is an adaptation of the manuscript under preparation for publication entitled “Electrochemical designed cyanide vacancies influence on CoFePBA-based catalysts boosted performance during the Oxygen Evolution reaction under mild conditions” by Rafael L. Germscheidt, Ana B. S. de Araujo, João P. B. de Souza, Eduarda Q. Machado, Marco A. Z. Arruda, Túlio C. R. da Rocha, Juliano A. Bonacin.

Graphical Abstract

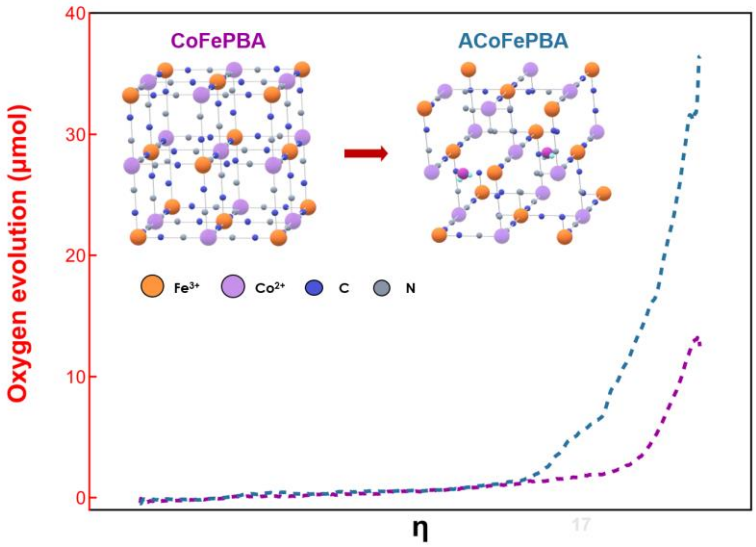

4.1 Introduction

Hydrogen presents itself as a great alternative and a symbol for a sustainable world.[7,24] It has a wide range of applications, including in the petrochemical industry, helping with petrol refining; in the chemical industry, being the feedstock for ammonia production (the main source for fertilizers); and also as a fuel source through combustion or in Fuel Cells.[2] Moreover, the hydrogen demand has been increasing in the past few years and it is expected to increase even more in the next few decades. Nonetheless, all hydrogen environmental advantages are related to its way of production and the green and sustainable hydrogen can be obtained from a well-known process named Water Splitting (WS).[2,16]

During the WS process, hydrogen is produced through an electrochemical process, where at the anode oxygen is evolved, in a process called Oxygen Evolution reaction (OER), providing the necessary electrons and protons so hydrogen can be evolved through the Hydrogen Evolution reaction (HER) at the cathode. Nevertheless, the bottleneck reaction, the OER, is both kinetic and thermodynamic unfavorable and it requires a catalyst to be efficient.[33,53,55]

In the search for cheap and earth-abundant catalyst that operate under mild conditions for OER has brought attention to Prussian Blue analogues (PBAs).[4,125,172] They are represented by $M_{1(x)}[M_2(CN)_6]_{(y)}$, where M_2 is an hexacyanometalate that plays a structural role and it can modulate the donor-acceptor effect to the other metal and M_1 a first-row transition metal and it is coordinated to the N atoms forming a 3D network.[78–80] This material is also very interesting for presenting a mixed spin/valence structure, and for the OER, the CoFePBA is widely studied[35,83,84,125,134] and it is usually organized with Fe^{3+} d^5 in a low spin configuration, while Co^{2+} d^6 assumes the high spin configuration.[81,82] Although having a great performance, their activity is limited by the low concentration of active sites, thus, the design and creation of vacancies can be the best strategy to increase number active sites and improve their catalytic activity.[1,4,125]

Furthermore, synchrotron-based soft X-ray spectroscopy, including X-ray absorption (XAS) and X-ray photoelectron spectroscopy (XPS) are element-specific methods that allow the probing of materials composition, different valence states in the elements and can provide insights about electronic states.[173,174] Thus, their unique sensitivity can help to probe and identify vacances and structural changes on earth-abundant based catalysts, with an highlight to PBA.[4]

Hance, this chapter presents the creation of electrochemically formed cyanide vacancies in a CoFe Prussian blue analogue. The enhancement on the catalytic activity was probed by quantifying the amount of oxygen evolved and then related to the improvement in cyanide vacancies within the structure. Furthermore, synchrotron based soft X-ray spectroscopy was used to investigate and probe these vacancies and gave insights on their role in the modulation of metallic sites oxidation states.

4.2 Experimental Section

4.2.1 Catalyst preparation and substrate modification

FTO substrates of 1 × 2.5 cm^2 were cleaned using isopropyl alcohol in an ultrasonic bath for 10 minutes, rinsed with distilled water, and cleaned again in an ultrasonic bath using distilled water for 10 minutes. After that, the substrates were annealed in a muffle at 400 °C for 30 minutes.[69] Then, the FTO was used on the electrodeposition step as the working electrode, Ag/AgCl 3.5M electrode as a reference electrode and a platinum wire as an auxiliary electrode.

4.2.1.1 CoFe Prussian Blue analogue

The electrode was immersed in a solution containing 0.1 mol L^{-1} of $Co_2(SO_4)_3$, 0.1 mol L^{-1} of KNO_3 and 5uL of H_2SO_4, then a potential of -1.5 V x Ag/AgCl 3.5 M was applied to the WE for 60 seconds and the metallic film was formed over the surface. Then, this film was oxidized by immersing the electrode in a solution containing 10 mmol L^{-1} of $K_3[Fe(CN)_6]$ and a potential of 0.5 V x Ag/AgCl 3.5 M was applied to the WE for 250 seconds, a brown film was observe on the electrode. The electrode was dried before further tests.

4.2.1.2 Activated CoFe Prussian Blue

The electrode was immersed in a solution containing 0.1 mol L^{-1} of $Co_2(SO_4)_3$, 0.1 mol L^{-1} of KNO_3 and 5uL of H_2SO_4, then a potential of -1.5 V x Ag/AgCl 3.5 M was applied to the WE for 60 seconds and the metallic film was formed over the surface. Then, this film was oxidized by immersing the electrode in a solution containing 10 mmol L^{-1} of $K_3[Fe(CN)_6]$ and a potential of 2.2 V x Ag/AgCl 3.5 M was applied to the WE for 250 seconds, a brown film was observe on the electrode. The electrode was dried before further tests.

4.2.2 Electrochemical characterization

All electrochemical measurements were carried out in a 0.5 mol L^{-1} KNO_3 electrolyte, using a 3-electrode arrangement. With a Ag/AgCl 3.5 M working as the reference electrode, Platinum wire as the auxiliary electrode and FTO modified substrate as the working electrodes.

The water oxidation studies were performed on the 3D printed SECM cell, operating at the substrate generation – tip collection mode (SG/TC), using a 4 electrodes arrangement. The cell design was adapted for FTO from the system developed by our group and described in details on Chapter III.[4] Using this mode, O_2 is generated on the WE1 surface, during the WOR, furthermore it diffuses towards the WE2, biased at the potential required to reduce O_2, and the measured current can be related to the O_2 evolution. The modified FTO electrode was used as the WE1, Ag/AgCl 3.5 M as a reference electrode, a platinum wire as an auxiliary electrode, and a micro sized platinum wire as the WE2.

4.2.3 Further characterization

Further characterization methods including Vibrational Spectroscopy (Raman) characterization for the materials; Electrochemical Active Surface Area (ECSA) and Heterogeneous electron transfer rate constant (k^o_{obs}) calculation; UV-Vis Spectroscopy characterization for the materials; SEM images; XPS and XAS analysis and LA-ICP-MS measurements followed the same methods and parameters reported by our group in a recent publication[4] and presented in the experimental section on Chapter III.

4.3 Results and discussion

4.3.1 Synthesis and Characterization

4.3.1.1 Film synthesis

Cobalt-Iron Prussian blue analogue (CoFePBA) and activated Cobalt-Iron Prussian blue analogue (ACoFePBA) were electrodeposited onto a FTO electrode substrate according to the

procedures described in the Experimental Section. CoFePBA was deposited according to a method already described in the literature, consisting of a chronoamerometry.[69] and the current evolution curves can be seen on **Figure 42**. In this way, first a metallic cobalt (Co^0) film is obtained by the reduction of Co^{2+} present in the electrolyte (**Figure 42 A**). Then, the film is oxidized to Co^{2+} in the presence of $[Fe(CN)_6]^{3-}$, leading to the formation of CoFePBA (**Figure 42 B**), a 3D framework with a general structure like $Co_y[Fe(CN)_6].nH_2O$.[83,84] Moreover, ACoFePBA was deposited according to an activation method proposed by our group,[4] in which after the Co^0 film deposition, the electrolyte containing $[Fe(CN)_6]^{3-}$ was oxidized along with some cyanide groups, due to a high potential application (**Figure 42 C**). This resulted in the material activation due to the formation of some cyanide vacant sites that are replaced by water.

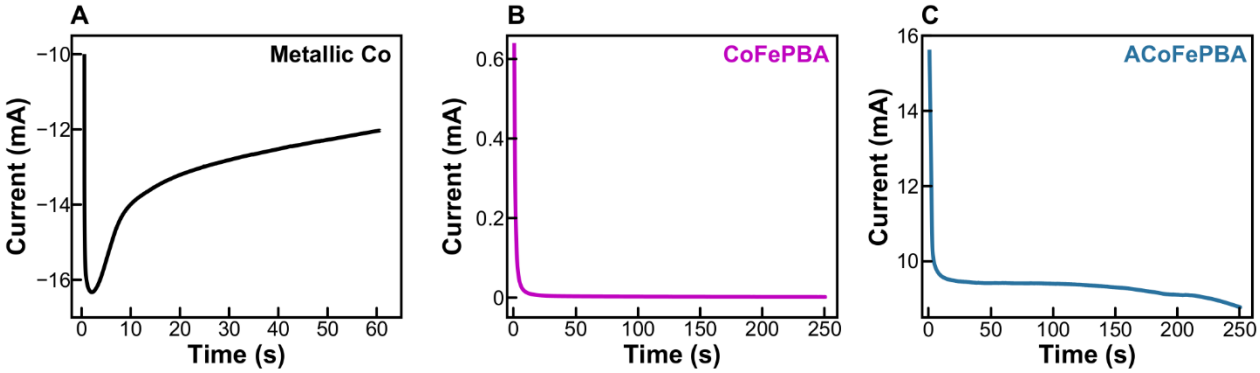

Figure 42. Current evolution during the catalysts film deposition. A) Metallic cobalt deposition. B) CoFePBA deposition and C) ACoFePBA deposition.

4.3.1.2 Morphological Characterization

The electrodes were characterized by Scanning electron microscopy (SEM) in order to get some information about how the films were spread over the electrode, and also to understand if the material activation has some morphological impact. The results can be seen in **Figure 43** and no huge differences can be observed in the material morphology with the activation process. CoFePBA structure is more shape-defined, presenting the square shaped-like structure reported for PBAs. Besides, these particles are presented in a more agglomerated way in some parts of the film. Furthermore, ACoFePBA presents a more amorphous structure, with smaller particles spread in a better way over the thin film, with a lower appearance of agglomerated areas. Nonetheless, SEM

images for both materials suggest that material synthesis resulting in the electrodes modification was successful.

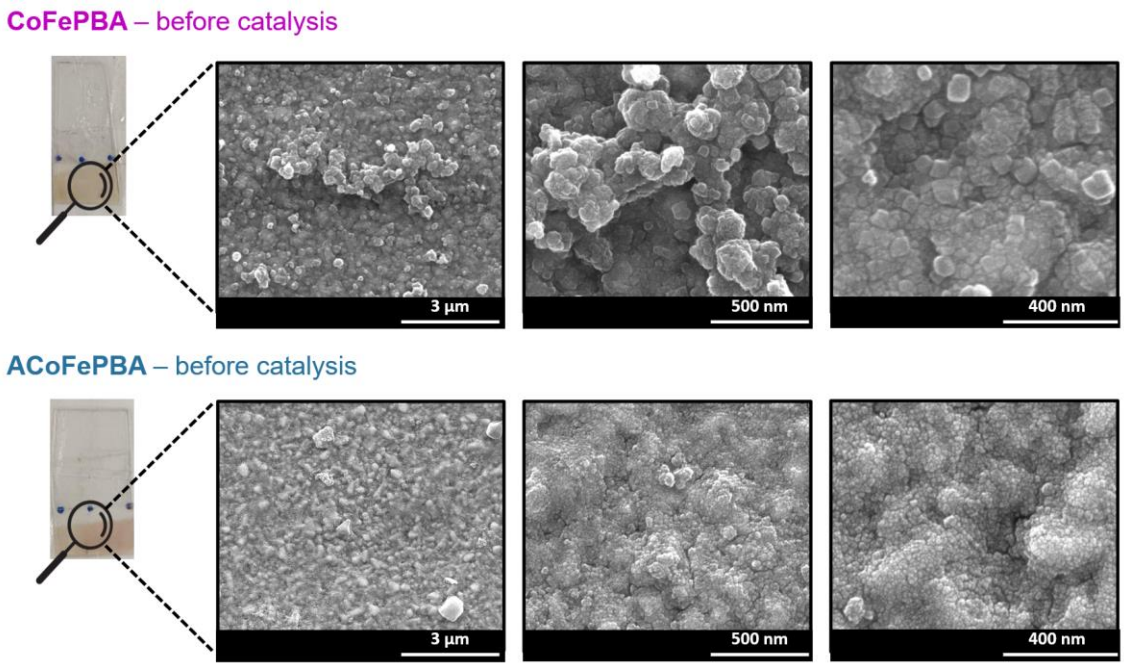

Figure 43. Scanning Electron Microscopy (SEM) of the as prepared catalysts (before catalysis).

4.3.1.3 Spectroscopy studies

Furthermore, the catalysts were characterized by vibrational Raman spectroscopy to gain a deeper understanding on their structural properties and the results can be seen in **Figure 44 A**. As it is shown, both materials present the bands related to the cyanide stretching vibrations (ν(CN)), known as the fingerprints from PBA structures, indicating that the material activation maintains the PBA general framework. The two main observed bands can be assigned to the A_{1g} and E_g mode of ν(CN) stretching vibration.[4,125,175,176] Moreover, it is possible to notice a shift towards higher wavelengths for these bands, going from 2098/2130 cm^{-1} for CoFePBA to 2105/2140 cm^{-1} for ACoFePBA. This shift can be assigned to iron species with a higher oxidation state that are probably present in the material structure after the activation and probable vacancies formation. This can be related to the fact that higher metal oxidation states can strengthen σ-bonding and since electrons are removed from a weakly anti-bonding orbital, the metallic center oxidation can result in the increasement of the ν(CN), thus, shifting the bands towards higher wavelengths.[159,177]

Therefore, this can indicate that the activation process, linked with the formation of cyanide vacancies, can modulate the metals oxidation state as a way to introduce neutrality in the structure.

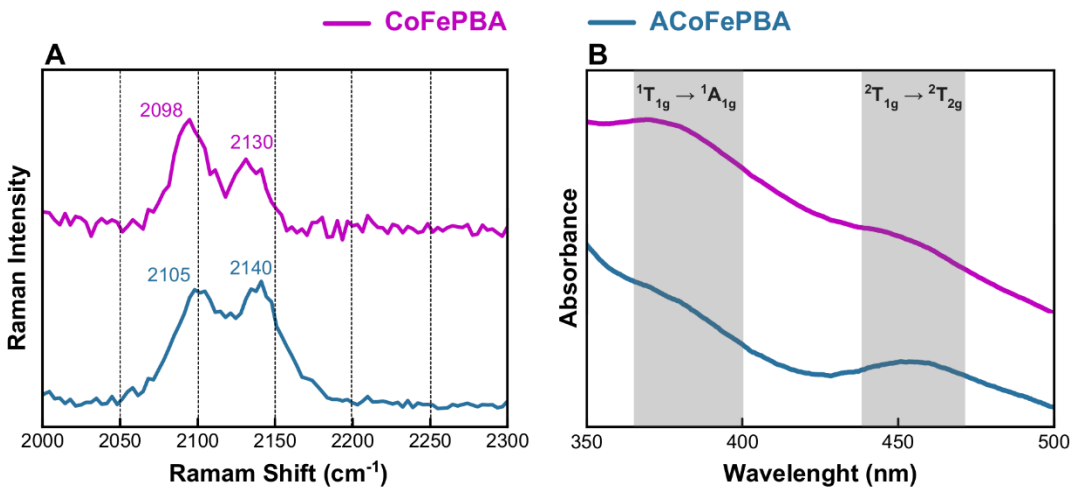

Figure 44. Spectroscopic characterization. CoFePBA (pink line) and Activated CoFePBA (blue line). A) Raman spectra obtained using a 785 nm laser excitation for the modified FTO electrodes to study the materials ν(CN) stretching vibration. B) UV-Vis electronic spectrum from 350 to 500 nm of catalysts on FTO electrodes.

UV-Visible electronic spectroscopy was also used to probe the catalysts' structure and the results are shown in **Figure 44 B**. As it is presented, both materials present 2 distinct bands and can be assigned to the $^1T_{1g} \rightarrow {}^1A_{1g}$ ligand field transition of Fe^{2+} and to the $^2T_{1g} \rightarrow {}^2T_{2g}$ ligand field transition of Fe^{3+}, respectively.[123] The comparison between both of them indicates that the material activation process (ACoFePBA) results in a bathochromic shift for both bands, going from 370 and 444 nm for CoFePBA to 380 and 459 nm for ACoFePBA. As discussed in chapter III and recently published by our group, this bathochromic shift can be associated with the formation of CN^- vacancies with the material activation.[4] The creation of CN^- vacancies during the material activation implies in the substitution of CN^- by some water molecules. The ligand aquo, a σ-donor, is known as a weaker π acceptor comparing with cyanide, thus, its substitution would result in the decreasing on the metal d orbitals splitting. Therefore, resulting in a shift of the band towards higher wavelengths, as it can be observed in the plot (**Figure 44 B**).[165,166]

4.3.1.4 Electrochemical paraments

Some electrochemical parameters such as Electrochemical Active Surface Area (ECSA), heterogeneous electron transfer rate constant (k^0_{obs}) and superficial concentration of electroactive Co^{2+} sites ($[Co]_{surf.}$) were determined from cyclic voltametric characterization. These paraments helped us to understand how the activation process impacts the material during electrochemical studies and the CV plots are shown in **Figure 45**.

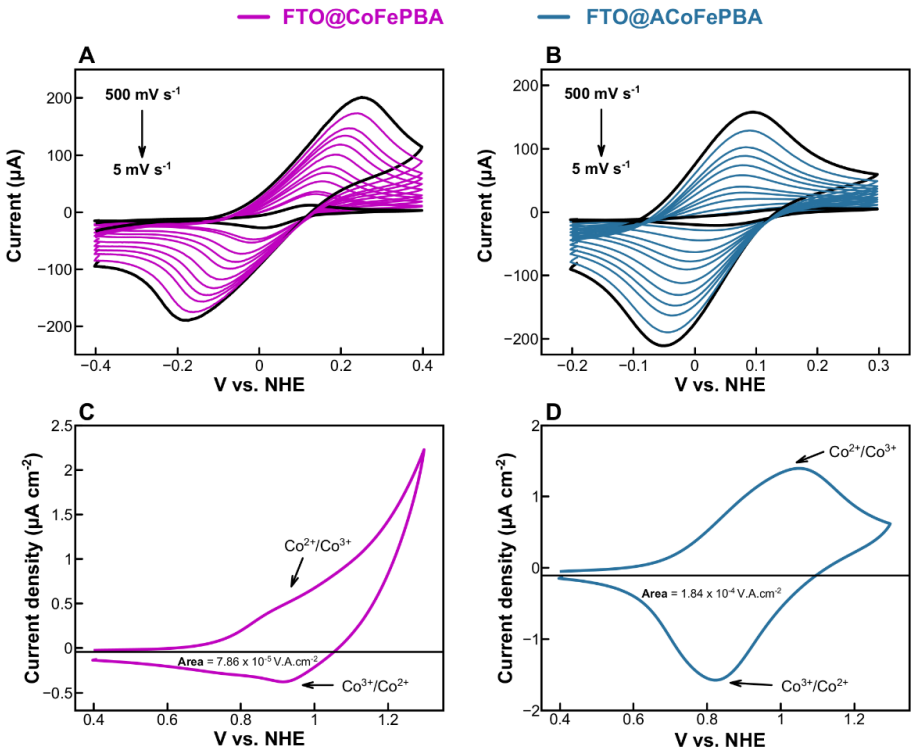

Figure 45. Cyclic voltammetry performed using $[Ru(NH_3)_6]Cl_3$ probe in different scan rates. A) CoFePBA. B) ACoFePBA. Cyclic voltammetry performed at 100 mV s^{-1} in 0.1 mol L^{-1} KNO_3 electrolyte for superficial cobalt sites determination. C) CoFePBA and D) ACoFePBA.

ECSA were obtained by CV measurements (**Figure 45 A** and **B**) performed using $[Ru(NH_3)_6]Cl_3$ as a redox probe at different scan rates (5.0 to 500 mV s^{-1}), according to the Randles–Ševčíck equation (3)[145], where Ip is the peak current, A is the electrode area, C is the concentration of the redox probe, D is the diffusion coefficient, n is the number of electrons transferred.

$$I_p = 2.69\ x\ 10^5 ADC^{\frac{1}{2}} n^{\frac{3}{2}} \nu^{\frac{1}{2}}$$

The reported ECSA values for CoFePBA and ACoFePBA are 0.29 ± 0.03 and 0.34 ± 0.03 cm^{-2}, respectively. This small difference can be considered negligible since it falls within the calculated standard deviation, showing the material activation, although changes the particles sizes and agglomeration, it does not affect ECSA.

Moreover, the heterogeneous electron transfer rate constant (k°_{obs}) could be determined from the same measurements following the Nicholson method,[146] using equation bellow, where D is the diffusion coefficient (9.10×10^{-6} cm^2 s^{-1} for $[Ru(NH_3)_6]^{3+}$), α is assumed to correspond to 0.5, n is the number of electrons transferred in the electrochemical process (1 in this case), F is the Faraday constant, ν is the scan rate, R is the gas constant, T is the temperature and ΔE_p is the peak-to-peak separation. The reported values for CoFePBA and ACoFePBA are 0.20 ± 0.03 and 0.92 ± 0.00, respectively. This improvement in 4.6 times indicates that the material activation and cyanide vacancies creation can result in faster kinetics related to electron transfer.

$$\mathbf{k}^{\circ}_{obs} = \left[\mathbf{2.18}\left(\frac{D\alpha nF\nu}{RT}\right)^{\frac{1}{2}}\right] exp\left[-\left(\frac{\alpha^2 nF}{RT}\right)\Delta E_p\right]$$

Finally, the superficial concentration of electroactive Co^{2+} sites ($[Co]_{surf.}$) was obtained according to a method reported in the literature,[178] consisting in a CV measurement with scan rate of 0.1 V s^{-1} (**Figure 45 C** and **D**). The resulting CV is normalized by the ECSA and the area corresponding to the peak of the Co^{3+}/Co^{2+} reduction can be determined by the peak integration. Furthermore, since the reduction of Co^{3+} to Co^{2+} involves the transference of a single electron, the exact molar concentration of electroactive Co^{2+} sites can be determined according to the following equation, where A is the area of the redox process peak (V A cm^{-2}), S is the scan rate (V s^{-1}), e is the elementary charge (1.602×10^{-19}C) and NA is the Avogadro constant (6.022×10^{23} Mol^{-1}):

$$[Co]_{surf.} = \frac{A}{S\,.e\,.N_A}$$

The reported results show an increase in the ([Co]$_{surf.}$ sites for ACoFePBA, going from 4.07 ± 0.10 nmol for CoFePBA to 9.52 ± 0.77 nmol for ACoFePBA. This increase can be attributed to the creation of vacancies, resulting in the substitution of cyanide by water in some metallic sites. Thus, it is possible to state that the creation of vacancies affects the number of active sites in the material.

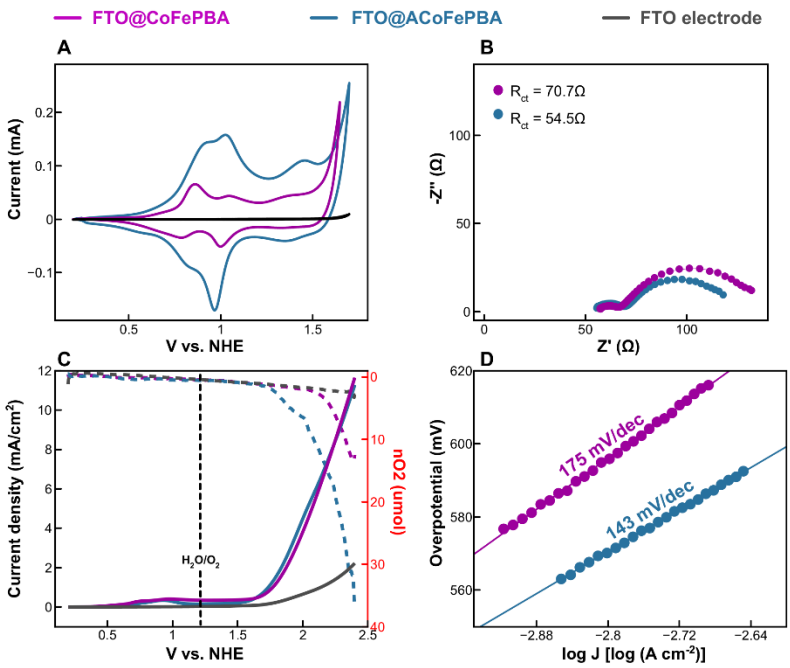

Figure 46. Electrochemical characterization on the FTO modified electrodes. CoFePBA (pink line), Activated CoFePBA (blue line) and bare FTO electrode (gray line). A) Cyclic voltammetry performed at 50 mV s^{-1} in 0.1 mol L^{-1} KNO_3 solution. B) Electrochemical Impedance Spectroscopy (EIS) performed at 1.7 V vs. NHE in 0.1 mol L^{-1} KNO_3 solution. Linear Sweep voltammetry (LSV) performed at 10 mV s^{-1} in 0.1 mol L^{-1} KNO_3 solution in the 3D printed SECM cell, with two working electrodes set up, operating in the SG/TC mode. Straight line represents the LSV on the WE1 and dashed line represents the O_2 reduction current on WE2. B) Tafel slopes for the catalysts.

Cyclic voltammetry was performed at 50 mV s^{-1} in 0.1 mol L^{-1} KNO_3 electrolyte to get a better understanding on the redox processes for both materials and the results are presented in **Figure 46 A**. CoFePBA (pink line) and ACoFePBA (blue line) cyclic voltammogram present similar shapes, with three main redox waves around 0.9, 1.03 and beyond 1.3 V (vs. NHE) that can be assigned to Fe^{2+}/Fe^{3+}, Co^{2+}/Co^{3+} and Co^{3+}/Co^{4+} oxidation process respectively, suggesting that they have similar structures.[4,83] However, some differences in the redox potentials can be observed by comparing both films and these changes can indicate a differences in the ACoFePBA structure, besides iron/cobalt species in a different chemical environments with the material activation. Moreover, we highlight the increase in the Co^{3+}/Co^{4+} oxidation potential when comparing

CoFePBA (1.37 V) and ACoFePBA (1.44 V). This increase in the redox potential can be related to the substitution of some cyanide by water molecules during the material activation, due to the fact that the replacement of the nitrogen from CN^- by a H_2O is reported to increase the redox potential of the cobalt center.[82]

Finally, electrochemical impedance spectroscopy (EIS) was conducted on the modified electrodes. **Figure 46 B** shows the Nyquist plot for the materials, characterized by two semi-circles, the first related to the substrate and the second to the material.[141] In this way, the electrochemical circuit consists in an uncompensated resistance (R_u), two different charge-transfer resistance (R_{ct}) in series, and two different constant phase element (CPE) in parallel connection with their respective R_{ct}, as shown in **Figure 47**. The obtained R_{ct} values shows that the creation of vacancies can enhance electron transference reactions within the material, being 70.7 and 54.5 Ω for CoFePBA and ACoFePBA respectively (**Figure 27 B**).

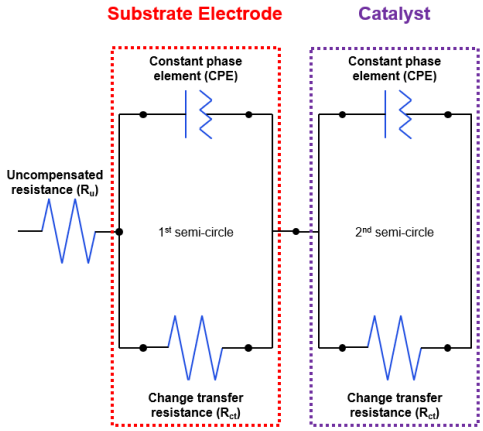

Figure 47. EIS equivalent electrochemical circuit.

4.3.2 Catalytic studies

Both CoFePBA and ACoFePBA films had their catalytic activity evaluated towards water oxidation reaction (WOR), and the experiments were performed on a 3D printed SECM cell. The use of the adapted cells, allows an arrangement with two working electrodes, making it possible the evaluation of the catalyst current densities evolution, along with an evaluation of the amount of O_2 being evolved during the potential application process, following the SECM substrate generation/tip collection (SG/TC) operation mode. The results are presented on **Figure 46 C** and

as it can be seen, both materials reach a similar current density (j), however the rate of O_2 evolution is different for both materials, with a higher production rate being reported by ACoFePBA. The similar current densities can be related to some side reactions for CoFePBA that are not related to OER, resulting in a lower faradaic efficiency for this material. When comparing the O_2 evolution rate, is possible to observe it starts earlier for ACoFePBA and besides, when comparing the amount of O_2 in the highest potentials (2.50 V), ACoFePBA produced 36.5 µmol of O_2, while CoFePBA produced only 13.2 µmol. Thus, this indicates that ACoFePBA produces almost 2.8 times more O_2 than the structure without defects, indicating better performance towards the OER with the creation of cyanide vacancies in the structure. Moreover, the Tafel plot (**Figure 46 D**) shows that the Tafel slope decreases from 175 mV dec^{-1} for CoFePBA to 143 mV dec^{-1} for the ACoFePBA. This difference, although small, indicated faster kinetics for ACoFePBA and maybe some differences in the rate-determining step in the reaction mechanism, indicating that the material activation and vacancies formation can improve their performance and improve their kinetics towards OER. Besides, this performance enhancement can also be related to the improvement in the number of surface active Co^{2+} sites, that are probably exposed and coordinated to water instead of cyanide, due to the material activation process.

Table 10. Oxygen evolution quantification at η = 400mV for both catalysts.

	O_2 current (A)	**O_2 mol**	**O_2 µmol (± 0.45)**
CoFePBA	-1.79_x10^{-5}	5.89_x10^{-6}	5.89
ACoFePBA	-2.10_x10^{-5}	8.02_x10^{-6}	8.02

Furthermore, the oxygen evolution was studied at a fixed potential with the aim of obtaining a more accurate quantification of O_2 for both catalysts. The results are presented in **Table 10**. The amount of evolved O_2 related to the current was obtained according to a calibration with the dissolved oxygen (DO) sensor, Hanna instrument, as described in our recent publication reproduced on Chapter III.[4] It is important to highlight that the O_2 measurements were carried out three times to obtain a more accurate result, with a standard deviation value, thus the reported results are an average of the measurements. The reported results at η = 400mV are 5.89 and 8.02 ± 0.45 µmol for CoFePBA and ACoFePBA respectively. It is possible to observe that the material activation and vacancies formation can increase the oxygen evolution by approximately 35%,

indicating that the number of vacant active sites is directly related to the catalyst performance enhancement. Moreover, when comparing the previous results obtained by the Activated Prussian Blue, with only iron atoms, the overpotential is decreased, since with APB we were only able to quantify O_2 with a η = 500mV. Besides, the oxygen evolution is higher for analogue with Co, indicating cobalt is playing a crucial role as the active site.

Finally, stability tests were also carried out to understand the catalyst's activity and performance operating under WOR conditions (η = 600mV) during 16 hours of electrolysis and the results are presented in **Figure 48**. The results show that although both current densities decrease after 16 hours under reaction, both catalysts present a relatively good stability. Nonetheless, ACoFePBA presents a more consistent current evolution, and its j does not change much during the whole process, as it is observed for the traditional material, indicating the material activation can be responsible for providing a better stability for the structure under WOR conditions. The slightly higher j achieved by CoFePBA is in accordance with the observed results for LSV and can indicate some side reaction taking place and a lower faradaic efficiency for this material. Therefore, this suggests that the creation of cyanide vacancies, besides improving the O_2 evolution for the catalyst, can also make it more selective towards the WOR.

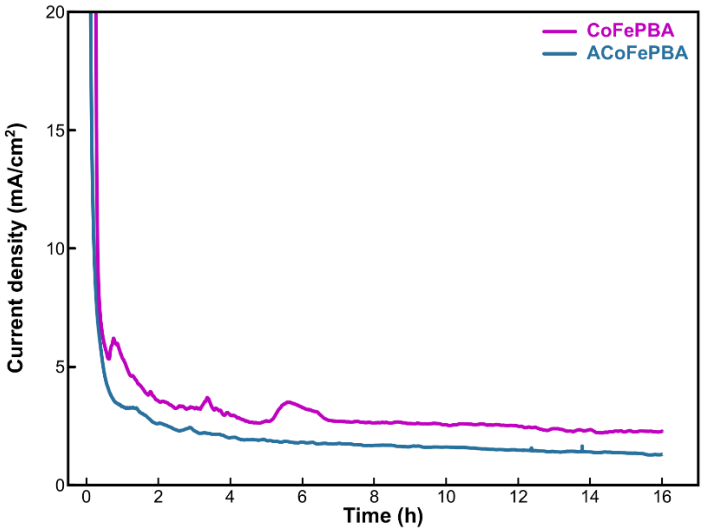

Figure 48. Stability test performed at η = 600mV in 0.1 mol L^{-1} KNO_3 solution for 16 hours for both catalysts. CoFePBA (pink line) and ACoFePBA (blue line).

The catalysts were evaluated after the stability test to obtain information about the materials structure and understand if there were any changes after the catalysis. Firstly, SEM was carried out

to see if the catalysis brought any change in the material morphology, shape and distribution over the electrode. The results are presented in **Figure 49**. As it is shown, there are no big changes for the particles size and distribution after the catalysis, being similar to the information obtained from the analysis with the as prepared materials, presented in **Figure 43**. Furthermore, it is possible to observe a lower amount of material spread over the electrode, with a higher appearance of the FTO substrate. This can be related to some lixiviation that can happen during the reaction, due to some areas with a lower stability and can be the possible reason for the current decreasing during the stability tests. Nonetheless, although there us some material lixiviation, some active material is still deposited over the electrode and it can keep operating with a good current density.

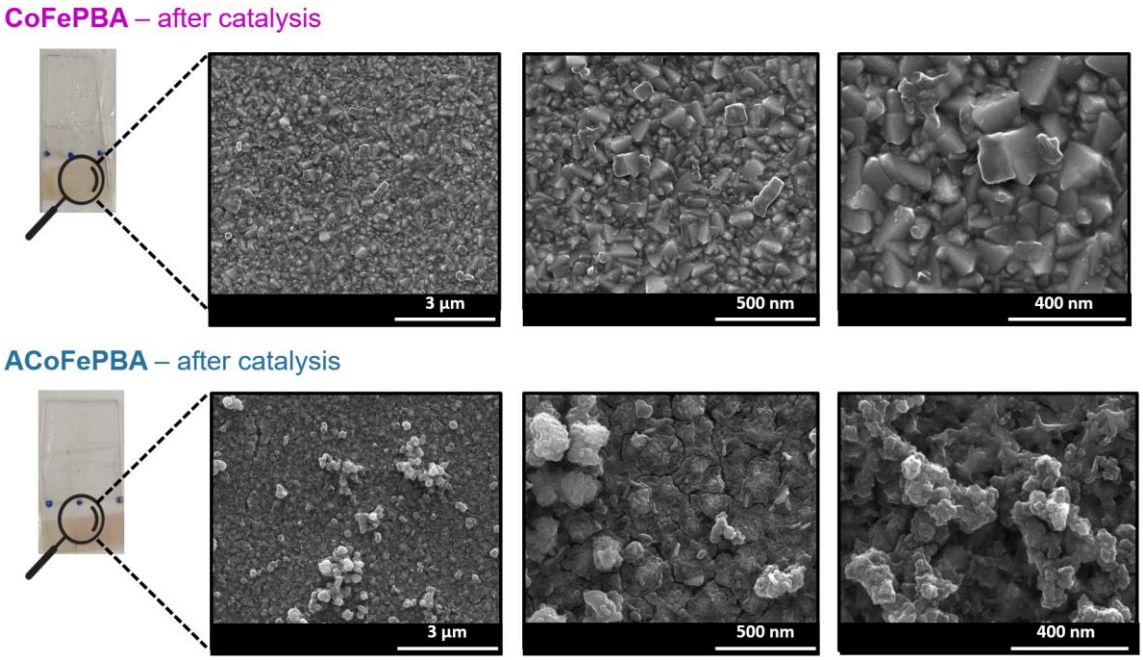

Figure 49. Scanning Electron Microscopy (SEM) of the catalysts after the stability test (after catalysis).

Moreover, Raman spectroscopy and X-ray photoelectron spectroscopy (XPS) were carried out after the stability tests aiming to get information about possible structural changes after 16h operating under WOR conditions. Raman spectrum comparing the films before and after the catalysis can be seen in **Figure 50 A**. For both materials before and after the catalysis it is possible to identify two main bands assigned to the A_{1g} and E_g mode of ν(CN) stretching vibration.[4,125,175,176] The presence of these bands in the materials after the catalysis indicates that the general PBA framework was kept with the reaction and no side product catalyst was formed. Moreover, when comparing CoFePBA spectrums before and after, it is possible to observe a shift from 2130 to 2140

cm^{-1} after the catalysis, indicating the reaction promotes an oxidation on the metallic sites that is irreversible even when the reaction stops. The active sites are expected to go to higher oxidation states during the reaction, due to the high applied potential, and the results suggest that not all of the metallic sites come back to the as prepared oxidation state. Furthermore, for the ACoFePBA after catalysis spectrum it is possible to identify the appearance of a shoulder band around 2166 cm^{-1}, meanwhile the main E_g and A_{1g} modes of ν(CN) remain unchanged. This suggests a different species with a higher oxidation state being formed with the high potential application during WOR, not going back to the original reduced states. Thus, the Raman results indicate that the PBA structure is maintained after the catalysis, although some metallic oxidation states are irreversibly changed.

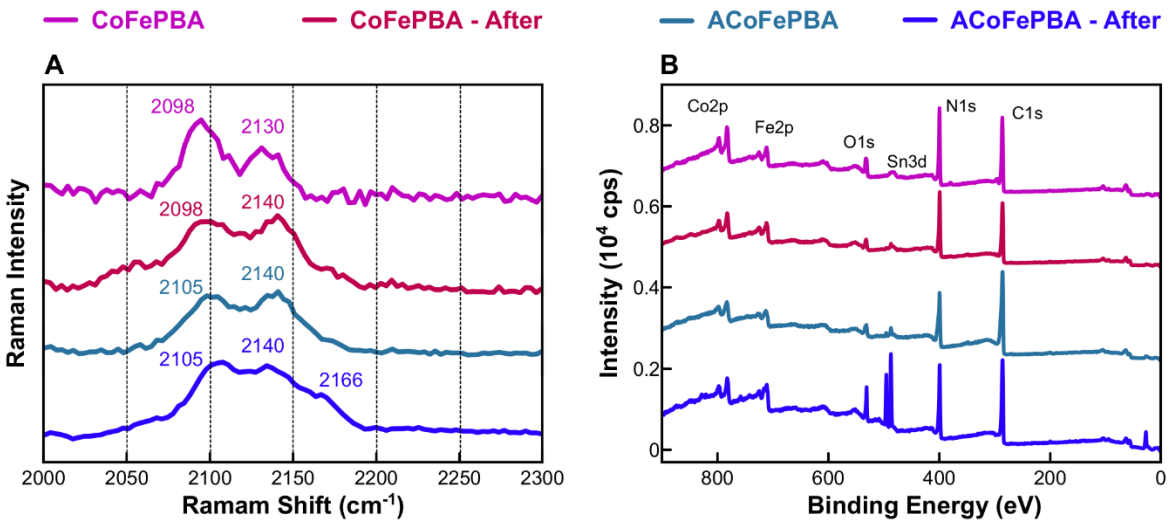

Figure 50. Spectroscopy studies carried out after stability tests. CoFePBA (pink line), CoFePBA-After (red line), ACoFePBA (light blue line) and ACoFePBA-After (dark blue line). A) Raman spectra obtained using a 785 nm laser excitation for the modified FTO electrodes to study the materials ν(CN) stretching vibration. B) XPS survey spectra with main peaks assigned to their respective elements and transitions.

Finally, qualitative XPS measurements were carried out after the stability tests aiming to understand possible changes in the catalysts after the catalysis took place for 16h and the results are shown in **Figure 50 B**. The analysis shows the same general elemental composition, before and after the catalysis for both catalysts, identifying Co 2p (782 eV), Fe 2p (708 eV), O 1s (531 eV), Sn 3d (485 eV), N 1s (397 eV) and C 1s (284 eV). The presence of Sn can be related to the FTO glass substrate composition. Besides, some changes in intensity of the Sn composition can be observed especially for ACoFePBA after the catalysis and can indicate a higher film lixiviation that does not drastically alter the catalytic activity.

Therefore, these results suggests that although bringing some changes in the catalysts oxidation states, no big structural changes can be observed, indicating the main PBA framework is maintained through the whole process and is the main responsible for the O_2 evolution, without any catalyst by-product (like an oxide) being formed.

4.3.3 LA-ICP-MS

Laser ablation inductively coupled plasma mass spectrometry (LA-ICP-MS)[101,147,148] analysis were used to obtain some information about the elemental (Fe and C) distribution over the thin film, to understand its homogeneity. Furthermore, the results also helped to obtain some insights on the Fe/C in an attempt to confirm the vacancies formation. The Co information could not be obtained from this analysis, because the metallic cobalt film was not completely oxidized during the PBA formation, and thus, the Co composition was higher and out of the detectable limit by the equipment. Nonetheless, we believe the changes in the Fe/C ratio could be further related to Co/C ratio as well, since the CN^- vacancies are introduced between the Co and Fe in the Co-CN-Fe proposed structure. The analyses were carried out on a titanium electrode to avoid the presence of any other element that could interfere with the results and elemental identification. The same FTO deposition paraments described in the experimental data were used for the deposition on the Ti electrode.

The results can be seen in **Figure 51** and **Figure 52** and it indicated a good film distribution over the substrate. It is possible to see Fe and C are widely spread over the whole probed area and suggests a good film deposition and homogeneity. Moreover, the differences in the Fe intensities when comparing both films can be related to the differences in the materials deposition that can result in a higher concentration of the deposited film depending on the chosen methodology.

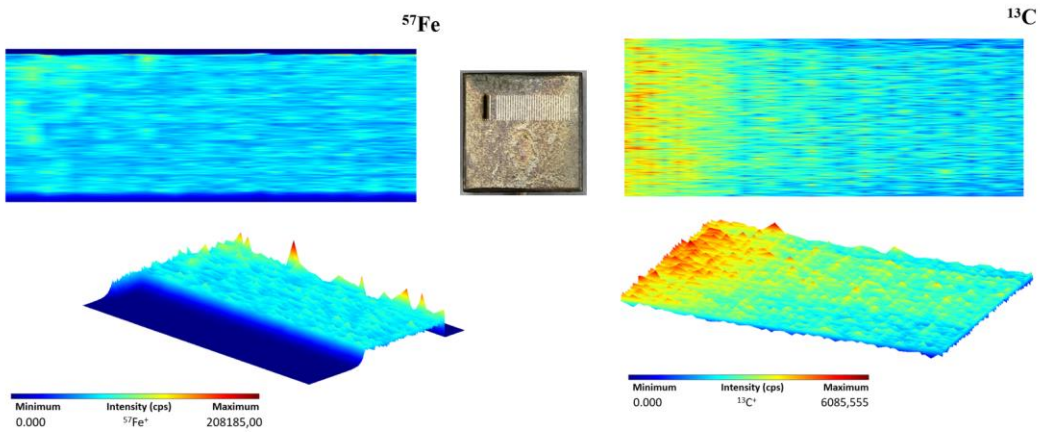

Figure 51. LA-ICP-MS qualitative mapping for Fe and C on CoFePBA film. Inset represents the modified picture with the scan area highlighted.

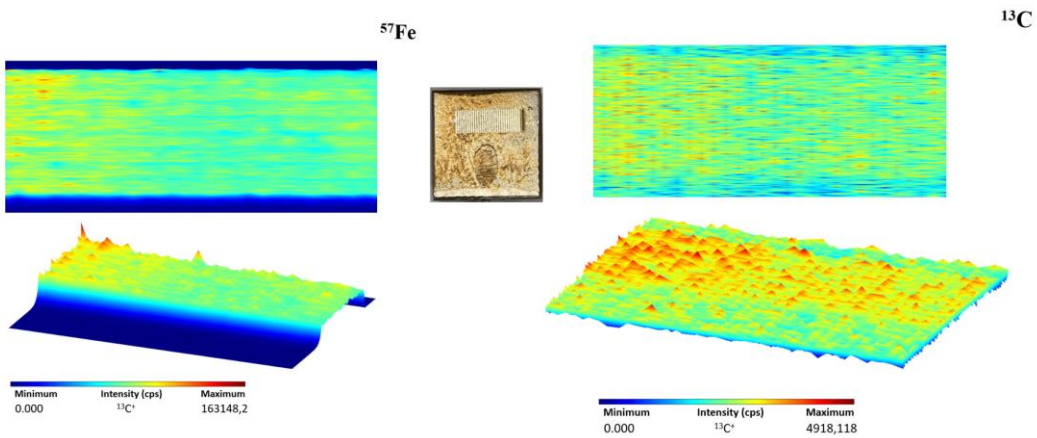

Figure 52. LA-ICP-MS qualitative mapping for Fe and C on ACoFePBA film. Inset represents the modified picture with the scan area highlighted.

Finally, these results were used to obtain the ration between Fe/C in both films as an attempt to identify and confirm the formation of cyanide vacancies in the activated catalyst film (ACoFePBA). This approach was used with the belief that the film activation would form electrochemically designed CN^- vacancies, removing CN^- from the structure and therefore increasing the ration between Fe and C. A 3D mapping on the Fe/C qualitative ratio intensity for both films can be seen in **Figure 53**. As it is shown, CoFePBA has a Fe/C ratio of 16.80, while ACoFePBA has a ratio of 21.20. The nominal ratio for CoFePBA is approximately 6 times higher than previously reported for the traditional Prussian blue (2.70)[4], since CoFePBA is known to have more conventional vacancies in its structure to ensure the electro-neutrality of the network.[82]

These results show ACoFePBA has a Fe/C ratio 1.30 times higher than CoFePBA, indicating carbon is probably leaving the structure in the form of CN^- during the material activation

and synthesis. This confirms that ACoFePBA has 30% more cyanide vacancies than the traditional reported CoFePBA and this is related to the enhancement of the catalytic activity and O_2 evolution. Furthermore, it is worth noting that an increase in 30% on the Fe/C ratio for the activated material, indicating 30% more vacant sites in ACoFePBA, resulted in an enhancement of 35% in the O_2 evolution (**Table 10**) for this catalyst when comparing to CoFePBA. Therefore, it is possible to conclude that the creation of vacancies and the formation of these free active sites explain and is directly related to an enhancement in the performance and activity of these catalysts towards the water oxidation reaction. Hence, defects and vacancies design are a great approach to overcome the low concentration of active sites on PBAs and improve their catalytic activity.

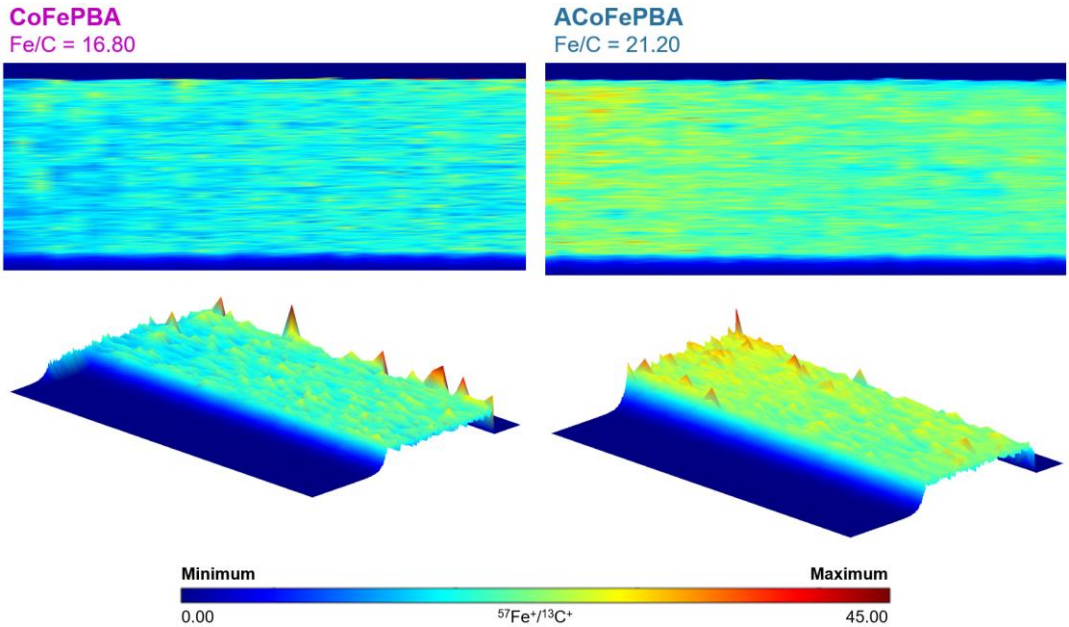

Figure 53. Laser ablation inductively coupled plasma mass spectrometry (LA-ICP-MS) qualitative mapping to obtain the ratio between Fe/C in the CoFePBA and ACoFePBA films.

4.3.4 Synchrotron-based soft X-ray spectroscopy

Synchrotron-based soft X-ray Photoelectron Spectroscopy (XPS), performed at IPÊ beamline of the synchrotron light source Sirius, was used to probe the surface composition and Co and Fe speciation of the films. The survey plot from 1200 to 0 eV is presented in **Figure 54 A**, and the analysis shows the same general elemental composition for both films, identifying Co 2p (782

eV), Fe 2p (708 eV), O 1s (531 eV), Sn 3d (485 eV), N 1s (397 eV) and C 1s (284 eV). The presence of the Sn signal can be related to the substrate used as the electrode (FTO - fluorine doped tin oxide coated glass), having Sn in its composition. The similar elemental composition for both films confirm the same structure obtained even after the creation of vacancies for ACoFePBA. Furthermore, Fe 2p and Co 2p separate spectrum was obtained with the same kinetic energy for Co and Fe speciation and the plots can be seen on **Figure 54 B** and **C**. A few differences can be observed when comparing both materials and can indicate differences in the oxidation states for the materials. However, due to some positive charge building up over the surface, a high-resolution spectrum could not be obtained for the materials, and further speciation studies were made using high resolution XAS. Finally, quantitative XPS analysis provided some information about Co, Fe and N composition over the films surface. The surface Fe/Co ratio is very similar for both materials, being 1:1 for CoFePBA and 1.3:1 for ACoFePBA, indicating a very similar metallic structure for both materials. Further Matal/N ratio studies show an increase in from 2:1 for CoFePBA to 3:1 for ACoFePBA, suggesting that nitrogen is being lost with the material activation, possibly related to the CN^- vacancies formation. These results agree with the previous LA-ICP-MS reports and the activation represents 50% more vacancies than the traditional analogue (CoFePBA). This difference in the ratio increasement between XPS (50%) and LA-ICP-MS (30%) is related to XPS being a surface sensitive technique, while with LA-ICP-MS it is possible to obtain deeper analysis and the results represent an average of whole film composition.[147,179] Nonetheless, quantitative XPS analysis provides more evidence of the creation of cyanide vacancies com ACoFePBA and how this is associated to the catalytic activity enhancement.

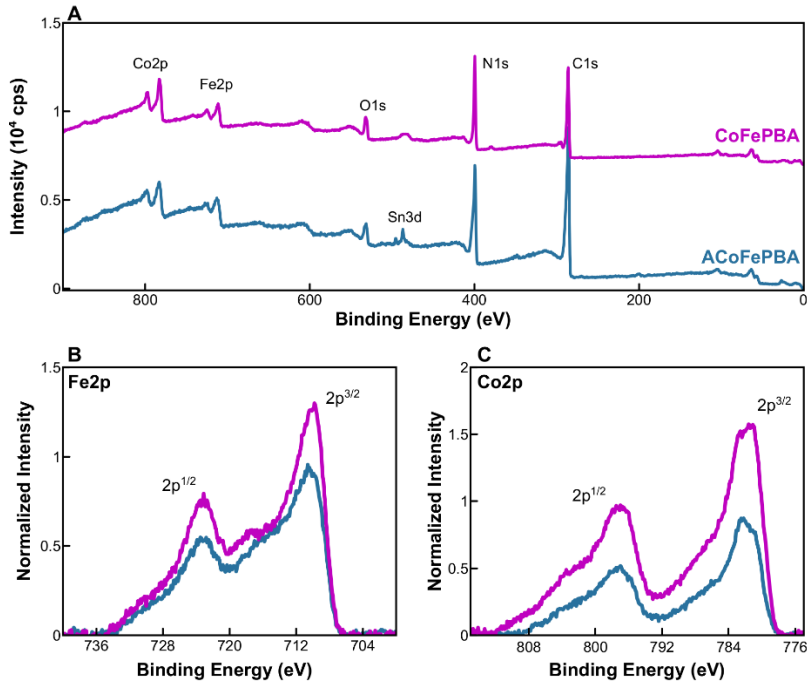

Figure 54. Synchrotron based soft X-ray photoelectron spectroscopy for CoFePBA (pink line) and ACoFePBA (blue line). A) XPS survey spectra with main peaks assigned to their respective elements and transitions. B) Fe 2P spectra. C) Co 2P spectra.

Moreover, synchrotron-based soft X-ray absorption Spectroscopy (XAS), performed at IPÊ beamline of the synchrotron light source Sirius, was used to probe the materials' ligand field structure, defects, and Co/Fe speciation. The analysis were carried out using two different detection methods, a more surface sensitive method, Total Electron Yield (TEY), and a bulk sensitive method, Fluorescence Yield (FY).[173,180,181] The Co and Fe L-edge spectrums are shown in **Figure 55**. The Co^{2+}/Co^{3+} and Fe^{2+}/Fe^{3+} speciation can be also observed in the figure and it was made according to the literature, using some previous XAS analysis carried out on Prussian Blue and its analogues which also base their results and discussion in some spectrum simulations.[4,81,82,171,182,183]

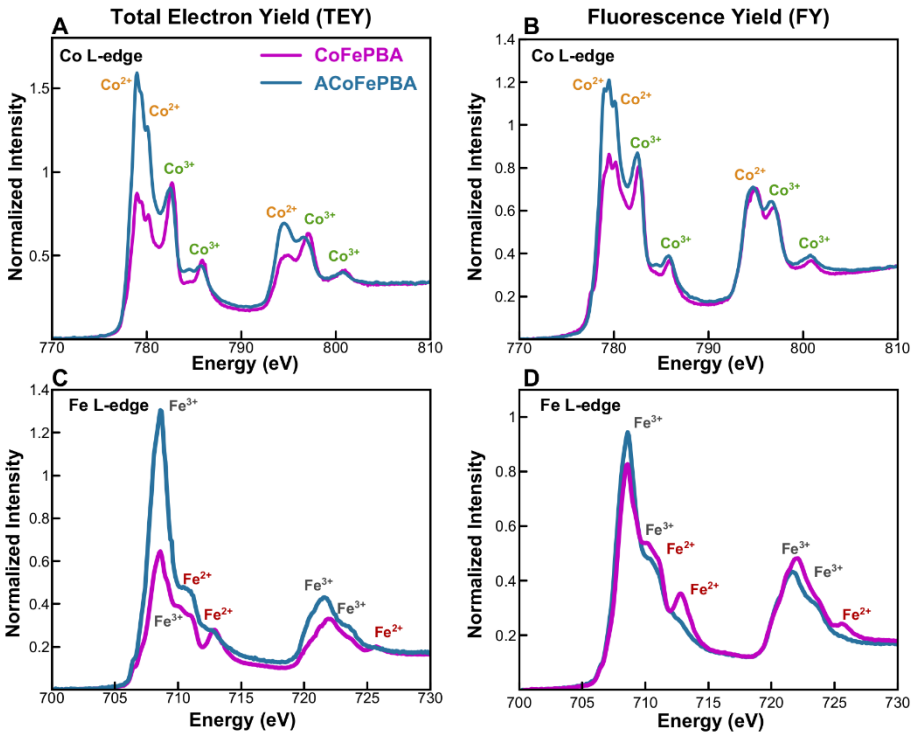

Figure 55. Synchrotron based soft X-ray absorption spectroscopy for CoFePBA (pink line) and ACoFePBA (blue line). A) Co L-edge TEY XAS spectra. B) Co L-edge FY XAS spectra. C) Fe L-edge TEY XAS spectra. D) Fe L-edge FY XAS spectra.

By comparing TEY and FY analysis, it is possible to observe small but existing differences in the spectrum for the Co and Fe L-egdes, especially when comparing the Co^{2+} and Fe^{3+} composition. This can suggest small differences between the surface and the bulk for both materials. When comparing the TEY results between both CoFePBA and ACoFePBA it is observed that before the creation of defects (CoFePBA), the ratio between Co^{2+}/Co^{3+} obtained from the Co L_3-edges (**Figure 55 A**) absorption peaks (779 eV for Co^{2+} and 782.7 eV for Co^{3+}) is around 1:1, being a very balanced mixed valance material. However, the creation of defects has resulted in the increasing of the amount of Co^{2+} composition in the ACoFePBA, taking this ratio up to around 2:1. This agrees to the increase in the superficial concentration of electroactive Co^{2+} sites previously described and supports the literature mechanism proposals that Co^{2+} are the active sites for WOR in the CoFePBA catalyst, since the creation of vacancies and predominance of Co^{2+} on the structure resulted in an enhancement of the catalytic activity.[69,83,84] Furthermore, the ratio between Fe^{3+} and Fe^{2+} obtained from the Fe L_3-edges (**Figure 55 B**) absorption peaks (708.7 eV for Fe^{3+} and 713 eV for Fe^{2+}) is around 2:1 for CoFePBA and after the creation of defects, the structure becomes predominantly in Fe^{3+}, since the absorption

peaks assigned to Fe^{2+} practically disappeared (713 and 725.8 eV) for ACoFePBA. These results agree with the Raman previously mentioned results and can indicate that the activation process, linked with the formation of cyanide vacancies, can modulate the metals oxidation states as a way to introduce neutrality in the structure. Thus, this modulation can also favour a specific oxidation state (in this case Co^{2+}/Fe^{3+}) that facilitates and results in an enhancement of the catalytic activity. Finally, by analyzing the absorption peaks energy it is possible to observe that the spectrum for ACoFePBA is shifted in 0.2 and 0.4 eV toward lower energies when compared to the CoFePBA spectra, indicating changes in the ligand-field structure that are possibly linked some CN^- left the structure and was replaced by H_2O, supporting and giving spectroscopic evidence for our vacancy formation mechanism.[4,171] Thus, explaining how the design of cyanide vacancies in the ACoFePBA can improve its performance towards WOR and the amount of O_2 evolved.

4.4 Conclusion

In conclusion, we presented the application of an electrochemical method to create cyanide vacancies on a CoFe Prussian blue analogue catalyst. The activated material showed an enhancement on its catalytic performance towards the oxygen evolution reaction. The creation of these defects improved the number of superficial Co^{2+} sites, that are probably the active sites for the reaction. Using LA-ICP-MS we were able to quantify an increase of 30% in the number of CN^- defects that resulted in an increase of 35% in the amount of evolved O_2. Finally, soft X-ray spectroscopy was used to probe these vacancies and shows that it can modulate the catalyst oxidation state and favors more active species, which is related to the catalytic activity enhancement. Thus, this easy method presents itself as a great and simple way to improve the number of active sites in earth abundant catalyst and the unique sensitivity of soft x-ray spectroscopy might break the complexity of defect chemistry on earth-abundant catalysts recently exploited for catalysis and energy conversion.

4.5 Acknowledgments

The authors are grateful for the financial support of Brazilian Funding Agencies. This study was financed in part by the Coordenação de Aperfeiçoamento de Pessoal de Nível Superior - Brasil

(CAPES) - Finance Code 001, Conselho Nacional de Desenvolvimento Científico e Tecnológico CNPq (grant#141020/2022-9 and grant#140809/2021-0) and Fundação de Amparo à Pesquisa do Estado de São Paulo, FAPESP (grant#2014/50867-3, grant#2017/11986-5, grant#2017/50085-3, grant#2018/25092-9, grant#2018/25207-0, grant#2019/00063-9, grant#2019/2445-8, grant#2021/05976-2, 2022/04739-0). This research used facilities of the Brazilian Synchrotron Light Laboratory (LNLS), part of the Brazilian Center for Research in Energy and Materials (CNPEM), a private non-profit organization under the supervision of the Brazilian Ministry for Science, Technology, and Innovations (MCTI). The IPE beamline staff is acknowledged for the assistance during the experiments 20221791.

Chapter V

Conclusion and Perspectives

In Chapter V, the main overview and conclusion from this research is presented. By the end, some of the perspectives for future research are discussed.

5.1 Addressal of objectives

In Chapter I, the main objectives of this research were presented and are listed below:

i. Propose a methodology to quantify iron for some iron-based catalysts thin films.
ii. Propose a strategy to overcome the PBA-based catalysts' main shortcoming of having low concentration of active sites.
iii. Investigate the active sites in Prussian Blue analogue catalysts, understanding how they work and the factors that influence their activity and performance towards OER.
iv. Investigate synchrotron-based soft X-ray spectroscopy techniques to probe the structure of PBAs and identify changes in the electronic configuration.

Here are presented as a summary how this thesis addressed each of the objectives set in Chapter I:

i. A photochemical pre-treatment was proposed for the quantification of the total iron from heterogeneous thin films composed of iron-based materials. The photochemical approach (with UV-light) is used to ensure a full dissociation of iron ions before the quantification, to allow its coordination with 1,10-phenanthroline and a further spectroscopic quantification. This method has been revealed to be highly effective and precise, and has been shown to have a wide range of applications for different iron-based catalysts.

ii. This thesis presents an alternative methodology to synthesize the Prussian blue, obtaining a catalyst with vacancies created by an electrochemical method. The methodology was applied for Traditional Prussian Blue (TPB) and its analogue, CoFePBA. Both modified catalysts were shown to have an enhanced catalytic performance towards WOR and a higher concentration of active sites.

iii. The vacancies and active sites were probed by spectroscopic method using pyridine as a molecular probe, electrochemical CV-based methods and by using laser ablation inductively coupled plasma mass spectrometry (LA-ICP-MS). The analysis showed the active sites to be Fe^{2+} vacant sites (for TPB) and Co^{2+} for CoFePBA. Furthermore, they were able to identify an increase in CN^- defects with the material defects by probing Fe/C ratio. The increase of this ratio is directly proportional to the enhancement of oxygen evolution.

iv. Synchrotron-based soft X-ray spectroscopy was carried at the IPE beamline of Sirius at the Brazilian Synchrotron Light Laboratory and provided spectroscopic evidence of the creation of vacancies and changes in the ligand-field. Besides, the analysis also provided information about the metallic oxidation states and how the presence of CN^- vacancies influenced these configurations.

PBA materials serve as excellent catalyst alternatives for oxygen evolution reactions (OER), particularly due to their ability to operate under mild conditions, exhibit high stability, and maintain great activity. Research on these materials offers a significant opportunity to replace noble metal-based catalysts. Therefore, this thesis proposal, involving the creation of cyanide vacancies within these materials, represents a promising approach to increase the number of active sites within their structures and enhance their overall catalytic activity.

Furthermore, the electrochemical method is a cost-effective, rapid, straightforward, and readily accessible approach that has demonstrated its effectiveness in generating vacancies within these materials. This further underscores the advantages of employing this technique, which has the potential to elevate the significance of PBA in the field of OER research.

Finally, the use of synchrotron-based soft X-ray spectroscopy, a well-established element-specific technique, proves invaluable for investigating the composition of materials, discerning distinct valence states within elements, and gaining valuable insights into electronic states. We have

empirically harnessed its unique sensitivity to probe vacancies within these materials. This technique has demonstrated its suitability for such investigations, enabling the identification of changes in the material's electronic structure, alterations in the ligand field, and modulation of oxidation states upon the creation of vacancies. As a result, it provides spectroscopic evidence regarding the nature of active sites within these structures and offers valuable insights into the challenging task of elucidating reaction mechanisms in the field of PBA research.

5.2 Research perspectives

The perspective for future research from this thesis is presented in the form of questions to left to be answered:

i. What is the vacancies creation mechanism? Is there any change in the method that would favor their formation?

ii. Is it possible to use this methodology for defects creation to activate other PBAs such as CoCoPBA, CuFePBA, NiFePBA or even RuFePBA? Can the catalytic activity be enhanced in the same way?

iii. The creation of cyanide vacancies changes the reaction mechanism and the rate-determining step?

iv. What is the real active site for the structure before and after the activation? What is the oxidation state reached during the reaction?

v. Can synchrotron-based hard X-ray spectroscopy (XANES/EXAFS) be used to probe and identify changes in the coordination number and ligand-field, indicating the creation of these vacancies?

To address these perspectives future spectroscopic *in situ* studies are required, including Raman, FTIR, UV-Vis and even synchrotron-based spectroscopic techniques. These studies can give the necessary evidence for the reaction mechanism proposal, active sites suggestion, the metallic oxidation states during the reaction, the rate-determining step and even further information about the nature of defects and how their presence influence the reaction mechanism.

Nevertheless, this thesis presents a very relevant work for the research about Prussian Blue analogues-based catalysts, providing evidence of how the creation of vacancies can increase the

number of active sites and consequently enhance their catalytic activity, which is a massive challenge in the area. Furthermore, the TPB has never been shown to act as a good catalyst towards WOR due to the low number of active sites, and our first report of this material being activated and reaching outstanding activity is evidence of how important these vacancies can be. The use of this vacancies for the CoFePBA-based catalyst showed how versatile the methodology is and the material also presented an enhancement in the activity.

Finally, most of vacancies creation proposals in the literature are based on extreme conditions of pH and temperature, with some of them being based on the use of high energy plasma lasers. Meanwhile, the method proposed by this thesis is very simple, cheap and easy to achieve, besides proving to be very efficient. Therefore, it can be a great opportunity to study other PBA with those electrochemically formed vacancies.

Bibliography

1. Germscheidt, R. L. *et al.* Hydrogen Environmental Benefits Depend on the Way of Production: An Overview of the Main Processes Production and Challenges by 2050. *Advanced Energy and Sustainability Research* **2**, 2100093 (2021).
2. Von Zuben, T. *et al.* Is Hydrogen Indispensable for a Sustainable World? A Review of H2 Applications and Perspectives for the Next Years. *J. Braz. Chem. Soc.* (2022) doi:10.21577/0103-5053.20220026.
3. Germscheidt, R., Morais, C., Francischini, D., Arruda, M. A. & Bonacin, J. Photochemical Pre-Treatment to Quantify Iron in Thin Films. *J. Braz. Chem. Soc.* (2023) doi:10.21577/0103-5053.20230008.
4. Germscheidt, R. L. *et al.* Water Oxidation Performance Enhanced by Electrochemically Designed Vacancies on a Prussian Blue Catalyst. *ACS Appl. Energy Mater.* **5**, 9447–9454 (2022).
5. Williams, Q. & Hemley, R. J. Hydrogen in the Deep Earth. *Annu. Rev. Earth Planet. Sci.* **29**, 365–418 (2001).
6. Planet hydrogen - Hydrogen. *Air Liquide Energies* https://energies.airliquide.com/resources/planet-hydrogen-hydrogen (2017).
7. Abdin, Z. *et al.* Hydrogen as an energy vector. *Renewable and Sustainable Energy Reviews* **120**, 109620 (2020).
8. Abdalla, A. M. *et al.* Hydrogen production, storage, transportation and key challenges with applications: A review. *Energy Conversion and Management* **165**, 602–627 (2018).
9. What Is the Sun Made Of? | Space. https://www.space.com/17170-what-is-the-sun-made-of.html.
10. Bockris, J. O. M. The hydrogen economy: Its history. *International Journal of Hydrogen Energy* **38**, 2579–2588 (2013).
11. Hydrogen - Fuels & Technologies. *IEA* https://www.iea.org/fuels-and-technologies/hydrogen.
12. Widera, B. Renewable hydrogen implementations for combined energy storage, transportation and stationary applications. *Thermal Science and Engineering Progress* **16**, 100460 (2020).
13. Hydrogen Applications | Hydrogen. https://hydrogeneurope.eu/hydrogen-applications.
14. *Hydrogen fuel: production, transport, and storage*. (CRC Press, 2009).
15. Fayaz, H. *et al.* An overview of hydrogen as a vehicle fuel. *Renewable and Sustainable Energy Reviews* **16**, 5511–5528 (2012).
16. Germscheidt, R. L. *et al.* Hydrogen Environmental Benefits Depend on the Way of Production: An Overview of the Main Processes Production and Challenges by 2050. *Adv Energy Sustain Res* 2100093 (2021) doi:10.1002/aesr.202100093.
17. International Energy Agency. *The Future of Hydrogen: Seizing today's opportunities*. 203 https://www.oecd-ilibrary.org/energy/the-future-of-hydrogen_1e0514c4-en (2019) doi:10.1787/1e0514c4-en.
18. Gregory, D. P., Ng, D. Y. C. & Long, G. M. The Hydrogen Economy. in *Electrochemistry of Cleaner Environments* (ed. Bockris, J. O.) 226–280 (Springer US, 1972). doi:10.1007/978-1-4684-1950-4_8.

19. Hydrogen in Latin America – Analysis - IEA. https://www.iea.org/reports/hydrogen-in-latin-america.
20. Hosseini, S. E. & Wahid, M. A. Hydrogen production from renewable and sustainable energy resources: Promising green energy carrier for clean development. *Renewable and Sustainable Energy Reviews* **57**, 850–866 (2016).
21. Abe, J. O., Popoola, A. P. I., Ajenifuja, E. & Popoola, O. M. Hydrogen energy, economy and storage: Review and recommendation. *International Journal of Hydrogen Energy* **44**, 15072–15086 (2019).
22. Dawood, F., Anda, M. & Shafiullah, G. M. Hydrogen production for energy: An overview. *International Journal of Hydrogen Energy* **45**, 3847–3869 (2020).
23. Acar, C. & Dincer, I. Review and evaluation of hydrogen production options for better environment. *Journal of Cleaner Production* **218**, 835–849 (2019).
24. Noussan, M., Raimondi, P. P., Scita, R. & Hafner, M. The Role of Green and Blue Hydrogen in the Energy Transition—A Technological and Geopolitical Perspective. *Sustainability* **13**, 298 (2021).
25. Newborough, M. & Cooley, G. Developments in the global hydrogen market: The spectrum of hydrogen colours. *Fuel Cells Bulletin* **2020**, 16–22 (2020).
26. 50 shades of (grey and blue and green) hydrogen. *Energy Cities* https://energy-cities.eu/50-shades-of-grey-and-blue-and-green-hydrogen/ (2020).
27. Boretti, A. White is the color of hydrogen from concentrated solar energy and thermochemical water splitting cycles. *International Journal of Hydrogen Energy* (2021) doi:10.1016/j.ijhydene.2021.03.178.
28. Landing page (RECU eng) – Recupera. http://www.recupera.si/eng/.
29. Ahmed, A., Al-Amin, A. Q., Ambrose, A. F. & Saidur, R. Hydrogen fuel and transport system: A sustainable and environmental future. *International Journal of Hydrogen Energy* **41**, 1369–1380 (2016).
30. Abdin, Z. *et al.* Hydrogen as an energy vector. *Renewable and Sustainable Energy Reviews* **120**, 109620 (2020).
31. Nikolaidis, P. & Poullikkas, A. A comparative overview of hydrogen production processes. *Renewable and Sustainable Energy Reviews* **67**, 597–611 (2017).
32. Craig, M. J. *et al.* Universal scaling relations for the rational design of molecular water oxidation catalysts with near-zero overpotential. *Nature Communications* **10**, 4993 (2019).
33. McCrory, C. C. L. *et al.* Benchmarking Hydrogen Evolving Reaction and Oxygen Evolving Reaction Electrocatalysts for Solar Water Splitting Devices. *J. Am. Chem. Soc.* **137**, 4347–4357 (2015).
34. Hosseini, S. E. & Wahid, M. A. Hydrogen production from renewable and sustainable energy resources: Promising green energy carrier for clean development. *Renewable and Sustainable Energy Reviews* **57**, 850–866 (2016).
35. Pires, B. M. *et al.* Electrochemical water oxidation by cobalt-Prussian blue coordination polymer and theoretical studies of the electronic structure of the active species. *Dalton Trans.* **48**, 4811–4822 (2019).
36. Zambiazi, P. J. *et al.* Electrocatalytic water oxidation reaction promoted by cobalt-Prussian blue and its thermal decomposition product under mild conditions. *Dalton Trans.* **49**, 16488–16497 (2020).
37. Greeley, J. & Markovic, N. M. The road from animal electricity to green energy: combining experiment and theory in electrocatalysis. *Energy Environ. Sci.* **5**, 9246–9256 (2012).

38. Suen, N.-T. *et al.* Electrocatalysis for the oxygen evolution reaction: recent development and future perspectives. *Chem. Soc. Rev.* **46**, 337–365 (2017).
39. Schmidt, O. *et al.* Future cost and performance of water electrolysis: An expert elicitation study. *International Journal of Hydrogen Energy* **42**, 30470–30492 (2017).
40. Luca Bertuccioli (E4tech), Alvin Chan (Element Energy) David Hart (E4tech), Franz Lehner (E4tech), & Ben Madden (Element Energy) Eleanor Standen (Element Energy). *Study on development of water electrolysis in the EU*. https://www.fch.europa.eu/sites/default/files/study%20electrolyser_0-Logos_0_0.pdf (2014).
41. Shiva Kumar, S. & Himabindu, V. Hydrogen production by PEM water electrolysis – A review. *Materials Science for Energy Technologies* **2**, 442–454 (2019).
42. Barco-Burgos, J., Eicker, U., Saldaña-Robles, N., Saldaña-Robles, A. L. & Alcántar-Camarena, V. Thermal characterization of an alkaline electrolysis cell for hydrogen production at atmospheric pressure. *Fuel* **276**, 117910 (2020).
43. David, M., Ocampo-Martínez, C. & Sánchez-Peña, R. Advances in alkaline water electrolyzers: A review. *Journal of Energy Storage* **23**, 392–403 (2019).
44. Zeng, K. & Zhang, D. Recent progress in alkaline water electrolysis for hydrogen production and applications. *Progress in Energy and Combustion Science* **36**, 307–326 (2010).
45. Buttler, A. & Spliethoff, H. Current status of water electrolysis for energy storage, grid balancing and sector coupling via power-to-gas and power-to-liquids: A review. *Renewable and Sustainable Energy Reviews* **82**, 2440–2454 (2018).
46. Zhang, X. *et al.* Towards a smart energy network: The roles of fuel/electrolysis cells and technological perspectives. *International Journal of Hydrogen Energy* **40**, 6866–6919 (2015).
47. Mališ, J., Mazúr, P., Paidar, M., Bystron, T. & Bouzek, K. Nafion 117 stability under conditions of PEM water electrolysis at elevated temperature and pressure. *International Journal of Hydrogen Energy* **41**, 2177–2188 (2016).
48. Feng, Q. *et al.* A review of proton exchange membrane water electrolysis on degradation mechanisms and mitigation strategies. *Journal of Power Sources* **366**, 33–55 (2017).
49. Carmo, M., Fritz, D. L., Mergel, J. & Stolten, D. A comprehensive review on PEM water electrolysis. *International Journal of Hydrogen Energy* **38**, 4901–4934 (2013).
50. Laguna-Bercero, M. A. Recent advances in high temperature electrolysis using solid oxide fuel cells: A review. *Journal of Power Sources* **203**, 4–16 (2012).
51. Vilekar, S. A., Fishtik, I. & Datta, R. Kinetics of the Hydrogen Electrode Reaction. *J. Electrochem. Soc.* **157**, B1040 (2010).
52. Yilmaz, F., Balta, M. T. & Selbaş, R. A review of solar based hydrogen production methods. *Renewable and Sustainable Energy Reviews* **56**, 171–178 (2016).
53. Seh, Z. W. *et al.* Combining theory and experiment in electrocatalysis: Insights into materials design. *Science* **355**, (2017).
54. Li, P. *et al.* Recent Advances in the Development of Water Oxidation Electrocatalysts at Mild pH. *Small* **15**, 1805103 (2019).
55. McCrory, C. C. L., Jung, S., Peters, J. C. & Jaramillo, T. F. Benchmarking Heterogeneous Electrocatalysts for the Oxygen Evolution Reaction. *J. Am. Chem. Soc.* **135**, 16977–16987 (2013).
56. Hunter, B. M., Gray, H. B. & Müller, A. M. Earth-Abundant Heterogeneous Water Oxidation Catalysts. *Chem. Rev.* **116**, 14120–14136 (2016).
57. Lee, Y., Suntivich, J., May, K. J., Perry, E. E. & Shao-Horn, Y. Synthesis and Activities of Rutile IrO_2 and RuO_2 Nanoparticles for Oxygen Evolution in Acid and Alkaline Solutions. *J. Phys. Chem. Lett.* **3**, 399–404 (2012).

58. Cherevko, S. *et al.* Oxygen and hydrogen evolution reactions on Ru, RuO 2 , Ir, and IrO 2 thin film electrodes in acidic and alkaline electrolytes: A comparative study on activity and stability. *Catalysis Today* **262**, 170–180 (2016).
59. Kötz, R., Neff, H. & Stucki, S. Anodic Iridium Oxide Films: XPS-Studies of Oxidation State Changes and. *J. Electrochem. Soc.* **131**, 72 (1984).
60. Mohammed-Ibrahim, J. & Sun, X. Recent progress on earth abundant electrocatalysts for hydrogen evolution reaction (HER) in alkaline medium to achieve efficient water splitting – A review. *Journal of Energy Chemistry* **34**, 111–160 (2019).
61. Walton, D. J., Burke, L. D. & Murphy, M. M. Sonoelectrochemistry: Chlorine, hydrogen and oxygen evolution at platinised platinum. *Electrochimica Acta* **41**, 2747–2751 (1996).
62. Hwang, J. *et al.* Perovskites in catalysis and electrocatalysis. *Science* **358**, 751–756 (2017).
63. Zhao, G., Rui, K., Dou, S. X. & Sun, W. Heterostructures for Electrochemical Hydrogen Evolution Reaction: A Review. *Advanced Functional Materials* **28**, 1803291 (2018).
64. Wei, C. *et al.* Recommended Practices and Benchmark Activity for Hydrogen and Oxygen Electrocatalysis in Water Splitting and Fuel Cells. *Advanced Materials* **31**, 1806296 (2019).
65. Hughes, J. P. *et al.* Single step additive manufacturing (3D printing) of electrocatalytic anodes and cathodes for efficient water splitting. *Sustainable Energy Fuels* **4**, 302–311 (2019).
66. Santos, P. L. dos, Rowley-Neale, S. J., Ferrari, A. G.-M., Bonacin, J. A. & Banks, C. E. Ni−Fe (Oxy)hydroxide Modified Graphene Additive Manufactured (3D-Printed) Electrochemical Platforms as an Efficient Electrocatalyst for the Oxygen Evolution Reaction. *ChemElectroChem* **6**, 5633–5641 (2019).
67. Ball, M. & Wietschel, M. The future of hydrogen – opportunities and challenges. *International Journal of Hydrogen Energy* **34**, 615–627 (2009).
68. Nejat Veziroğlu, T. Hydrogen technology for energy needs of human settlements. *International Journal of Hydrogen Energy* **12**, 99–129 (1987).
69. Pires, B. M. *et al.* Electrochemical water oxidation by cobalt-Prussian blue coordination polymer and theoretical studies of the electronic structure of the active species. *Dalton Trans.* **48**, 4811–4822 (2019).
70. Galán-Mascarós, J. R. Water Oxidation at Electrodes Modified with Earth-Abundant Transition-Metal Catalysts. *CHEMELECTROCHEM* **2**, 37–50 (2015).
71. Brown, D. B. & Shriver, D. F. Structures and solid-state reactions of Prussian blue analogs containing chromium, manganese, iron, and cobalt. *Inorg. Chem.* **8**, 37–42 (1969).
72. Zakaria, M. B. & Chikyow, T. Recent advances in Prussian blue and Prussian blue analogues: synthesis and thermal treatments. *Coordination Chemistry Reviews* **352**, 328–345 (2017).
73. Hegner, F. S., Galán-Mascarós, J. R. & López, N. A Database of the Structural and Electronic Properties of Prussian Blue, Prussian White, and Berlin Green Compounds through Density Functional Theory. *Inorg. Chem.* **55**, 12851–12862 (2016).
74. Buser, H. J., Ludi, A., Petter, W. & Schwarzenbach, D. Single-crystal study of Prussian Blue: Fe4[Fe(CN)6]2, 14H2O. *J. Chem. Soc., Chem. Commun.* 1299–1299 (1972) doi:10.1039/C39720001299.
75. Ito, A., Suenaga, M. & Ôno, K. Mössbauer Study of Soluble Prussian Blue, Insoluble Prussian Blue, and Turnbull's Blue. *The Journal of Chemical Physics* **48**, 3597–3599 (2003).
76. Davidson, D. & Welo, L. A. The Nature of Prussian Blue. *J. Phys. Chem.* **32**, 1191–1196 (1928).
77. Robin, M. B. The Color and Electronic Configurations of Prussian Blue. *Inorg. Chem.* **1**, 337–342 (1962).

78. Aksoy, M., Nune, S. V. K. & Karadas, F. A Novel Synthetic Route for the Preparation of an Amorphous Co/Fe Prussian Blue Coordination Compound with High Electrocatalytic Water Oxidation Activity. *Inorganic Chemistry* **55**, 4301–4307 (2016).
79. Nai, J. & Lou, X. W. (David). Hollow Structures Based on Prussian Blue and Its Analogs for Electrochemical Energy Storage and Conversion. *Advanced Materials* **31**, 1706825 (2019).
80. Han, L. *et al.* Enhanced Activity and Acid pH Stability of Prussian Blue-type Oxygen Evolution Electrocatalysts Processed by Chemical Etching. *J. Am. Chem. Soc.* **138**, 16037–16045 (2016).
81. Bleuzen, A. *et al.* Photoinduced Ferrimagnetic Systems in Prussian Blue Analogues CIxCo4[Fe(CN)6]y (CI = Alkali Cation). 1. Conditions to Observe the Phenomenon. *J. Am. Chem. Soc.* **122**, 6648–6652 (2000).
82. Aguilà, D., Prado, Y., Koumousi, E. S., Mathonière, C. & Clérac, R. Switchable Fe/Co Prussian blue networks and molecular analogues. *Chem. Soc. Rev.* **45**, 203–224 (2016).
83. Alsaç, E. P., Ülker, E., Nune, S. V. K., Dede, Y. & Karadas, F. Tuning the Electronic Properties of Prussian Blue Analogues for Efficient Water Oxidation Electrocatalysis: Experimental and Computational Studies. *Chemistry - A European Journal* **24**, 4856–4863 (2018).
84. Pintado, S., Goberna-Ferrón, S., Escudero-Adán, E. C. & Galán-Mascarós, J. R. Fast and Persistent Electrocatalytic Water Oxidation by Co–Fe Prussian Blue Coordination Polymers. *Journal of the American Chemical Society* **135**, 13270–13273 (2013).
85. Boström, H. L. B. *et al.* Probing the Influence of Defects, Hydration, and Composition on Prussian Blue Analogues with Pressure. *J. Am. Chem. Soc.* 11 (2021).
86. Yu, Z.-Y. *et al.* Unconventional CN vacancies suppress iron-leaching in Prussian blue analogue pre-catalyst for boosted oxygen evolution catalysis. *Nat Commun* **10**, 2799 (2019).
87. Yan, D. *et al.* Defect Chemistry of Nonprecious-Metal Electrocatalysts for Oxygen Reactions. *Adv. Mater.* **29**, 1606459 (2017).
88. Jiang, M. *et al.* Thermally activated carbon–nitrogen vacancies in double-shelled NiFe Prussian blue analogue nanocages for enhanced electrocatalytic oxygen evolution. *J. Mater. Chem. A* **9**, 12734–12745 (2021).
89. Hunter, B. M., Gray, H. B. & Müller, A. M. Earth-Abundant Heterogeneous Water Oxidation Catalysts. *Chem. Rev.* **116**, 14120–14136 (2016).
90. McCrory, C. C. L., Jung, S., Peters, J. C. & Jaramillo, T. F. Benchmarking Heterogeneous Electrocatalysts for the Oxygen Evolution Reaction. *J. Am. Chem. Soc.* **135**, 16977–16987 (2013).
91. Kozuch, S. & Martin, J. M. L. “Turning Over” Definitions in Catalytic Cycles. *ACS Catal.* **2**, 2787–2794 (2012).
92. Sallum, L. F., Gonzalez, E. R. & Mota-Lima, A. Quantifying the turnover frequency for ethanol electro-oxidation on polycrystalline Pt in acid and alkaline media. *Electrochemistry Communications* **90**, 26 (2018).
93. Li, D., Liu, H. & Feng, L. A Review on Advanced FeNi-Based Catalysts for Water Splitting Reaction. *Energy Fuels* **34**, 13491–13522 (2020).
94. Hunter, B. M. *et al.* Trapping an Iron(VI) Water-Splitting Intermediate in Nonaqueous Media. *Joule* **2**, 747–763 (2018).
95. Kang, M.-S., Choi, Y.-J., Lee, H.-J. & Moon, S.-H. Effects of inorganic substances on water splitting in ion-exchange membranes: I. Electrochemical characteristics of ion-exchange membranes coated with iron hydroxide/oxide and silica sol. *Journal of Colloid and Interface Science* **273**, 523–532 (2004).

96. Du, P. & Eisenberg, R. Catalysts made of earth-abundant elements (Co, Ni, Fe) for water splitting: Recent progress and future challenges. *Energy Environ. Sci.* **5**, 6012–6021 (2012).
97. Villafranca, J. J. & Nowak, T. 2 Metal Ions at Enzyme Active Sites. in *The Enzymes* (ed. Sigman, D. S.) vol. 20 63–94 (Academic Press, 1992).
98. Li, J. *et al.* Low-Crystalline Bimetallic Metal–Organic Framework Electrocatalysts with Rich Active Sites for Oxygen Evolution. *ACS Energy Lett.* **4**, 285–292 (2019).
99. Han, X. *et al.* Engineering Catalytic Active Sites on Cobalt Oxide Surface for Enhanced Oxygen Electrocatalysis. *Advanced Energy Materials* **8**, 1702222 (2018).
100. Amais, R. S., Donati, G. L. & Zezzi Arruda, M. A. ICP-MS and trace element analysis as tools for better understanding medical conditions. *TrAC Trends in Analytical Chemistry* **133**, 116094 (2020).
101. Pessôa, G. de S., Lopes Júnior, C. A., Madrid, K. C. & Arruda, M. A. Z. A quantitative approach for Cd, Cu, Fe and Mn through laser ablation imaging for evaluating the translocation and accumulation of metals in sunflower seeds. *Talanta* **167**, 317–324 (2017).
102. Agustina, E. *et al.* Simple and Precise Quantification of Iron Catalyst Content in Carbon Nanotubes Using UV/Visible Spectroscopy. *ChemistryOpen* **4**, 613–619 (2015).
103. Cai, H. *et al.* Multi-wavelength spectrophotometric determination of hydrogen peroxide in water with peroxidase-catalyzed oxidation of ABTS. *Chemosphere* **193**, 833–839 (2018).
104. Çağlar, Y. & Saka, E. T. Ionic liquid based dispersive liquid–liquid microextraction procedure for the spectrophotometric determination of copper using 3-dimethylamino rhodanine as a chelating agent in natural waters. *Karbala International Journal of Modern Science* **3**, 185–190 (2017).
105. Sabel, C., Neureuther, J. & Siemann, S. A spectrophotometric method for the determination of zinc, copper, and cobalt ions in metalloproteins using Zincon. *Analytical biochemistry* **397**, 218–26 (2009).
106. Prenesti, E., Daniele, P. & Toso, S. Visible spectrophotometric determination of metal ions: The influence of structure on molar absorptivity value of copper(II) complexes in aqueous solution. *Analytica Chimica Acta* **459**, 323–336 (2002).
107. Uddin, A. H. *et al.* Comparative study of three digestion methods for elemental analysis in traditional medicine products using atomic absorption spectrometry. *Journal of Analytical Science and Technology* **7**, 6 (2016).
108. Kuhn, D. D. & Young, T. C. Photolytic degradation of hexacyanoferrate (II) in aqueous media: The determination of the degradation kinetics. *Chemosphere* **60**, 1222–1230 (2005).
109. Santos, C., Alava-Moreno, F., Lavilla, I. & Bendicho, C. Total As in seafood as determined by transverse heated electrothermal atomic absorption spectrometry-longitudinal Zeeman background correction: An evaluation of automated ultrasonic slurry sampling, ultrasound-assisted extraction and microwave-assisted digestion methods. *J. Anal. At. Spectrom.* **15**, 987–994 (2000).
110. Druzian, G. T. *et al.* Rare earth element determination in heavy crude oil by USN-ICP-MS after digestion using a microwave-assisted single reaction chamber. *J. Anal. At. Spectrom.* **31**, 1185–1191 (2016).
111. Adamson, A. W. Inorganic photochemistry - - then and now. *Coordination Chemistry Reviews* **125**, 1–12 (1993).
112. Arellano, C. A. P. & Martínez, S. S. Effects of pH on the degradation of aqueous ferricyanide by photolysis and photocatalysis under solar radiation. *Solar Energy Materials and Solar Cells* **94**, 327–332 (2010).

113. Meeussen, J. C. L., Keizer, M. G., Van Riemsdijk, W. H. & De Haan, F. A. M. Dissolution behavior of iron cyanide (Prussian blue) in contaminated soils. *Environ. Sci. Technol.* **26**, 1832–1838 (1992).
114. Jr, A. M., Moraes, J. E. F., Okano, L. T., Silvério, C. A. & Quina, F. H. Photolysis of ferric ions in the presence of sulfate or chloride ions: implications for the photo-Fenton process. *Photochem. Photobiol. Sci.* **8**, 985–991 (2009).
115. Subelzu, N. & Schöneich, C. Near UV and Visible Light Induce Iron-Dependent Photodegradation Reactions in Pharmaceutical Buffers: Mechanistic and Product Studies. *Mol. Pharmaceutics* **17**, 4163–4179 (2020).
116. Caicedo, D. F., Brum, I. A. S. & Buitrago, L. A. B. Photocatalytic degradation of ferricyanide as synthetic gold mining wastewater using TiO_2 assisted by H_2O_2. *REM, Int. Eng. J.* **73**, 99–107 (2019).
117. Santos, P. L. dos, Rowley-Neale, S. J., Ferrari, A. G.-M., Bonacin, J. A. & Banks, C. E. Ni−Fe (Oxy)hydroxide Modified Graphene Additive Manufactured (3D-Printed) Electrochemical Platforms as an Efficient Electrocatalyst for the Oxygen Evolution Reaction. *ChemElectroChem* **6**, 5633–5641 (2019).
118. Friedrich, R. B., Ravanello, A., Cichota, L. C., Rolim, C. M. B. & Beck, R. C. R. Validation of a simple and rapid UV spectrophotometric method for dexamethasone assay in tablets. *Quím. Nova* **32**, 1052–1054 (2009).
119. Shrivastava, A. & Gupta, V. Methods for the determination of limit of detection and limit of quantitation of the analytical methods. *Chron Young Sci* **2**, 21 (2011).
120. Braterman, P. S., Song, J. I. & Peacock, R. D. Electronic absorption spectra of the iron(II) complexes of 2,2'-bipyridine, 2,2'-bipyrimidine, 1,10-phenanthroline, and 2,2':6',2''-terpyridine and their reduction products. *Inorg. Chem.* **31**, 555–559 (1992).
121. von Eschwege, K. G. & Conradie, J. Iron phenanthrolines: A density functional theory study. *Inorganica Chimica Acta* **471**, 391–396 (2018).
122. Zhang, W. *et al.* Core–Shell Prussian Blue Analogs with Compositional Heterogeneity and Open Cages for Oxygen Evolution Reaction. *Advanced Science* **6**, 1801901 (2019).
123. Frenzel, N., Hartley, J. & Frisch, G. Voltammetric and spectroscopic study of ferrocene and hexacyanoferrate and the suitability of their redox couples as internal standards in ionic liquids. *Phys. Chem. Chem. Phys.* **19**, 28841–28852 (2017).
124. Ayers, J. B. & Waggoner, W. H. Synthesis and properties of two series of heavy metal hexacyanoferrates. *Journal of Inorganic and Nuclear Chemistry* **33**, 721–733 (1971).
125. Zambiazi, P. J. *et al.* Electrocatalytic water oxidation reaction promoted by cobalt-Prussian blue and its thermal decomposition product under mild conditions. *Dalton Trans.* **49**, 16488–16497 (2020).
126. Al-Hakkani, M. F., Gouda, G. A. & Hassan, S. H. A. A review of green methods for phyto-fabrication of hematite (α-Fe2O3) nanoparticles and their characterization, properties, and applications. *Heliyon* **7**, e05806 (2021).
127. Freitas, A. L. M., Muche, D. N. F., Leite, E. R. & Souza, F. L. Interface engineering of nanoceramic hematite photoelectrode for solar energy conversion. *Journal of the American Ceramic Society* **103**, 6833–6846 (2020).
128. Lian, J. *et al.* Hematite (α-Fe2O3) with Various Morphologies: Ionic Liquid-Assisted Synthesis, Formation Mechanism, and Properties. *ACS Nano* **3**, 3749–3761 (2009).
129. Sherman, D. M. & Waite, T. D. Electronic spectra of Fe3+ oxides and oxide hydroxides in the near IR to near UV. *American Mineralogist* **70**, 1262–1269 (1985).

130. Goldsmith, Z. K. *et al.* Characterization of NiFe oxyhydroxide electrocatalysts by integrated electronic structure calculations and spectroelectrochemistry. *PNAS* **114**, 3050–3055 (2017).
131. Santos, J. R. N. *et al.* Reduced Graphene Oxide-Supported Nickel(II)-Bis(1,10-Phenanthroline) Complex as a Highly Active Electrocatalyst for Ethanol Oxidation Reaction. *Electrocatalysis* **10**, 560–572 (2019).
132. Liardet, L., Katz, J. E., Luo, J., Grätzel, M. & Hu, X. An ultrathin cobalt–iron oxide catalyst for water oxidation on nanostructured hematite photoanodes. *J. Mater. Chem. A* **7**, 6012–6020 (2019).
133. Hosseini, S. E. & Wahid, M. A. Hydrogen production from renewable and sustainable energy resources: Promising green energy carrier for clean development. *Renewable and Sustainable Energy Reviews* **57**, 850–866 (2016).
134. Zambiazi, P. *et al.* Performance of Water Oxidation by 3D Printed Electrodes Modified by Prussian Blue Analogues. *J. Braz. Chem. Soc.* (2020) doi:10.21577/0103-5053.20200088.
135. Zoski, C. G. Review—Advances in Scanning Electrochemical Microscopy (SECM). *J. Electrochem. Soc.* **163**, H3088–H3100 (2016).
136. Voronin, O. G. *et al.* Prussian Blue-modified ultramicroelectrodes for mapping hydrogen peroxide in scanning electrochemical microscopy (SECM). *Electrochemistry Communications* **23**, 102–105 (2012).
137. Maljusch, A., Ventosa, E., Rincón, R. A., Bandarenka, A. S. & Schuhmann, W. Revealing onset potentials using electrochemical microscopy to assess the catalytic activity of gas-evolving electrodes. *Electrochemistry Communications* **38**, 142–145 (2014).
138. Iffelsberger, C., Raith, T., Vatsyayan, P., Vyskočil, V. & Matysik, F.-M. Detection and imaging of reactive oxygen species associated with the electrochemical oxygen evolution by hydrodynamic scanning electrochemical microscopy. *Electrochimica Acta* **281**, 494–501 (2018).
139. Chen, X., Botz, A. J. R., Masa, J. & Schuhmann, W. Characterisation of bifunctional electrocatalysts for oxygen reduction and evolution by means of SECM. *J Solid State Electrochem* **20**, 1019–1027 (2016).
140. Ding, Y., Gu, G. & Xia, X.-H. Electrochemical deposition and mechanism investigation of Prussian blue on graphic carbon paste electrode from an acidic ferricyanide solution. *J Solid State Electrochem* **12**, 553–558 (2008).
141. Anantharaj, S. & Noda, S. Appropriate Use of Electrochemical Impedance Spectroscopy in Water Splitting Electrocatalysis. *ChemElectroChem* **7**, 2297–2308 (2020).
142. Meloni, G. N. 3D Printed and Microcontrolled: The One Hundred Dollars Scanning Electrochemical Microscope. *Anal. Chem.* **89**, 8643–8649 (2017).
143. Schneidereit, D., Kraus, L., Meier, J. C., Friedrich, O. & Gilbert, D. F. Step-by-step guide to building an inexpensive 3D printed motorized positioning stage for automated high-content screening microscopy. *Biosensors and Bioelectronics* **92**, 472–481 (2017).
144. Guver, A. *et al.* A low-cost and high-precision scanning electrochemical microscope built with open source tools. *HardwareX* **6**, e00082 (2019).
145. Bard, A. J. & Faulkner, L. R. *Electrochemical methods: fundamentals and applications*. (Wiley, 2001).
146. Nicholson, R. S. Theory and Application of Cyclic Voltammetry for Measurement of Electrode Reaction Kinetics. *Anal. Chem.* **37**, 1351–1355 (1965).

147. Francischini, D. S. & Arruda, M. A. Z. When a picture is worth a thousand words: Molecular and elemental imaging applied to environmental analysis – A review. *Microchemical Journal* **169**, 106526 (2021).
148. Crone, B. *et al.* Quantitative imaging of platinum-based antitumor complexes in bone tissue samples using LA-ICP-MS. *Journal of Trace Elements in Medicine and Biology* **54**, 98–102 (2019).
149. Amais, R. S. *et al.* Trace elements distribution in tropical tree rings through high-resolution imaging using LA-ICP-MS analysis. *Journal of Trace Elements in Medicine and Biology* **68**, 126872 (2021).
150. Amais, R. S., Francischini, D. S., Moreau, P. S. & Arruda, M. A. Z. *Laser Chemical Elemental Analysis: From Total to Images*. *Practical Applications of Laser Ablation* (IntechOpen, 2020). doi:10.5772/intechopen.94385.
151. López-Fernández, H. *et al.* LA-iMageS: a software for elemental distribution bioimaging using LA–ICP–MS data. *Journal of Cheminformatics* **8**, 65 (2016).
152. Yang, R., Qian, Z. & Deng, J. Electrochemical Deposition of Prussian Blue from a Single Ferricyanide Solution. *J. Electrochem. Soc.* **145**, 2231 (1998).
153. Katic, V. *et al.* 3D Printed Graphene Electrodes Modified with Prussian Blue: Emerging Electrochemical Sensing Platform for Peroxide Detection. *ACS Appl. Mater. Interfaces* **11**, 35068–35078 (2019).
154. Kong, B., Selomulya, C., Zheng, G. & Zhao, D. New faces of porous Prussian blue: interfacial assembly of integrated hetero-structures for sensing applications. *Chem. Soc. Rev.* **44**, 7997–8018 (2015).
155. dos Santos, M. F. *et al.* 3D-Printed Low-Cost Spectroelectrochemical Cell for In Situ Raman Measurements. *Anal. Chem.* **91**, 10386–10389 (2019).
156. M. Pires, B., Hegner, F. S., Bonacin, J. A. & Galán-Mascarós, J.-R. Ligand Effects of Penta- and Hexacyanidoferrate-Derived Water Oxidation Catalysts on BiVO4 Photoanodes. *ACS Appl. Energy Mater.* **3**, 8448–8456 (2020).
157. Formiga, A. L. B., Vancoillie, S. & Pierloot, K. Electronic Spectra of N-Heterocyclic Pentacyanoferrate(II) Complexes in Different Solvents, Studied by Multiconfigurational Perturbation Theory. *Inorg. Chem.* **52**, 10653–10663 (2013).
158. Zhou, Z. *et al.* CuInS2 quantum dot-sensitized TiO2 nanorod array photoelectrodes: synthesis and performance optimization. *Nanoscale Research Letters* **7**, 652 (2012).
159. Moretti, G. & Gervais, C. Raman spectroscopy of the photosensitive pigment Prussian blue. *J. Raman Spectrosc.* **49**, 1198–1204 (2018).
160. Tuschel, D. Selecting an Excitation Wavelength for Raman Spectroscopy. *Spectroscopy* **31**, 14–23 (2016).
161. Sendova, M. Surface kinetics analysis by direct area measurement: Laser assisted dehydration of α-FeOOH. *AIP Advances* **9**, 075101 (2019).
162. Pires, B. M., Galdino, F. E. & Bonacin, J. A. Electrocatalytic reduction of oxygen by metal coordination polymers produced from pentacyanidoferrate(II) complex. *Inorganica Chimica Acta* **466**, 166–173 (2017).
163. Suen, N.-T. *et al.* Electrocatalysis for the oxygen evolution reaction: recent development and future perspectives. *Chemical Society Reviews* **46**, 337–365 (2017).
164. Reier, T., Nong, H. N., Teschner, D., Schlögl, R. & Strasser, P. Electrocatalytic Oxygen Evolution Reaction in Acidic Environments - Reaction Mechanisms and Catalysts. *Adv. Energy Mater.* **7**, 1601275 (2017).

165. Morandi Pires, B., Venturinelli Jannuzzi, S. A., Barboza Formiga, A. L. & Alves Bonacin, J. Prussian Blue Films Produced by Pentacyanidoferrate(II) and Their Application as Active Electrochemical Layers: Prussian Blue Films as Active Electrochemical Layers. *Eur. J. Inorg. Chem.* **2014**, 5812-N5819 (2014).
166. Jwo, J.-J. & Haim, A. Kinetics and mechanism of the reactions between the oxygen-bonded complexes 4-, 3-, and 2-pyridinecarboxylatopentaamminecobalt(III) and aquopentacyanoferrate(II). *J. Am. Chem. Soc.* **98**, 1172–1176 (1976).
167. Itaya, K. & Uchida, I. Nature of intervalence charge-transfer bands in Prussian blues. *Inorg. Chem.* **25**, 389–392 (1986).
168. Mortimer, R. J. & Rosseinsky, D. R. Iron hexacyanoferrate films : spectroelectrochemical distinction and electrodeposition sequence of 'soluble' (K+-containing) and 'insoluble' (K+-free) Prussian Blue, and composition changes in polyelectrochromic switching. *J. Chem. Soc., Dalton Trans.* 2059–2062 (1984) doi:10.1039/DT9840002059.
169. Toma, H. E. & Malin, J. M. Properties and reactivity of some pentacyanoferrate(II) complexes of aromatic nitrogen heterocycles. *Inorg. Chem.* **12**, 1039–1045 (1973).
170. Wu, Q., Wu, G., Wang, L., Hu, W. & Wu, H. Facile synthesis and optical properties of Prussian Blue microcubes and hollow Fe2O3 microboxes. *Materials Science in Semiconductor Processing* **30**, 476–481 (2015).
171. Hocking, R. K. *et al.* Fe L-Edge XAS Studies of K4[Fe(CN)6] and K3[Fe(CN)6]: A Direct Probe of Back-Bonding. *J. Am. Chem. Soc.* **128**, 10442–10451 (2006).
172. Lee, J. H. *et al.* Prussian blue analogues as platform materials for understanding and developing oxygen evolution reaction electrocatalysts. *Journal of Catalysis* **393**, 390–398 (2021).
173. Risch, M., Morales, D. M., Villalobos, J. & Antipin, D. What X-Ray Absorption Spectroscopy Can Tell Us About the Active State of Earth-Abundant Electrocatalysts for the Oxygen Evolution Reaction**. *Angewandte Chemie International Edition* **61**, e202211949 (2022).
174. Stevie, F. A. & Donley, C. L. Introduction to x-ray photoelectron spectroscopy. *Journal of Vacuum Science & Technology A* **38**, 063204 (2020).
175. Grandjean, F., Samain, L. & Long, G. J. Characterization and utilization of Prussian blue and its pigments. *Dalton Trans.* **45**, 18018–18044 (2016).
176. Kettle, S. F. A., Diana, E., Marchese, E. M. C., Boccaleri, E. & Stanghellini, P. L. The vibrational spectra of the cyanide ligand revisited: the ν(CN) infrared and Raman spectroscopy of Prussian blue and its analogues. *J. Raman Spectrosc.* **42**, 2006–2014 (2011).
177. Nakamoto, K. *Infrared and Raman Spectra of Inorganic and Coordination Compounds: Part B: Applications in Coordination, Organometallic, and Bioinorganic Chemistry*. (John Wiley & Sons, Inc, 2008).
178. Anantharaj, S. *et al.* Precision and correctness in the evaluation of electrocatalytic water splitting: revisiting activity parameters with a critical assessment. *Energy Environ. Sci.* **11**, 744–771 (2018).
179. Bagus, P. S., Ilton, E. S. & Nelin, C. J. The interpretation of XPS spectra: Insights into materials properties. *Surface Science Reports* **68**, 273–304 (2013).
180. Calvin, S. *XAFS for Everyone*. (CRC Press, 2013). doi:10.1201/b14843.
181. Timoshenko, J. & Roldan Cuenya, B. In Situ/Operando Electrocatalyst Characterization by X-ray Absorption Spectroscopy. *Chem. Rev.* **121**, 882–961 (2021).

182. Bonhommeau, S. *et al*. Metal-to-ligand and ligand-to-metal charge transfer in thin films of Prussian blue analogues investigated by X-ray absorption spectroscopy. *Phys. Chem. Chem. Phys.* **10**, 5882–5889 (2008).
183. Baker, M. L. *et al.* K- and L-edge X-ray absorption spectroscopy (XAS) and resonant inelastic X-ray scattering (RIXS) determination of differential orbital covalency (DOC) of transition metal sites. *Coordination Chemistry Reviews* **345**, 182–208 (2017).

Appendix A

Se a Tese ou Dissertação for reproduzida em formato alternativo (com artigos anexados), este documento, preenchido e assinado, deve ser inserido no trabalho como Anexo.

DECLARAÇÃO

As cópias dos documentos de minha autoria ou de minha coautoria, já publicados ou submetidos para publicação em revistas científicas ou anais de congressos sujeitos a arbitragem, que constam da minha Dissertação/Tese de Mestrado/Doutorado, intitulada" WATER OXIDATION PERFORMANCE ENHANCED BY ELECTROCHEMICALLY DESIGNED VACANCIES ON PRUSSIAN BLUE ANALOGUES BASED CATALYSTS" não infringem os dispositivos da Lei nº 9.610/98, nem o direito autoral de qualquer editora.

Campinas, 20 de Julho de 2023

Autor – Rafael Lavagnolli Germscheidt - R.G. nº 37.791.046-6

Documento assinado digitalmente
JULIANO ALVES BONACIN
Data: 12/07/2023 16:47:38-0300
Verifique em https://validar.iti.gov.br

Orientador – Prof. Dr. Juliano Alves Bonacin - RG nº 6.1634.76-2

Appendix B

17/07/2023, 13:24 Rightslink® by Copyright Clearance Center

CCC RightsLink

Help Live Chat

Hydrogen Environmental Benefits Depend on the Way of Production: An Overview of the Main Processes Production and Challenges by 2050

Author: Juliano A. Bonacin, Pāmyla L. dos Santos, Evandro Datti, et al

Publication: Advanced Energy and Sustainability Research

Publisher: John Wiley and Sons

Date: Jun 25, 2021

© 2021 The Authors. Advanced Energy and Sustainability Research published by Wiley-VCH GmbH

Open Access Article

This is an open access article distributed under the terms of the Creative Commons CC BY license, which permits unrestricted use, distribution, and reproduction in any medium, provided the original work is properly cited.

You are not required to obtain permission to reuse this article.

For an understanding of what is meant by the terms of the Creative Commons License, please refer to Wiley's Open Access Terms and Conditions.

Permission is not required for this type of reuse.

Wiley offers a professional reprint service for high quality reproduction of articles from over 1400 scientific and medical journals. Wiley's reprint service offers:

- Peer reviewed research or reviews
- Tailored collections of articles
- A professional high quality finish
- Glossy journal style color covers
- Company or brand customisation
- Language translations
- Prompt turnaround times and delivery directly to your office, warehouse or congress.

Please contact our Reprints department for a quotation. Email corporatesaleseurope@wiley.com or corporatesalesusa@wiley.com or corporatesalesDE@wiley.com.

© 2023 Copyright - All Rights Reserved | Copyright Clearance Center, Inc. | Privacy statement | Data Security and Privacy | For California Residents | Terms and ConditionsComments? We would like to hear from you. E-mail us at customercare@copyright.com

1/1

Appendix C

17/07/2023, 13:36 COPYRIGHT - Journal of the Brazilian Chemical Society

PubliSBQ JBCS QN QNEsc QNInt RVq BE QuiD+ EditSBQ

Digite aqui

JBCS QN QNEsc QNInt RVq

Type a word SEARCH

JBCS Google SciELO

13:35, Mon Jul 17

Home Instructions for Authors Instructions for Referees General Info Contacts

Submission online (ScholarOne)

Open Access/APCs

Follow BK

Forthcoming Papers

FPapers - ChrMelRelTech

Current Issue

Past Issues

Reviews/Accounts - last 5 years

Past Special Issues

Virtual Thematic Collections

Cover Gallery/ePUB

Ethical Guides

JBCS Medal of Honor

Most Highly Cited Papers

CNPq Conselho Nacional de Desenvolvimento Científico e Tecnológico

CAPES

Ministério da Educação

Ministério da Ciência e Tecnologia

FAPESP

IQ Instituto de Química

Copyright

Authors submitting a manuscript do so on the understanding that if accepted for publication in the ***Journal of the Brazilian Chemical Society*** (***JBCS***), copyright of the article shall be assigned to the *Sociedade Brasileira de Química (SBQ)*

Copyright encompasses exclusive rights to reproduce and deliver the article in all form and media, including reprints, photographs, microfilms and any other similar reproductions, as well as translations. The reproduction of any part of this journal, its storage in databases and its transmission by any form or media - such as electronic, electrostatic and mechanical copies, photocopies, recordings, magnetic media, etc. - will be allowed only with a written permission from the *Sociedade Brasileira de Química*.

Permission for other use. The copyright owner's consent does not extend to copying for general distribution, for promotion, for creating new works, or for resale. Specific written permission must be obtained from the Publisher (*PubliSBQ-**JBCS***) for such copying.

Creative Commons Licenses - Open access articles in *SBQ* journals are published under Creative Commons licenses. These licenses provide an industry-standard framework to support easy re-use of open access material.
***JBCS* articles** are published open access under a CC BY license (Creative Commons Attribution 4.0 International license) **from 26-9 issue**. The CC BY license is the most open license available and considered a 'gold standard' for open access; it is also preferred by many funders. This license allows readers to copy and redistribute the material in any medium or format, and to alter, transform, or build on the material, including for commercial use, on the condition that the original author is credited.

The *Sociedade Brasileira de Química*, the editors and the advisory editorial board make every effort to ensure that no wrong or misleading data, opinions or statements be published in the journal. In any way, the contents of the articles and advertisements published in the ***Journal of the Brazilian Chemical Society*** are sole and exclusive responsibility of their respective authors and advertisers. Therefore, the SBQ, the editors, the advisory editorial board, directors, agents and officers declare themselves totally free from any responsibility for the consequences that may result from those wrong or misleading data, opinions or statements.

https://jbcs.sbq.org.br/copyright 1/3

Appendix D

17/07/2023, 13:36 Creative Commons — Attribution 4.0 International — CC BY 4.0

This page is available in the following languages:

Creative Commons License Deed

Attribution 4.0 International (CC BY 4.0)

This is a human-readable summary of (and not a substitute for) the license.

You are free to:

Share — copy and redistribute the material in any medium or format

Adapt — remix, transform, and build upon the material

for any purpose, even commercially.

The licensor cannot revoke these freedoms as long as you follow the license terms.

Under the following terms:

Attribution — You must give appropriate credit, provide a link to the license, and indicate if changes were made. You may do so in any reasonable manner, but not in any way that suggests the licensor endorses you or your use.

No additional restrictions — You may not apply legal terms or technological measures that legally restrict others from doing anything the license permits.

Notices:

You do not have to comply with the license for elements of the material in the public domain or where your use is permitted by an applicable exception or limitation.

No warranties are given. The license may not give you all of the permissions necessary for your intended use. For example, other rights such as publicity, privacy, or moral rights may limit how you use the material.

https://creativecommons.org/licenses/by/4.0/ 1/1

Appendix E

12/07/2023, 14:17 Rightslink® by Copyright Clearance Center

CCC RightsLink

Home | Help | Live Chat | Sign in | Create Account

ACS Publications
Most Trusted. Most Cited. Most Read.

Water Oxidation Performance Enhanced by Electrochemically Designed Vacancies on a Prussian Blue Catalyst

Author:
Rafael Lavagnolli Germscheidt, Danielle da Silva Francischini, Mariana Bianchini Silva, et al

Publication: ACS Applied Energy Materials

Publisher: American Chemical Society

Date: Aug 1, 2022

Copyright © 2022, American Chemical Society

PERMISSION/LICENSE IS GRANTED FOR YOUR ORDER AT NO CHARGE

This type of permission/license, instead of the standard Terms and Conditions, is sent to you because no fee is being charged for your order. Please note the following:

- Permission is granted for your request in both print and electronic formats, and translations.
- If figures and/or tables were requested, they may be adapted or used in part.
- Please print this page for your records and send a copy of it to your publisher/graduate school.
- Appropriate credit for the requested material should be given as follows: "Reprinted (adapted) with permission from {COMPLETE REFERENCE CITATION}. Copyright {YEAR} American Chemical Society." Insert appropriate information in place of the capitalized words.
- One-time permission is granted only for the use specified in your RightsLink request. No additional uses are granted (such as derivative works or other editions). For any uses, please submit a new request.

If credit is given to another source for the material you requested from RightsLink, permission must be obtained from that source.

BACK CLOSE WINDOW

© 2023 Copyright - All Rights Reserved | Copyright Clearance Center, Inc. | Privacy statement | Data Security and Privacy | For California Residents | Terms and ConditionsComments? We would like to hear from you. E-mail us at customercare@copyright.com

https://s100.copyright.com/AppDispatchServlet#formTop 1/1